Final Report

Project Title: Development of Novel Non-Pt Group Metal Electrocatalysts for PEM Fuel Cell Applications

Project Period: (July 31, 2010 to July 31st, 2015)

Reporting Period: (July 31st, 2010 to July 31st 2015)

Date of Report: (January 4th 2016)

Recipient: Northeastern University, Prof. Sanjeev Mukerjee (P.I)

Award Number: DE-EE0000459

Working Partners:
(1) University of New Mexico (UNM) (Prof. Plamen Atanassov)
(2) Michigan State University (MSU) (Prof. Scott Barton)
(3) Nissan Technical Center, North America (NTCNA) (Dr. Nilesh Dale)
(4) Pajarito Powders (PPC) (Dr. Bar Halevi)

Cost-Sharing Partners:(NEU, UNM, MSU, PPC and NTCNA)

Contact:

Technical Point of contact:

Dr. Sanjeev Mukerjee, Professor;
Department of Chemistry and Chemical Biology,
Northeastern University, Boston, MA
Phone: 617 373 2382, Fax: 617 373 8795
Email: s.mukerjee@neu.edu

Business Point of Contact:

Ms. Diane Keys,
Office of Research Administration and Finance,
490 Renaissance Place, Northeastern University, 360 Huntington Avenue, Boston, MA 02115
Phone: 617 373 5771, Fax: 617 373 4595, email: di.keys@neu.edu

DOE Managers: Ms. Donna Ho (DOE, HQ); Mr. David Peterson, Shaun Onorato, Golden Field Office, Golden, CO. Phone: 303-275-4956, E-Mail: david.peterson@go.doe.gov

Acknowledgment: This material is based upon work supported by the Department of Energy, Office of Energy Efficiency and Renewable Energy (EERE), under Award Number DE-EE0000459.

Disclaimer: This report was prepared as an account of work sponsored by an agency of the United States Government. Neither the United States Government nor any agency thereof, nor any of their employees, makes any warranty, express or implied, or assumes any legal liability or responsibility for the accuracy, completeness, or usefulness of any information, apparatus, product, or process disclosed, or represents that its use would not infringe privately owned rights. Reference herein to any specific commercial product, process, or service by trade name, trademark, manufacturer, or otherwise does not necessarily constitute or imply its endorsement, recommendation, or favoring by the United States Government or any agency thereof. The views and opinions of authors expressed herein do not necessarily state or reflect those of the United States Government or any agency thereof.

Northeastern University - Final Report

Development of Novel Non-Pt Group Metal Electrocatalysts for PEM Fuel Cell Applications

Executive Summary

I. PROJECT OBJECTIVES

The objective of this project is to design non Platinum (Pt) group based catalyst materials for the cathode oxygen reduction reaction (ORR) and supporting gas transport layer, both in the interfacial reaction layer between the electrode and membrane as well as in the underlying gas diffusion medium, for meeting and exceeding DOE goals for application in Polymer Electrolyte Fuel Cells for automotive applications. This project is focused on materials development and is assisted by advanced analytical tools, computation, and testing for improving the design via critical understanding of electrocatalysis in these novel structures.

II. OVERALL PROJECT SCOPE

The materials design and synthesis includes (a) reaction polymer approach in conjunction with metal salt and carbon support and a polymer such as polyaniline or polyvinylidene guanidine, Silica template structures based on (b) mechano-chemical approach using organic charge transfer salt and a metal salt or (c) chelating (such as amino-antipyrenes) (d) non chelating organic precursors (such as carbendazim) and a metal salt precursor and (e) metal organic precursor based templated structures using chelated transition metal salts. The common denominator is to replace supported PGM based metal clusters with systems where individual atoms are configured in well-characterized metal organic frameworks with correct geometry for effective four-electron reduction of oxygen (most challenging). The important issues of understanding the turn over frequency (TOF) at the active site are addressed using the combination of computation and new *in situ* synchrotron spectroscopy with the ability to determine site-specific adsorption *in situ* under actual cell operating conditions. This combination has been previously used effectively for understanding oxygen reduction reaction (ORR) on Pt and Pt alloys electrocatalysts. Further, this project involves the redesign of the reaction layer and gas diffusion medium for enhanced mass transport characteristics. The testing and validation as well as membrane electrode assembly (MEA) fabrication are conducted at various partner institutions. Materials developed, as a part of this effort is in the process of being scaled up both in terms of electrocatalysts as well as MEA's. Validation of initial results is conducted in large scale single cell tests and according to DOE specified procedures specific to this project.

III. OBJECTIVES, METRICS AND MILESTONES

Principle target for the project's first phase were based on performance in oxygen where the project's Go/No-Go decision point milestone of 100 mA/cm^2 at 0.8 V (internal resistance-free, iR-free) at 80^oC, pure H_2/O_2, with 1.5 bar total pressure was met. Susequently, the principle objectives were to (a) transition the project from H_2/O_2 to H_2/Air with slated target of exceeding 30 mA/cm^2 @ 0.8 V, 2.5 bar total pressure and an end of the project target of 1 A/cm^2 @ 0.4 V (same total pressure), both under 100% relative humidity. The target for catalyst material scale up was to achieve 100 g batch size at the end of the program. This scale up target had a quality control milestone of less than 5% variation of activity measured with H_2/Air (2.5 bar total pressure) at 0.8 V. In addition, the project also aimed at arriving at a unified understanding of the nature of active sites in these catalysts as well as some preliminary understanding of the mechanistic pathway. Also addressed is the development of an integrated method for determination of mass transport parameters using a combination of Helox experiments and modeling of the gas diffusion media, especially the micro-porous layer on the gas diffusion electrode (GDE).

TECHNICAL TARGETS:

The technical targets for this project are listed in Table 1.

Table 1. Progress towards Meeting Technical Targets for Non-PGM Electrocatalysts for Transportation Applications

Characteristic	Units	2015 Target	NEU 2014 status
Specific Activity @ 80ºC, 1.5 bar total pressure, H_2/O_2, 100% relative humidity (RH) 2013 Go/No go target	A/cm^3	Volumetric activity of 300 A/cm^3 -0.8 V (iR-free) projected from ~10 mA/cm^2 Un-projected volumetric activity (no target set)	 400 A/cm^3 95 A/cm^3
	A/cm^2	100 mA/cm^2 (iR-free)	100 mA/cm^2
Specific Activity @ 80ºC, 2.5 bar total pressure, H_2/Air, 100% relative humidity (RH) 2014 Target	A/cm^2	Areal activity of 30 mA/cm^2 @ 0.8 V Areal activity of 1 A/cm^2 @ 0.4 V	70 mA/cm^2 >950 mA/cm^2
Scale up of Catalyst	gms	100 gms	Target successfully met
Intra and inter batch variability	percent	5% variation for both inter and intra batch	Target successfully met
Durability at 80ºC Cycling: Catalyst Durability	% loss of activity	5%	<1%
Durability at 80ºC Cycling: Carbon Corrosion Durability	% loss of activity	10%	<50% Partially recoverable

Approach

NEU structured the program along the task flow chart in Scheme 1:

Task 1. Materials Preparation

Task 1.1 Development of Poly-nuclear Reaction Centers

The synthesis is described in the following subtasks.

Subtask 1.1.1: Synthesis of Trinuclear Cobalt-Triazole
Subtask 1.1.2: Development of Binucleating and Tetranucleating Ligands for Coordination Polymers
Subtask 1.1.3: Biomimetic Coordination Polymer Systems
Subtask 1.1.4: Effect of Coordinating Atom in the Ligand on Catalytic Active Site

Task 1.2 Open Framework Templated Structures

The pore structures studied in this effort would be specifically tailored for understanding how reaction layer transport mechanisms work in the context of these templated structures.

Task 1.3 Development of MNC Catalyst Synthesis Process

Subtask 1.3.1: Varying Nitrogen Precursor materials

Varying aromatic nitrogen precursors with increasing N/C atomic ratio, such as bipyridine (N/C=0.2), pyrazine (0.5), purine (0.8) and melamine (2), will be employed to study the effect of pyridinic precursors on surface nitrogen content of the resulting catalyst.

Task 1.4 Development of Catalyst Structure Using Enzyme Mimics
Subtask 1.4.1: New Catalyst Compositions Based on Enzyme Mimics
Subtask 1.4.2: Ligands of Controlled Electron Density

Task 1.5 Scale-up of Catalysts Formulations
Use initial formulations showing promise, such as those developed under the previous tasks, for scale-up of catalyst materials. Synthesis strategies and implementation of reproducible data in single cells will be the focus. This will involve the following: (a) use the best down-selected candidates for scale to 10-50 gram quantities; and (b) throughout process, advise on feasibility and cost for manufacturability. Down select condition would follow the criterion of the overall go/no-go decision. Hence only those candidates in Task 1 which show potential of meeting this goal will be subject to scale-up studies.

Task 2. Development of Novel Reaction Layer Formulations and Design of Gas Diffusion Medium for Enhanced Mass Transport and Fabrication of Membrane Electrode Assemblies

Task 2.1 Catalyst Support and Electrode Optimization and Fabrication of Membrane Electrode Assemblies
Subtask 2.1.1: Support Modifications
Subtask 2.1.2: Mass Transport
Subtask 2.1.3: Hydrophilicity/Hydrophobicity
Task 2.2 Scale-up Strategies of MEA and Electrode Structures

Task 3. Fuel Cell Testing and Initial Durability Measurements

Task 3.1 Electrocatalyst Testing Procedures (RRDE)
Task 3.2 High Throughput Screening of Electrocatalysts Using Segmented Multichannel Cells
Task 3.3 Catalyst-Electrode Design for Durability
Subtask 3.3.1: Catalyst Durability Design
Subtask 3.3.2: Electrode Studies for Durability
Subtask 3.3.3: Spectroscopic Studies on Durability
Task 3.4 Synchrotron X-Ray Absorption for In-situ Durability Measurements, and Modeling
Task 3.5 Fuel Cell Testing
Subtask 3.5.1: Fuel Cell Testing under PEMFC Conditions
Subtask 3.5.2 Fuel Cell Tests in MEA's using Celtec-P Membranes for High Temperature Applications

Task 4. Mechanistic Studies (Ex-Situ and In-Situ Spectroscopy and Modeling)

Task 4.1 *Ex Situ* Studies
Task 4.2 *In-situ* Measurements
Subtask 4.2.1: In-situ Synchrotron Measurements for Elucidation of Electrocatalytic Pathways in Complex Reaction Centers
Subtask 4.2.2: FTIR Measurements
Task 4.3 Computation/Modeling of Reaction Sites and Transport Behavior in Reaction Layer
Subtask 4.3.1: Calculations of Reaction Properties
Subtask 4.3.2: Macroscopic Models of Electrode Function
Subtask 4.3.3: Simulation of Transport and Reaction in Open-framework Templated Structures
Subtask 4.3.4: TDF Simulations of the Structure of the Active Site(s)

Task 5. Materials Preparation

Task 5.1 Development of Si Templated Charge Transfer Salt (CTS) Catalyst System
Task 5.2 ORR Catalysts Based on MOFs
Task 5.3 Controlling Hydrophobicity
Task 5.4 Catalyst Scale up

Task 6. Optimization of Electrode Structure and Membrane Electrode Assemblies

Task 6.1 Development of New Methodologies for Implementing Membrane Electrode Assembly
Task 6.2 Electrode Catalyst Layer Optimization

Task 7. Fuel Cell Testing and Initial Durability Measurements

Task 7.1 Post Mortem Analysis of MEA's
Task 7.2 MEA Testing and Validation
Task 7.3 Fuel Cell Testing Based on DOE Test Protocols for Automotive

Task 8. Mechanistic Studies (Ex-Situ and In-Situ Spectroscopy and Modeling)

Mechanistic studies will be extended to down-selected catalysts for evolution of a predictive model on electrocatalytic pathway and degradation mechanism.

Task 8.1 Catalyst Evaluations
Task 8.2 In-situ Measurements Electrocatalytic Pathways in Down-selected Catalysts

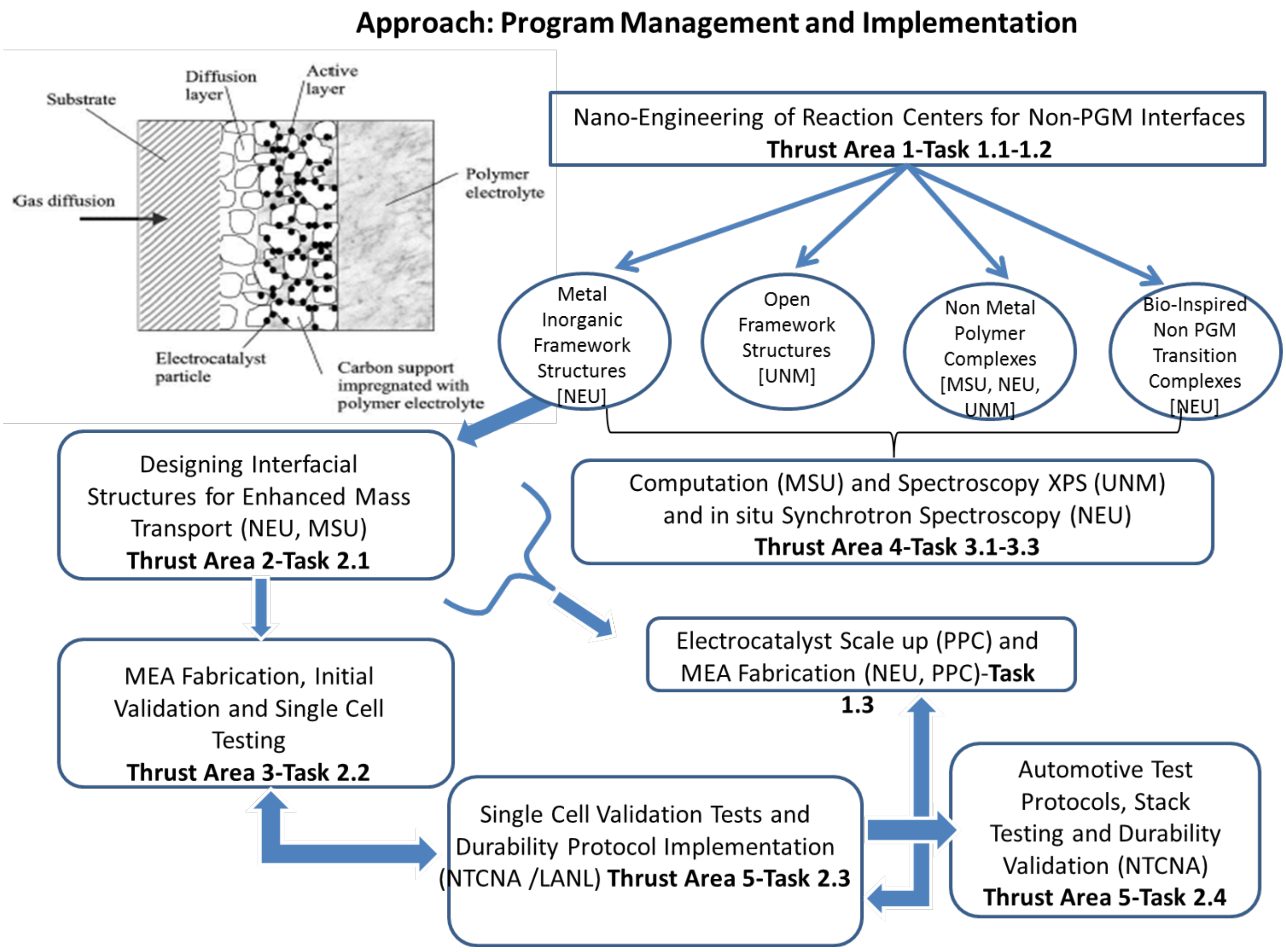

Scheme 1. Task flow in Spire Program.

WORK PERFORMED

Task 1/5. Materials Preparation

Task 1.1 Development of Poly-nuclear Reaction Centers

Proteins are very efficient for catalyzing the reduction of oxygen to water with porphyrin-based active sites. Scientists have tried to mimic this model when developing non-platinum group metal (Non-PGM) electrocatalysts for ORR.[1] Jasinski[2] was the first to report ORR catalytic activity using cobalt pthalocyanine, but these materials were only able to catalyze the $2e^-$ reduction of oxygen to hydrogen peroxide. Collman and Anson[3] believed that mononuclear complexes were incapable of delivering four electrons and developed a binucleating ligand that oriented two cobalt centers in a face-to-face coordination. They proposed a mechanism in which each metal center would transfer 2 e^- and together the binuclear catalyst would carry out the full $4e^-$ reduction of oxygen. However, they found that the function of these binuclear catalysts were extremely sensitive to the geometry of the Co centers. Amide bridges of different linkages were used to prepare binuclear oxygen reduction catalysts with an interporphyrin distance between 4-7 Å, and the dimer linked at 4 Å was the most efficient at the full 4e- reduction of oxygen. The following two decades focused on the structural aspects of these binuclear oxygen reduction catalysts. More recently, Nocera *et al*[4] developed a material that allowed them to investigate the effect of the electronic environment and found that targeted proton delivery was essential for the $4e^-$ reduction pathway.

Despite the promising results initially obtained with Co-based non-PGMs, most of the recent progress of non-PGMs in acidic media has been made with Fe-based materials. Even though the activity of Fe-based non-PGMs has approached that of Pt-based materials, stability is still an issue and some work has shown that adding Co enhances the stability.[5] Despite the growing literature on non-PGM electrocatalyst, very few publications have focused on Co-based electrocatalysts. Another benefit of Co-based catalysts is addressing the concern of the Fe ions participating in a Fenton type process that culminates in peroxide initiated free radical formation, that would severely inhibit the lifetime of the device.

This work as a part of the project aims to develop a binuclear Co-catalyst by investigating the effect of heat treatment temperature and Co-coordination on ORR activity in the acidic media. Synthesis of the desired structure was confirmed with hydrogen nuclear magnetic resonance (^1H NMR) and X-ray diffraction (XRD). Thermogravimetric analysis (TGA) was used to observe the effect of high temperature on degradation of the material and based on these results a window of heat treatment temperatures was chosen. Structural changes were observed at each distinct heat treatment temperature and changes to the Co-coordination were observed with X-ray absorption spectroscopy (XAS). ORR activity was tested using the rotating ring disk electrode technique that allowed simultaneous observation of ORR activity with the production of the undesired peroxide intermediate. The most active catalyst was then chosen for further studies that observed the effect of loading and pH to better understand the ORR mechanism.

Catalyst Synthesis

The synthesis of the cobalt dinuclear electrocatalyst was comprised of several steps: (1) organic synthesis of the 2,6-Bis{[bis(2-pyridylmethyl)amino]methyl}-4-*tert*-butylphenol (Hbpbp) ligand, (2) inorganic synthesis of $\{[Co^{III}_2(bpbp)\text{-}(O_2)]2bdc\}(PF_6)$ (Co_2bpbp), (3) ball milling of Co_2bpbp with a functionalized carbon support and (4) heat treatment of Co_2bpbp/Carbon mixture.

Hbpbp was synthesized according to a method previously reported.[6] *p*-formaldehyde (1.55 g, 0.0517 mol) and 4-tert-Butylphenol (1.994 g, 0.0133 mol) were dissolved in ethanol (25 mL) at room temperature with stirring in flask A. In flask B a solution of N,N-bis(2-pyridylmethyl)amine (10 g, 0.0503 mol) was added to water (50 mL) at room temperature. Flask B was added to Flask A and stirred at reflux temperature (82 °C) for 3 days. The two-pahse reaction mixture was cooled to room temperature and separated between water (100 mL) and dichloromethane (CH_2Cl_2; 200 mL) in a separatory funnel. The aqueous phase (yellow and opaque) separated from the organic phase (brown and transparent) that settled at the bottom of the funnel. The organic phase was removed and the aqueous phase was extracted with dichloromethane (3x50 mL). The combined organic phase was dried with anhydrous sodium sulfate. Solvent was isolated with a vacuum filter and removed with a rotary evaporator to isolate a brown-oil. The brown-oil was chromatographed on a silica gel column using acetone as the eluent to afford the crude product after removing solvent with rotary evaporator (yellow solid; 5.91 g, 78% yield). Crude product was recrystallized with diethyl ether and petroleum ether (700 mL) to afford Hbpbp (white crystals; 3.93 g, 57 % relative to the crude product). ^1H NMR (250 MHz): δ 1.27 (s, 9 H), 3.82 (s, 4 H), 3.90 (s, 8 H), 7.08 (m, 1H), 7.19 (s, 2 H), 7.48-7.61 (m, 8 H), 8.52 (m, 4 H), 10.80 (s, 1H).

Co_2bpbp was synthesized according to previously reported method.[7] The Hbpbp (102mg, 0.18 mmol) was dissolved in acetone (25 mL) in beaker A. Cobalt (II) nitrate (103 mg, 0.32 mmol) was dissolved in water (5 mL) in beaker B. Beaker B was added to beaker A to form a red-brown solution. Sodium 1,4-benzenedicarboxylate (19 mg, 0.10 mmol) was dissolved in water (3 mL) then added to the reaction mixture to form a dark-brown solution. Ammonium hexafluorophosphate (59 mg, 0.36 mol) was dissolved in water (2mL) and added to the reaction mixture. The reaction mixture was left on the benchtop to slowly evaporate in air at room temperature to yield Co_2bpbp (black crystals; 0.14 g, 65% yield) that were isolated by vacuum filtration.

The commercial carbon (Ketjanblack EC-600JD (K_{600}), Akzo Nobel) was purified and functionalized prior to catalyst synthesis. In order to remove any metallic impurities, K_{600} was combined with 6 M hydrochloric acid and allowed to stir for 24 hours at room temperature. The acid washed K_{600} was isolated by vacuum filtration and washed with copious amounts of water. Following a previously published method to functionalize the carbon support,[8] the acid washed K_{600} was combined with 70% nitric acid and stirred for 24 hours at reflux temperature (80 °C). The functionalized K600 (F-K_{600}) was isolated by vacuum filtration, washed with copious amounts of water and dried in a vacuum oven for 24 hours at 80 °C.

The catalyst precursor was generated by mixing Co_2bpbp with F-K_{600} in the mass ratio 1:1 and ball milling for 30 minutes (Co_2bpbp/F-K_{600}). The resulting powder was subjected to one heat treatment in argon at various temperatures (300-900 °C) with a 2 hour dwell time.

Rotating Ring Disk Electrode (RRDE) Measurements

Perchloric acid electrolyte (0.1 M) was prepared using double-distilled 70% perchloric acid (GFS Chemicals), sulfuric acid electrolyte (0.5 M) was prepared using double-distilled 98% sulfuric acid (GFS Chemicals) and potassium hydroxide electrolyte (0.1 M) was prepared using pellets (Alfa Aesar). Electrochemical measurements were carried out on glassy carbon (GC) disk (5.61 mm diameter, Pine Instruments) that was polished with 0.05-micron alumina paste (Buehler, Lake Bluff, IL) and then sonicated in distilled water and Isopropyl alcohol. Catalysts inks were prepared by dispersing the catalyst in a volume of 1:1 Millipore water:isopropyl alcohol with 10 vol% of 5 wt% Nafion® as a binder. The ink solution was then sonicated approximately 60 minutes to get a uniform suspension. A small volume of the catalyst ink was deposited on the GC substrate to obtain a non-PGM loading of approximately 200-600 $\mu g/cm^2$. All electrochemical measurements were carried out at room temperature (20-25 °C) in a standard electrochemical cell (Chemglass) with an acid or base electrolyte using a rotating disk electrode (RDE) setup from Pine Instrument Company connected to an Autolab bipotentiostat (PGSTAT302N). Cyclic voltammetry was run on non-PGM catalysts in 0.1 M perchloric acid ($HClO_4$), 0.5 M sulfuric acid (H_2SO_4) and 0.1M potassium hydroxide (KOH) bubbled with argon. ORR was investigated by the RDE technique after bubbling oxygen in the electrolyte solution followed with rotations at 100, 400, 900, 1600 and 2500 rpm. The ring electrode was held at 1.3 V vs RHE in acidic electrolyte and 1.1 V vs RHE in alkaline electrolyte. Scans were recorded at 20 mV/s and all potentials are referenced to a reversible hydrogen electrode (RHE) scale made from the same solution as the electrolyte. The percentage of H_2O_2 was measured according to previously reported method.[9]

Physicochemical Characterization

X-ray diffraction was performed on a Rigaku (model Ultima-IV) diffractometer with Cu Kα radiation (λ=1.5418 Å) at 40 kV and 40 mA. The scan speed was 2-20 seconds and the step size was 0.1°. Thermogravimetric analyses (TGA) were performed on TA Instruments SDT Analyzer Q600 from 22-1100°C with a ramp rate of 5°C/min and dwelling for 5min at maximum temperature. All studies were conducted under argon atmosphere, with a flow rate of 100mL/min. Scanning electron microscopy was performed on a Hitachi S-4900 FSEM instrument with an accelerating voltage of 3-5 keV with samples mounted on a carbon adhesive stub attached to an aluminum sample stage. Elemental composition was collected on Energy Dispersive X-ray Analysis (EDAX) Genesis with Hitachi S-4900 FSEM at an accelerating voltage of 15 keV.

X-ray Absorption Spectroscopy (XAS) Measurements

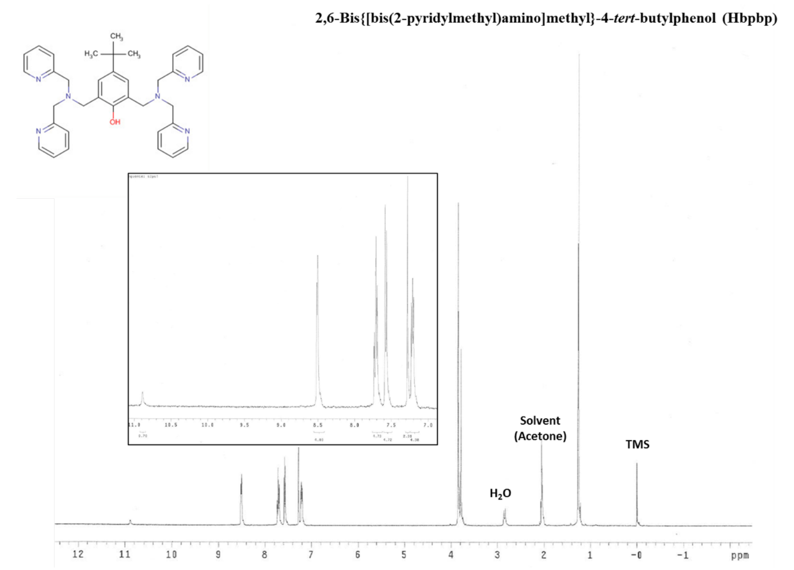

Figure 1.1: ^{1}H NMR Confirmation of Hbpbp Ligand. ^{1}H NMR spectrum of Hbpbp ligand powder from described reaction was dissolved in acetone measured at 400 M Hz.

The XAS studies at the Co K-edge (7709 eV) were performed at X3B beamline of National Synchrotron Light Source (NSLS, Brookhaven National Laboratory, NY). The electrode inks for the EXAFS electrodes were composed of 1:1 (wt%) 18.2 MΩ purity deionized water (Millipore) and 2-propanol (HPLC-grade, Aldrich), a 5 wt% Nafion solution (Aldrich), and the catalyst powder. The composition was chosen to give a final electrode with a dry Nafion loading of 5 wt%. The ink was hand-painted onto a Zoltek® carbon cloth and dried for 15 minutes in a 65°C vacuum oven between coats. The final cobalt geometric loadings were chosen to give 0.05 edge heights at the Co K–edge. A specially designed spectro-electrochemical cell was utilized and has been described previously.[10] The Co K-edge spectra were collected in fluorescence mode with a 32-element Ge solid state detector as a function of potential in the range 0.1 – 0.9 V vs. RHE.). Data were collected in fluorescence mode with a Co reference foil positioned between I_2 and I_3 as a reference. The voltage cycling limits were 0.05 to 1.10 V vs. RHE. Data collection was performed at the chosen potentials held during anodic sweeps. A pseudo steady-state was established by holding the cell for approximately 5 minutes before collecting the spectra. The electrolyte, 0.1 M $HClO_4$, was saturated with either argon or oxygen. Athena[11] and Artemis[12] programs were used to process and fit the data. IFEFFIT suite[11] was used to calibrate, align and normalize the scans. FEFF6 code[13] was used to calculate scattering paths to model the $\chi(R)$ transforms.

The dinucleating ligand Hbpbp was synthesized according to a previously published method and its structure was confirmed by ^{1}H NMR (Figure 1.1). The combination of $Co(NO)_3$ with Hbpbp in a mixture of acetone and water allowed the formation of a dinuclear unit with two Co^{III} centers coordinated by two pyridyl and one amine nitrogen from the $bpbp^-$ ligand. Addition of Sodium 1,4-benzenedicarboxylate (Na_2bdc) and ammonium hexafluorophosphate (NH_4PF_6) promoted the formation of a tetranuclear complex cation, where two of the dinuclear units were bridged by the coordination of the carboxylate O atoms from the bdc^{2-} ligand with the Co^{III} centers(Figure 1.2, inset).

A metal-organic host material formed from the edge-to-face interactions between one of the pyridyl rings of the $bpbp^-$ ligand of one cation with the bdc^{2-} ligand on an adjacent cation, resulting in parallel chains that stack in zigzag layers alternating with counteranions (PF_6^-).[7] A comparison of the powder XRD pattern of the material synthesized in our lab, $[Co_4(O_2)_2(bpbp)_2(BDC)](PF_6)_4$ (Co_2(bpbp)), with the published pattern (Figure 1.2) confirmed formation of the metal organic host material.

Following synthesis of Co_2(bpbp), a high-temperature heat treatment was employed to create a viable catalyst by surmounting the inherently insulating nature of the material. Determining an optimum heat treatment temperature is an integral first step in developing a new non-PGM electrocatalyst for ORR. TGA was performed on Co_2(bpbp) under nitrogen flow from ambient temperature up to 1100 °C to mimic the conditions of the high-temperature heat treatment step. The TGA trace revealed an initial mass loss below 200 °C due to removal of guest species (water and oxygen). Around 300 °C a small mass loss is observed and corresponds with the melting

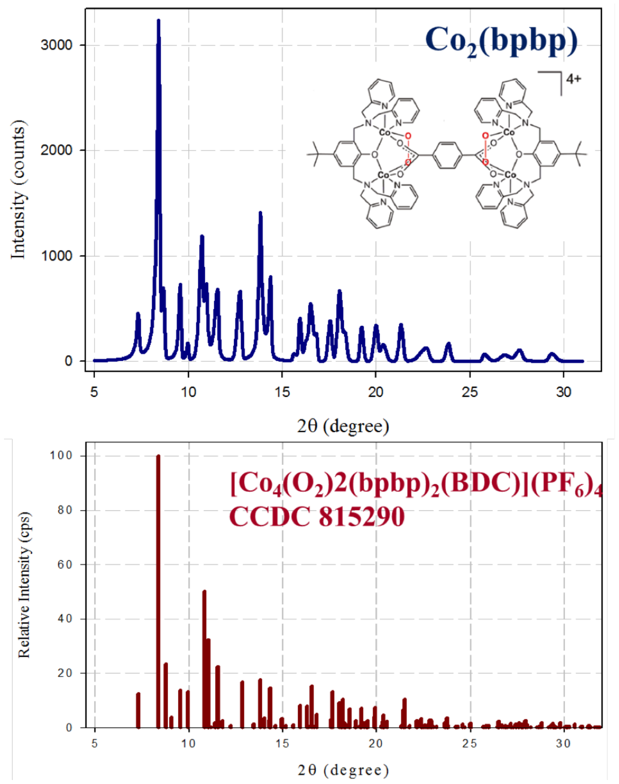

Figure 1.2: X-ray Diffraction Confirmation of Co_2(bpbp). Powder pattern of $[Co_4(O_2)_2(bpbp)_2(BDC)](PF_6)_4$ synthesized compared to published pattern.

point of the hexafluorophospahte anion. A steep drop around 400 °C accounts for most of the mass loss of the material and could signify decomposition of the metal organic host material. There is a final drop from 700-900 °C, resulting in an overall mass loss of ~45 wt%. Previous non-PGM reports have shown that the best heat treatment temperature to form active non-PGM electrocatalysts can range from 500-1000 °C, but it is dependent on the precursor material utilized. Based on the TGA results it was apparent that the significant transitions took place at three distinct temperatures (300, 400 and 900 °C), which led us to generate electrocatalysts at various temperatures in the range of 300-900 °C.

Co_2(bpbp) was mixed with a functionalized carbon black support (Co_2(bpbp)/F-K_{600}) and heat treated under an argon flow with a 2 hour dwell at the respective temperatures. Changes in elemental composition were monitored by energy dispersive X-ray analysis (EDS) as a function of heat treatment temperature (Table 1.1). Heat treatment at the lowest temperature, 300 °C, produced a 30% mass loss mostly due to evaporation of the adsorbed water and oxygen. Following the first heat treatment at 300 °C, fluorine was no longer detected, confirming the TGA results that the hexafluorophosphate anion decomposed around 300 °C. Increasing the heat treatment temperature to 400 °C produced very little changes in the elemental composition or mass loss. An additional increase of heat treatment temperature up to 600 °C induced degradation that accounted for 17% of the overall mass loss and

Temp.	% C	%O	%F	%P	% Co	% mass loss
No heat treatment	74.11	8.07	4.67	4.09	8.84	—
300°C	75.6	6.66	0	3.86	13.3	30.40
400°C	76.51	6.59	0	3.99	11.33	31.45
600°C	84.32	0	0	2.86	11.91	39.32
800°C	79.78	0	0	3.74	16.47	41.16
900°C	82.74	0	0	3.24	12.79	46.6

Table 1.1: Elemental Analysis of Co_2(bpbp). Quantification of elemental components of $[Co_4(O_2)2(bpbp)_2(BDC)](PF_6)_4$ mixed with functinalized carbon black and as a function of heat treatment temperature. Measurements were taken with an accelerating voltage of 15 kEV on multiple on 5 different areas of sample and quantities are an average.

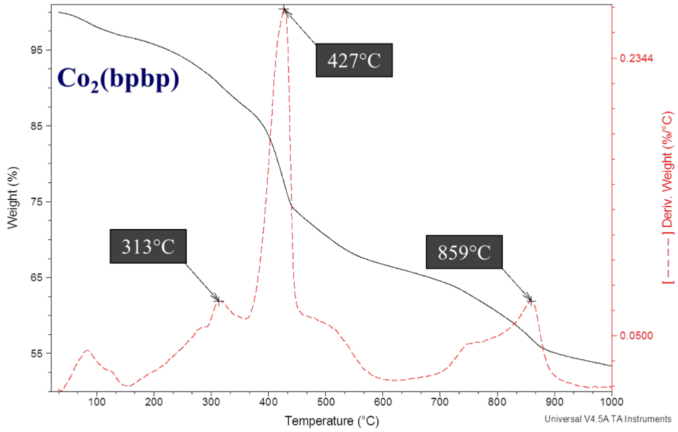

Figure 1.3: Thermogravimetric Analysis of Co_2(bpbp). Thermogravimetric analysis of $[Co_4(O_2)2(bpbp)_2(BDC)](PF_6)_4$ from ambient temperature up to 1000 °C. Measurement was run under argon with 100 mL/min flow rate and heated at a ramp rate of 5 °C/min.

oxygen was no longer detected. Combining these results with our TGA we believe the tetranuclear cation decomposes above 400 °C and the resulting material is predominantly comprised of carbon, phosphorous and cobalt. Increasing the heat treatment temperature up to 800 °C and 900 °C produced very little changes in the elemental composition, but promoted further material degradation that accounted for 16% of the overall mass loss. Heat treatment up to 900 °C produced an overall mass loss of ~45%, but the Co was stable throughout the heat treatment of Co_2(bpbp)/F-K_{600} as evidenced by the increase in the Co wt%.

XRD analysis was employed to monitor phase changes to the crystalline structure at the different heat treatment temperatures. The XRD pattern of Co_2(bpbp)/F-K_{600} (Figure 1.4) matches the pattern of Co_2(bpbp) alone, indicating the ball milling with the functionalized carbon does not disturb the structure of the metal-organic host material. Following heat treatment at 300 °C, the powder pattern of the catalyst no longer shows any evidence of the original crystal structure and is instead characterized by diffraction lines of graphite. The higher heat treatment temperatures led to the formation of several new diffraction lines that indicate the formation of a new cobalt phase (cobalt phosphide-Co_2P (Pnma(62)). These results are supported by the EDS elemental analysis that shows phosphorous and cobalt are stable in the entire heat treatment temperature range investigated.

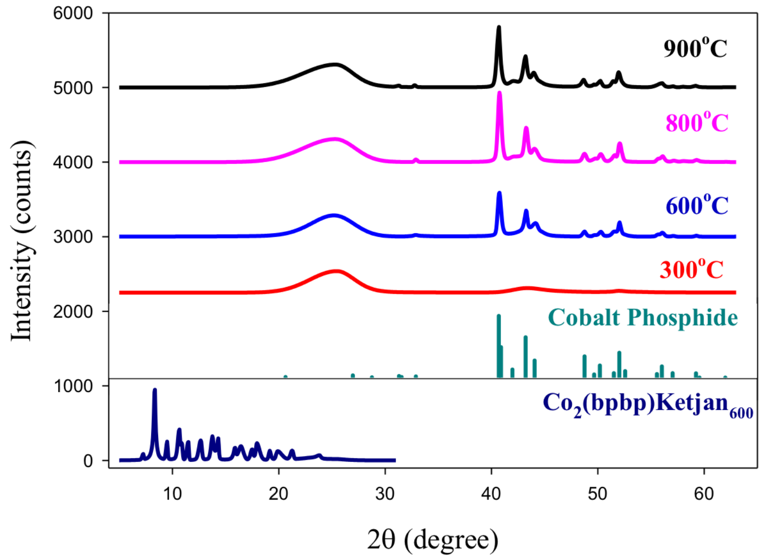

Figure 1.4: X-ray Diffraction Monitoring Effect of Heat Treatment Temperature. Powder patterns comparison of Co_2(bpbp) mixed with functionalized carbon black, after heat treatment at specified temperature and diffraction pattern of cobalt phosphide standard.

XAS was used to further probe the local coordination of the cobalt before and after the various heat treatment temperatures. Fourier transform (FT) of the extended X-ray absorption fine structure spectra (EXAFS) of the Co K-edge is shown in Figure 1.5, right. The FT-EXAFS of Co_2(bpbp)/F-K_{600} before heat treatment is characterized by a peak at ~1.5 Å due to Co-N/O scattering. After heat treatment at 300 °C the Co-N/O peaks shifts to higher radial distances and continues to shift as the heat treatment temperature is increased. At 600 °C is appears the Co-N/O structure starts to degrade and evidence of a Co-Co structure appears. Heat treatment of

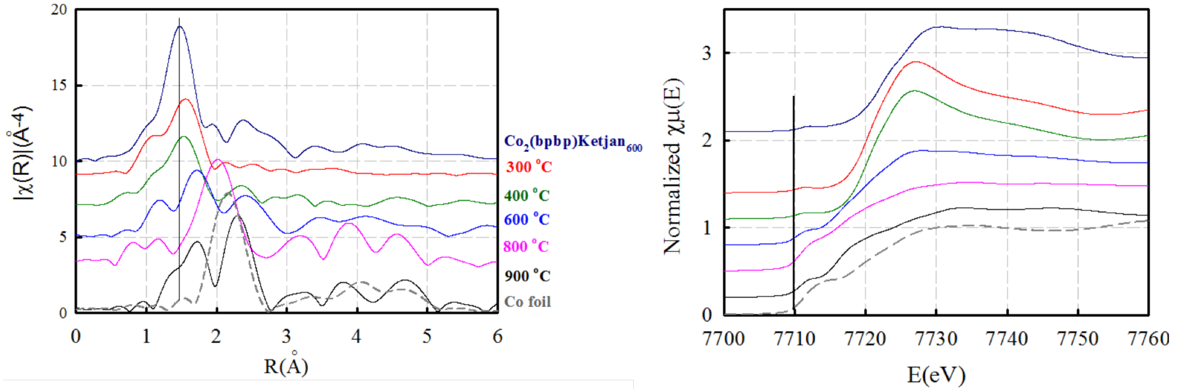

Figure 1.5: X-ray Absorption Spectroscopy Monitoring Effect of Heat Treatment Temperature. Fourier transform EXAFS and XANES of Co_2(bpbp) mixed with functionalized carbon black and after heat treatment at specified temperature compared with reference Co foil.

Co_2(bpbp)/F-K_{600} at 800 and 900 °C produces a peak at ~2.0 Å ,as well as displaying long range order. The multi-component nature of heat treated of Co_2(bpbp)/F-K_{600} makes the EXAFS fitting impossible, but a qualitative comparison with the FT-EXAFS of the Co foil indicate the peak at ~2.0 Å is due to Co-Co scattering. The FT-EXAFS results indicate that Co-N/O structure is decomposed and most of the cobalt ions are converted to metallic cobalt at the higher heat treatment temperatures. X-ray absorption near-edge structure (XANES) spectra (Figure 1.5 b) also confirm the transformation of the Co-N/O structure to a Co-Co/O structure as evidenced by the XANES of Co_2(bpbp)/F-K_{600} heat treated at 800 and 900 °C is very similar to the XANES of the Co foil.

Electrochemical Performance

The electrocatalytic activity for the oxygen reduction reaction (ORR) of Co_2(bpbp)/F-K_{600} catalyst was studied using the RRDE technique. Reduction of oxygen can proceed through either a $4e^-$ or $2e^-$ path, and a second working electrode allowed us to monitor the production of peroxide from the undesirable $2e^-$ path. The RDE polarization curves in oxygen saturated acidic electrolyte (0.5 M H_2SO_4) and corresponding ring response of the Co_2(bpbp)/F-K_{600} catalyst is shown in Figure 1.6. Without heat treatment Co_2(bpbp) shows now activity for ORR over what is achieved with the functionalized carbon black support. Following heat treatment Co_2(bpbp) shows activity for ORR, but for all the tested electrocatalyst no clear diffusion limited current was achieved. The diffusion limiting current ($i_{\lim}$) is defined by the Levich equation:

$$i_{\lim}=0.62nFD^{2/3}v^{-1/6}C_o \qquad (1.1)$$

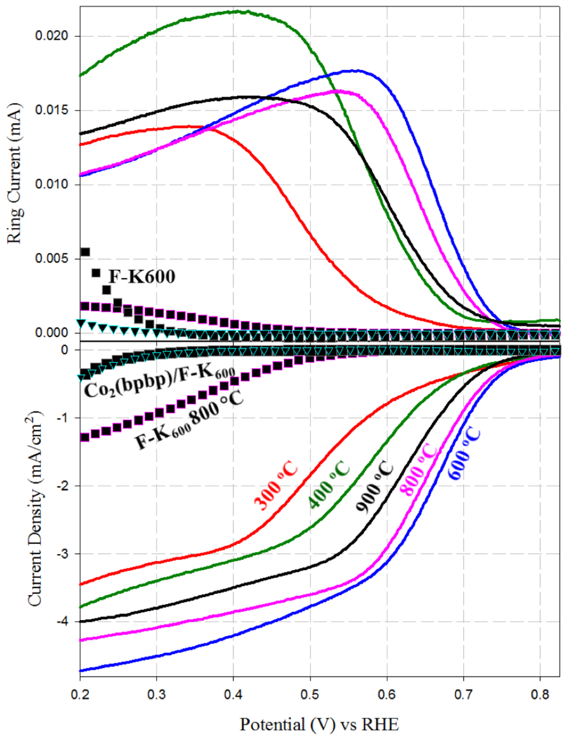

Figure 1.6: RRDE Catalyst Heat Treatment Study. Disk- and tring-currents measured during ORR on Co_2(bpbp)/F-K_{600} catalyst at various heat treatment temperatures in O_2 saturated 0.5 M H_2SO_4 electrolyte at 20 mV/s with rotation rate of 900 rpm at room temperature. E_{ring}=1.3 V vs RHE.

where *n* is the number of electrons transferred, *F* is the Faraday constant, *D* is the diffusion coefficient of O_2, *v* is the kinematic viscosity and *Co* is the concentration of O_2 in the electrolyte. Lack of a clear diffusion limiting current indicates that the reaction is under kinetic control possibly due to poor distribution of active sites.[14] As the heat treatment temperature is increased from 300 to 600 °C the electrocatalyst performance is correspondingly increased as evidenced by the steady improvement of the half-wave potential ($E_{½}$) (0.49 *vs* 0.64 V). For the catalyst generated in this temperature range (300 to 600 °C), the onset of peroxide oxidation detected at the ring electrode coincides with the onset of ORR at the disk electrode indicating that peroxide intermediate that is formed is not stabilized by Co_2(bpbp)/F-K_{600} . When the heat treatment temperature is further increased to 800 °C the electrocatalyst performance degrades slightly and the $E_{½}$ shifts cathodically (0.63 *vs* 0.64 V. After heat treatment at 900 °C the electrocatalyst performance degrades more severely, which interestingly coincides with the material degradation witnessed with the TGA analysis. The ORR activity of F-K_{600} heat treated at 800 °C indicates that the ORR activity of Co_2(bpbp)/F-K_{600} stems from the presence of Co.

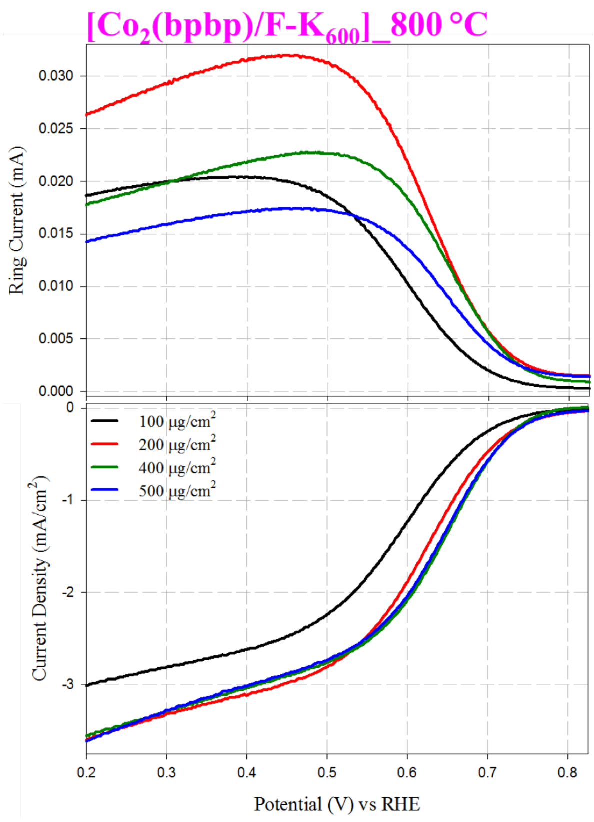

Figure 1.7: RRDE Catalyst Loading Study. Disk- and ring-currents measured during oxygen reduction reaction (ORR) on Co_2(bpbp)/F-K_{600}-800 in O_2 saturated 0.5 M H_2SO_4 electrolyte at 20 mV/s with rotation rate of 1600 rpm at room temperature. E_{ring}=1.3 V vs RHE.

Based on these original performance results presented above, Co_2(bpbp)/F-K_{600}-800 was selected for further study. The porosity and thickness of an electrode will determine the current-potential behavior in a RDE system.[15] Due to the porous nature of Co_2(bpbp)/F-K_{600}-800 it was important to work with the optimal catalyst loading. Shown in Figure 1.7 are the RRDE polarization curves at 1600 rpm in oxygen saturated acidic electrolyte (0.5 M H_2SO_4) with catalyst loadings ranging from 100 to 500 µg/cm². An increase in the reduction current is observed when the loading is increased from 100 to 200 µg/cm², but further increases in the loading did not produce a higher reduction current. However, the peroxide oxidation at the ring showed more variation with increased loading. Increasing the loading from 100 to 200 µg/cm² caused an increase in the peroxide detected, which is most likely due to the increase in the amount of O_2 reduced. When the loading was further increased from 200 to 500 µg/cm², the magnitude of the reduction current remained the same while the amount of peroxide detected at the ring decreased. These results indicate that above a loading of 200 µg/cm² the amount of peroxide released from the catalyst layer decreased. Since all the other parameters remain constant it can be concluded that the increased catalyst layer thickness changes the diffusion path for the H_2O_2 product and allows the H_2O_2 molecules to further react either electrochemically or chemically. Co_2(bpbp)/F-K_{600}-800 may contain catalytic sites that electrochemically reduce the peroxide according to the following equation:

$$H_2O_2 + 2H^+ + 2e^- \rightarrow 2H_2O \qquad (1.2)$$

The catalytic sites can also chemically decompose the peroxide product according to the following equation:

$$2H_2O_2 \rightarrow 2H_2O + O_2 \qquad (1.3)$$

The chemical decomposition of peroxide will produce water as well as oxygen, and the oxygen can be electrochemically reduced back to peroxide according to the following equation:

$$O_2 + 2H^+ + 2e^- \rightarrow H_2O_2 \qquad (1.4)$$

With lower catalyst loadings the catalyst layer is thinner and most of the H_2O_2 is produced near the electrolyte bulk, enhancing the possibility of the H_2O_2 diffusing and being oxidized at the ring electrode. Based on these results a loading of 200 µg/cm^2 was used for the following studies into the ORR mechanism.

Co_2(bpbp)/F-K_{600}-800 was used for our RRDE studies and compared to Pt/C to estimate electrocatalytic activity for ORR. Pt/C is the benchmark cathode catalyst and is known to proceed principally through the 4 e^- path in both alkaline and acidic media, as long as the surface is free of poisonous adsorbates.[16] The ORR polarization plots of Co_2(bpbp)/F-K_{600}-800 and Pt/C in acidic and alkaline media are shown in Figure 1.8. In alkaline media Co_2(bpbp)/F-K_{600}-800 had an onset potential of 0.84 V and the oxidation of the peroxide intermediate (HO_2^-) detected at the ring electrode corresponds with generation of reduction current at the disk. Unlike the catalyst tested in acidic media, Co_2(bpbp)/F-K600-800 established a well-defined limiting current in alkaline media that was higher in magnitude than what was produced in acid. Despite the different pH range of the electrolyte tested, the diffusion and concentration of oxygen in the electrolyte are expected to remain constant. Therefore the changes in the diffusion limiting current indicate an increase in the number of electrons transferred in the reaction. It could be possible the primary active site of Co_2(bpbp)/F-K_{600}-800 produces the peroxide intermediate, but the peroxide is further reduced by a secondary active site and ORR proceeds through a series of two $2e^-$ reductions resulting in an overall 4e- reduction. Conversely, Pt/C had an onset of ~1 V and the onset of oxidation of the peroxide intermediate was not detected until ~0.45 V. Peroxide oxidation at 0.45 V observed on Pt/C electrocatalyst has been attributed to $2e^-$ reduction of oxygen by the quinone functionalities of the carbon support.[17] Therefore, the active sites of Pt/C are able to stabilize the peroxide intermediate more effectively than Co_2(bpbp)/F-K_{600}-800. When the same experiment was conducted in acidic media Co_2(bpbp)/F-K_{600}-800 displayed poorer performance in the low pH environment. The onset of ORR on Co_2(bpbp)/F-K_{600}-800 was shifted cathodically by 60 mV (0.78 vs 0.84 V) when compared with its performance in alkaline media. The peroxide intermediate becomes a neutral species (H_2O_2) when switching to the low pH environment, decreasing its stability on metal-ion active sites (Co-N_4), such as those resembling the poryphyrin active sites of proteins. The onset of peroxide oxidation detected at the ring in acidic media still coincides with the Co_2(bpbp)/F-K_{600}-800 catalyzed ORR detected at the

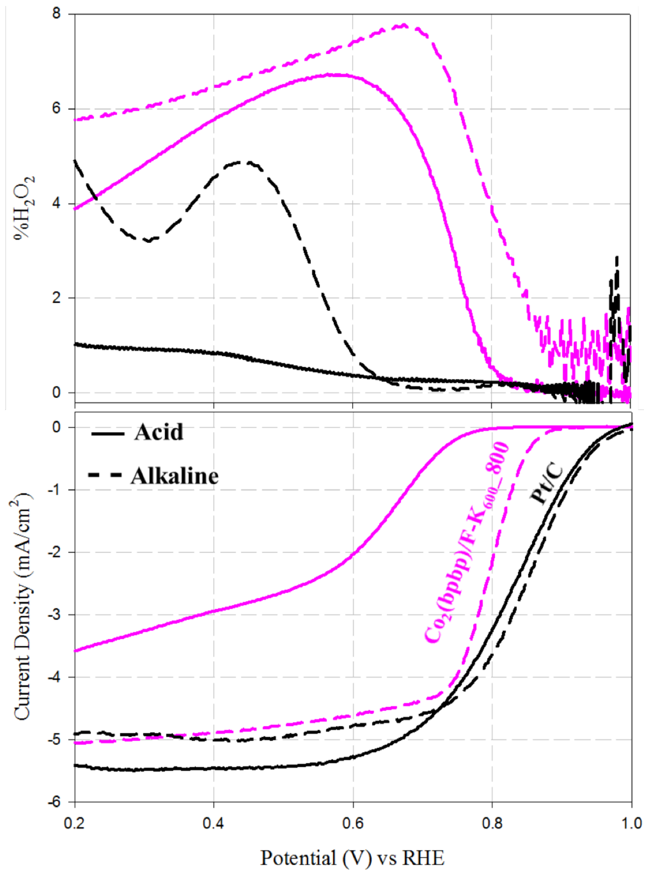

Figure 1.8: RRDE ORR Mechanism Study. Disk- and ring-currents measured during oxygen reduction reaction (ORR) on Tanka Pt/C and Co_2(bpbp)/F-K_{600}-800 in O_2 saturated 0.1 M KOH and 0.5 M H_2SO_4 electrolyte at 20 mV/s with rotation rate of 1600 rpm at room temperature. Alkaline E_{ring}=1.1 V vs RHE. Acid E_{ring}=1.3 V vs RHE.

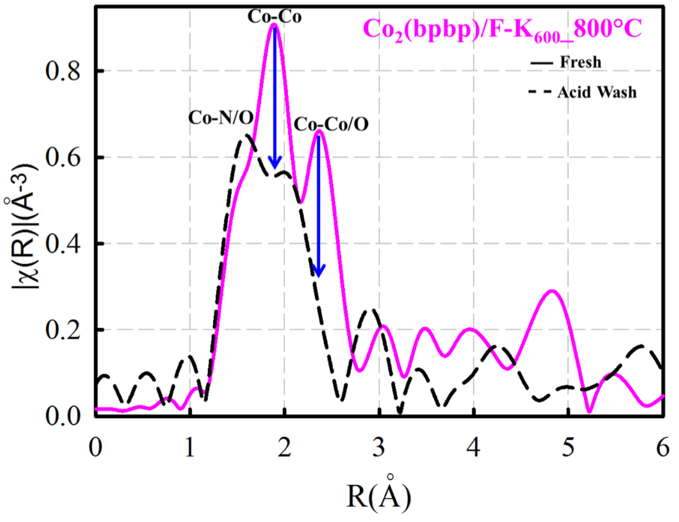

Figure 1.9: Stability of Cobalt Moities in Acid. Fourier transform of fresh $Co_2(bpbp)/F\text{-}K_{600}$-800 catalyst and acid washed $Co_2(bpbp)/F\text{-}K_{600}$-800 catalyst.

disk. However, the magnitude of the ring current is very similar in alkaline and acidic media, despite the difference in magnitude of the disk current. These results indicate that the primary active site of $Co_2(bpbp)/F\text{-}K_{600}$-800 still produces the peroxide intermediate in acidic media, but the peroxide is not further reduced by a secondary active site.

2.3.3 Investigation of a Secondary Active Site

The high temperature heat treatment of $Co_2(bpbp)/F\text{-}K_{600}$ generated cobalt metal, which is known to be thermodynamically unstable in the low pH environment. However, if the metallic moieties are protected they could survive the acidic environment. $Co_2(bpbp)/F\text{-}K_{600}$-800 was subjected to an acid wash to investigate the stability of the metallic moieties present after the high temperature heat treatment.

Shown in Figure 1.9 are the FT-EXAFS of fresh $Co_2(bpbp)/F\text{-}K_{600}$-800 and $Co_2(bpbp)/F\text{-}K_{600}$-800 after the acid wash. It can be seen that the peak at ~2.4 Å completely disappears and the peak at ~2.0 Å shows a decrease in intensity. Some of the Co NPs that are created at the higher heat treatment temperatures appear to be protected, while the metallic Co-moieties that are not protected are spontaneously oxidized when exposed to air. The Co-Co-O scattering of the oxidized Co NPs contribute the peak at 2.4 Å. The lack of protection around these moieties makes them vulnerable in the low pH environment and they are completely removed when washed in acid. However, some of the Co NP moieties are stable during the acid wash and their Co-Co scattering contribute to the peak at 2.0 Å.

Based on these XAS results, we investigated the effect of the acid wash of $Co_2(bpbp)/F\text{-}K_{600}$-800 on the ORR activity to better understand the involvement of the Co NPs in the ORR mechanism. RRDE measurements were taken on fresh $Co_2(bpbp)/F\text{-}K_{600}$-800 and catalyst that had been acid washed ($Co_2(bpbp)/F\text{-}K_{600}$-800-AW). Shown in Figure 1.10 are the ORR polarization plots and corresponding ring responses in acidic and alkaline media. The removal of Co NPs reduces ORR activity in acidic media as witnessed by a 20 mV increase in overpotential for ORR (0.76 vs 0.78 V). This potential loss is maintained throughout entire potential range and shifts the $E_{½}$ cathodically by 20 mV (0.59 V vs 0.61 V). Production of the peroxide intermediate still commences with the onset of ORR and removal of Co NPs has no effect on the amount of peroxide produced in the low pH environment. However, in alkaline media the removal of Co NPs has very different effect on the ORR activity. Despite an improvement in the onset potential by 40 mV (0.88 V vs 0.84 V), the $E_{½}$ shifts cathodically by 10 mV (0.78 V vs 0.79 V) and the diffusion limiting current is reduced by 10% (4.6 vs 5.1 mA/cm^2). The most drastic change due to the removal of Co NPs is the substantial increase in the amount of peroxide intermediate detected at the ring (20% vs 7.7%). It appears in alkaline media a secondary active site is able to further reduce the peroxide intermediate to yield the $4e^-$ reduction of oxygen. The Co-N moieties could initiate O_2 adsorption and complete the $2e^-$ reduction to HO_2^-, but the Co NPs act as a second active site that further reduce the peroxide intermediate to water. However, in acidic media of $Co_2(bpbp)/F\text{-}K_{600}$-800 is only capable of the 2e- reduction of oxygen since the peroxide intermediate formed by the Co-N moieties is not stabilized well enough to be further reduced. Although, the loading studies suggest that the Co NPs would still function as a secondary active site capable of further reducing peroxide if the peroxide pathway was altered by high-loadings.

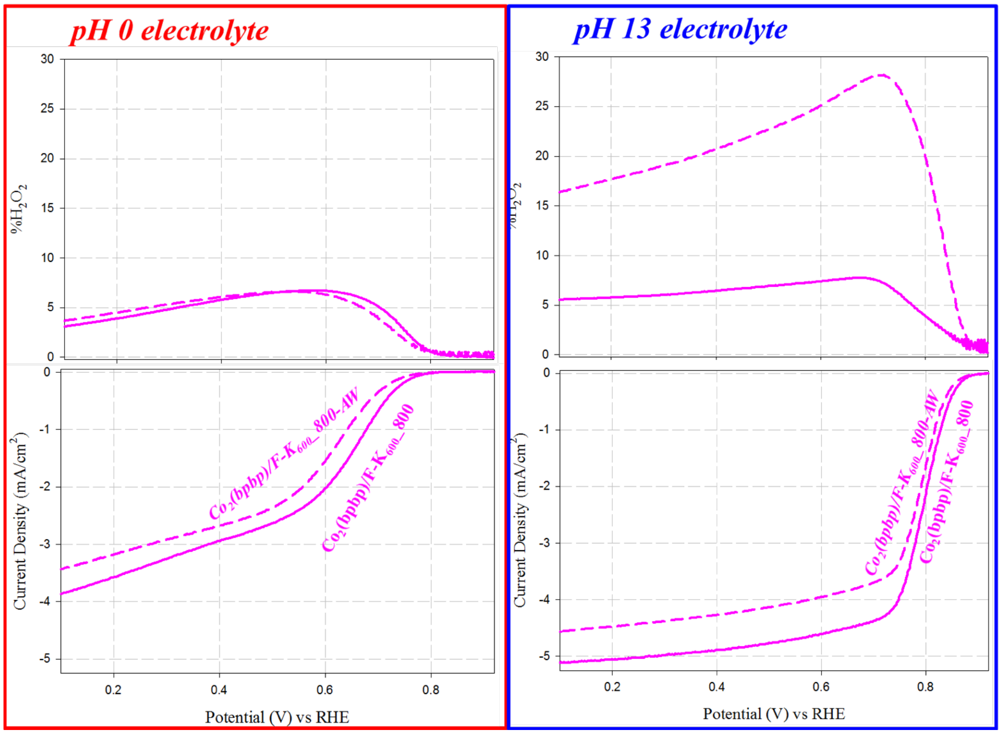

Figure 1.10: **RRDE Effect of Acid Wash on ORR Mechanism**. Disk- and ring-currents measured during oxygen reduction reaction (ORR) on fresh and acid washed Co_2(bpbp)/F-K_{600}-800 in O_2 saturated 0.1 M KOH and 0.5 M H_2SO_4 electrolyte at 20 mV/s with rotation rate of 1600 rpm at room temperature. Alkaline E_{ring}=1.1 V vs RHE. Acid E_{ring}=1.3 V vs RHE.

Conclusions

In this work we generated a Co-based non-PGM electrocatalyst by subjecting a tetranuclear cobalt cation to a high temperature heat treatment in inert atmosphere. Catalyst heat treated above 600 °C were the most active for ORR and were comprised of Co-N and Co NP moieties. Co_2(bpbp)/F-K_{600}-800 is an effective catalyst for the $2e^-$ reduction of oxygen in acidic electrolyte and enhanced stability of the peroxide intermediate in alkaline media allowed the Co NPs to act as a secondary active site that allowed a series of two $2e^-$ reductions, resulting in an overall $4e^-$ reduction of oxygen to water in alkaline media. In acidic media the Co NPs moieties can still act as a second active site if high enough loadings are used to allow further reduction of the peroxide before it is released into the electrolyte.

Task 1.2 Open Framework Templated Structures

Recently, several research groups have reported significant progress in the synthesis of highly active and durable non-PGM cathode catalysts.[5,18-21] These catalysts contain transition metals (M) coordinated by nitrogen (N) inside a carbon matrix (C) and are symbolized as M–N–C catalysts. Non-templated synthetic approaches involve either (i) the dispersion of M and N precursors on pre-existing carbon supports, or (ii) one pot synthesis approach with M, N and organic or metal–organic precursors. Complementary to these synthesis approaches, a templated synthesis approach allows for the design of hierarchically-structured materials resulting in catalysts with an open-frame morphology. The group at University of New Mexico (UNM) introduced the sacrificial support method (SSM) and applied it to the templated syntheses of both PGM[22] and non-PGM catalysts.[23]

Catalyst Synthesis

The pore structures studied in this effort would be specifically tailored for understanding how reaction layer transport mechanisms work in the context of these templated structures. Two types of Non-PGM Fe-based catalysts were synthesized by substantially modified sacrificial support method (SSM). First, Fe-AAPyr catalysts was synthesized by initially calculated amount of low sur-face area fumed silica (L90, Cab-O-Sil®, Cabot, surface area~90 m^2g^{-1}) was mixed with $Fe(NO_3)_3 \cdot 9H_2O$ (Sigma–Aldrich) and4-Aminoantipyrine (AAPyr, Sigma–Aldrich) and in-house made carbon nanotubes (CNTs). Obtained mixture was subjected to dry mechanochemical treatment by ball-milling in plane-tary ball mill at 400 rpm for 1 h. The finely homogenized mixture of precursors was pyrolyzed in inert atmosphere of Ultra High Purity(UHP) nitrogen at flow rate of 100 mL min^{-1}, 975°C and 45 min. Sacrificial support was removed by means of 25 wt% of HF for 48 h. Powder was washed with deionized water until neutral pH. In order to remove un-washed volatile silica compounds, a sec-ond treatment in ammonia atmosphere was carried out at 1000◦Cand 25 min. As obtained Fe-AAPyr catalyst was used in present study. Scanning electron microscopy (SEM) and transmission elec-tron microscopy (TEM) images were obtained using Hitachi S-800and JEOL 2010 EX instruments, respectively. Surface areas were measured by N_2 adsorption BET using a Micrometrics 2360 Gemini Analyzer. A four-point BET analysis was performed using a saturation pressure of 640 mm Hg. Second, Fe-CTS catalysts were prepared by a modified sacrificial support method. First, a calculated amount of silica (Cab-O-Sil® M5P, surface area 125 m^2 g^{-1}) was dispersed in water using a high energy ultrasound probe. Then, suspension of nicarbazin (Nicarbazin, Sigma-Aldrich) in acetone was added to silica and sonicated for 20 minutes in an ultrasound bath. Finally, a solution of iron nitrate ($Fe(NO_3)_3*9H_2O$, Sigma-Aldrich) was added to SiO_2-CTS solution and ultrasonicated for 8 hours (the total metal loading on silica was calculated to be ~20wt.%). After ultrasonication, the viscous gel of silica and Fe-NCB was dried overnight at T=85 °C. The obtained solid was ground to a fine powder in an agate mortar and then subjected heat treatment (HT). The general conditions of HT were UHP nitrogen (flow rate of 100 cc min^{-1}), 20 deg min^{-1} temperature ramp rate. The experimental variable component of heat-time trajectory were temperatures and duration of HT (900 °C, 1 hour; 950 °C, 30 minutes and 950 °C, 1 hour). After heat treatment, silica was leached using 25 wt.% HF overnight. Finally, the Fe-NCB catalyst was washed with DI water until neutral pH was achieved and then dried at T=85 °C. A second heat treatment was performed at T=950 °C in reactive (NH_3) atmospheres.

Physical characterization

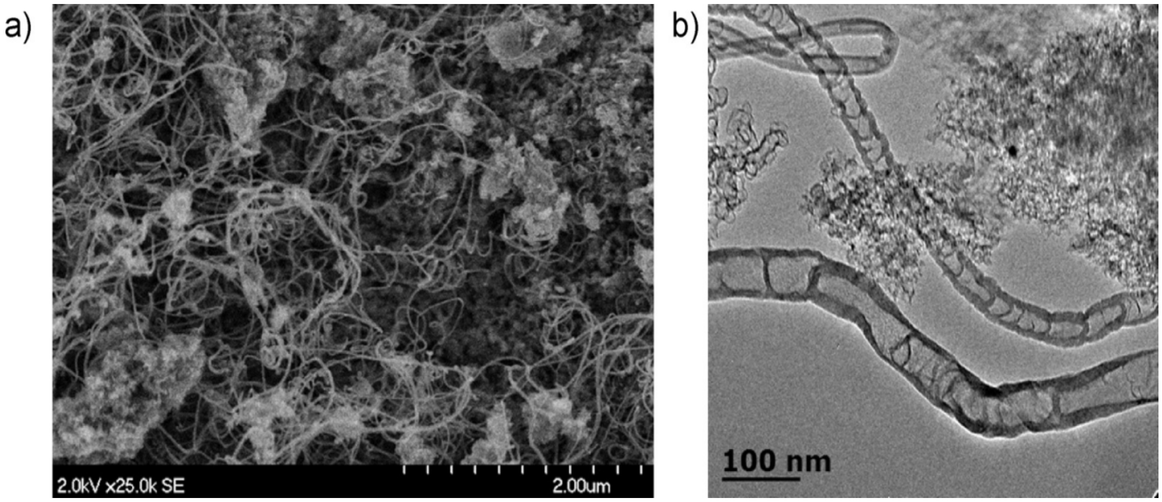

Figure 1.11. SEM (a) and TEM (b) images of Fe-AAPyr hybrid with CNTs catalyst.

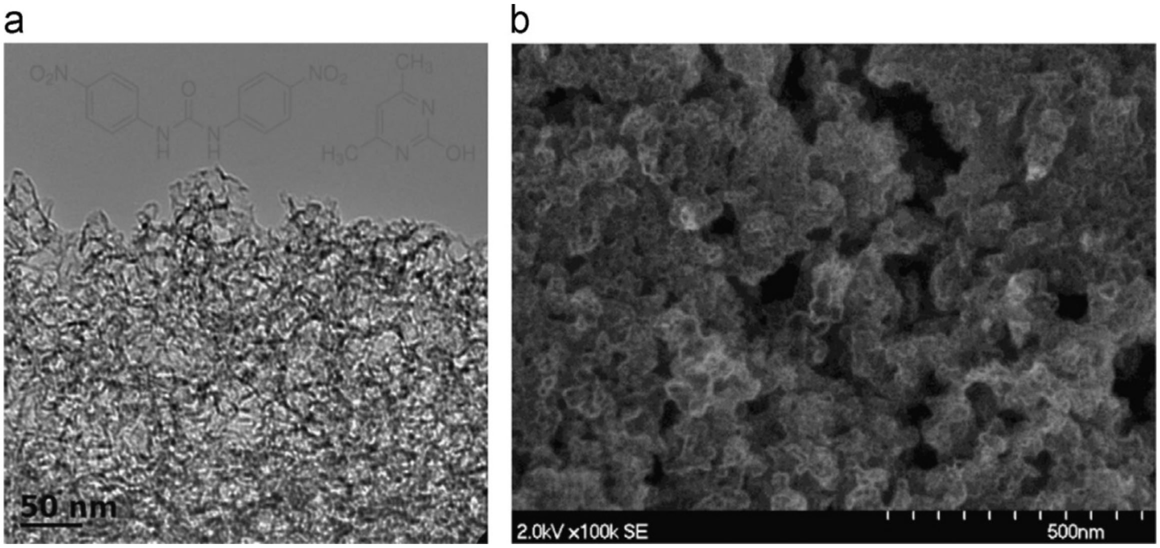

Figure 1.12. TEM (a) and SEM (b) images for the Fe-CTS catalyst synthesized at T=900 °C in N_2 for X minutes with Fe:CTS ratio1:8, second heat treatment at T=950 °C for 30 min in NH_3. Inset in (a) the chemical formula of the charge-transfer salt, nicarbazin.

As seen from Figure 1.11, Fe-AAPyr material possesses combination of open-framed structure as well as CNTs features. On the other hand, SEM images in Figure 1.12 show that the Fe-CTS catalyst has several levels of porosity originating from the removal of SiO_2 nanoparticles and from morphological defects formed during the decomposition of nicarbazin at high-temperature. TEM imaging (Figure 1.12) shows an open structure with uniform morphological units. High resolution TEM (Figure 1.12, inset) shows graphitic planes along with an amorphous carbon phase. While EDS analysis confirmed the presence of Fe, Fe-based particles could not be observed in the TEM images, suggesting that iron particles are absent or that they are extremely small and homogeneously throughout the nitrogen-enriched carbon network.

Iron speciation in the representative Fe-CTS and Fe-AApyr catalysts is characterized with ^{57}Fe Mössbauer spectroscopy together with *in situ* x-ray absorption spectroscopy (XAS) (Figure 1.13). Two Fe species (D1 and D2) are identified in both Fe-AApyr and Fe-CTS catalysts resulting in two doublets (Figure 1a), which are assigned as a four-fold nitrogen coordination of Fe^{II} in low-spin (LS) and medium-spin state (MS), respectively.[24,25] Consistently, the solely FT-EXAFS peak around 1.5 Å (without phase-correction) is assigned to the Fe-N_4 moieties based on EXAFS fitting results. The D1 is subject of ongoing research related to the exact site structure and to the integration of FeN_4 moieties, which can be viewed either at defect sites within a graphene layer, or as a structure bridging two graphene zigzag-orarmchair-edges.[17,24] In addition to the two doublets (D1 and D2), three more Fe species were identified in the Fe-CTS catalyst resulting in a singlet, and two sextets (Figure 1.13), but not in the Fe-AApyr catalyst. The singlet is assigned to either γ-Fe or super paramagnetic Fe nanoparticles,[24] while the sextet's parameters match those of α-Fe and iron carbide.[24,25]

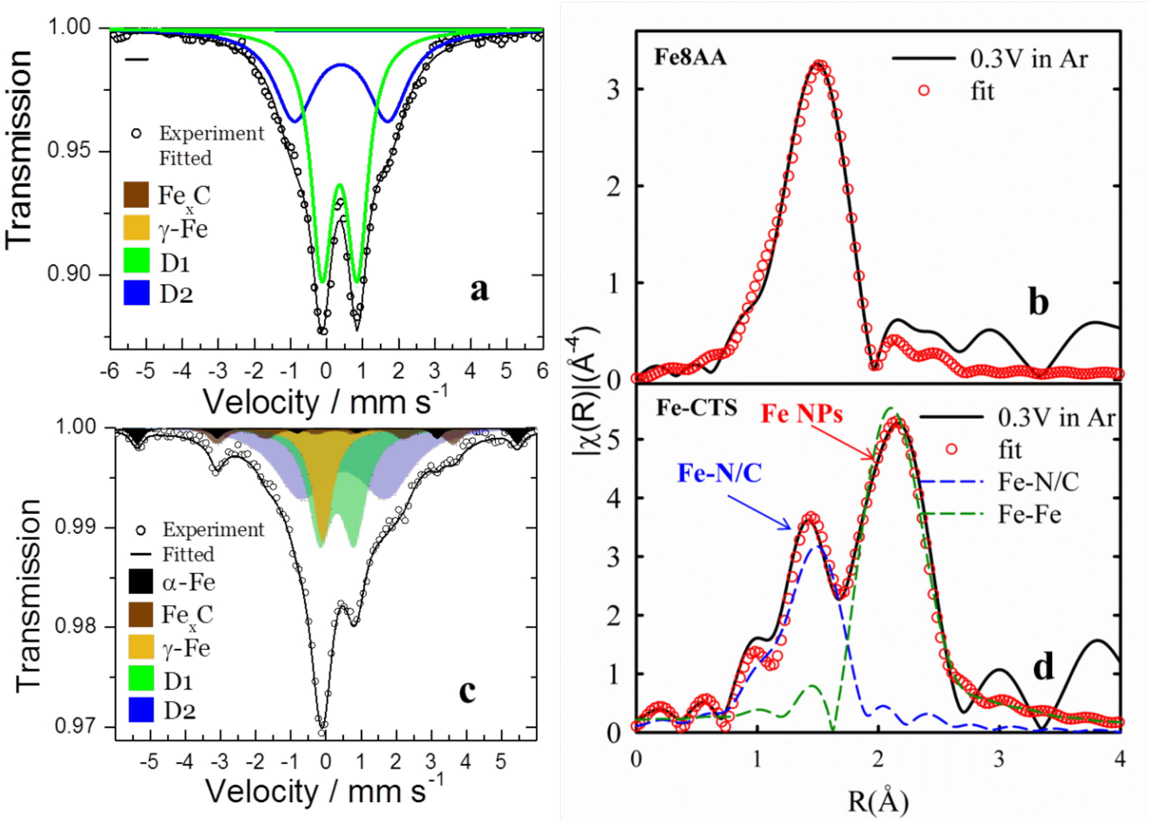

Figure 1.13. (left). Mössbauer absorption spectrum and its deconvolution for the Fe-AApyr and Fe-CTS catalysts. The measurement was performed at room temperature and calibrated vs. α-Fe foil. (Right). Fourier Transforms of the Fe K-edge XAS data and the corresponding EXAFS fits.

Table 1.2. Mössbauer fitted parameters for the Fe-CTS catalyst.

Component (assignment)	IS mm·s^{-1}	QS mm·s^{-1}	H Tesla	LW mm·s^{-1}	Relative absorption area %
Param. or γ-Fe	- 0.07	-	-	0.67	14
D1 ($Fe^{II}N_4$ LS)	0.33	0.98	-	0.80	30
D2 ($Fe^{II}N_4$ MS)	0.51	2.34	-	1.83	44
Fe_xC	0.29	-	20.2	0.62	10
α-Fe	0.04		33.5	0.37	4

The different content in the final products between these two catalysts revealed by *ex situ* Mössbauer spectroscopy is further confirmed by *in situ* XAS. The two FT peaks displayed in the left of Figure 1 clearly confirm the plurality of chemistries in the Fe-CTS catalyst. The second FT peak at ~ 2.1 Å (all the radial distances given in this work are without phase correction) can be well fitted as a Fe-Fe shell with a bond length of ~2.51 Å. This bond length is close to the Fe-Fe bond length in iron carbide (2.48 Å), confirming that the Fe-CTS catalyst contains some iron carbides that are stable under the acidic and oxidizing environment. The small $N_{Fe\text{-}Fe}$ (~1.2) suggests either the iron carbide content is low compared to the Fe-N_x species, and/or the particle size is small. This is consistent with the small amounts of γ-Fe and Fe_xC obtained by Mossbauer and absence of visible particles in high resolution TEM. The constant peak intensity with the operating potential indicates the iron carbide is not directly involved in the reaction.

Table 1.3: Results of fitting EXAFS data obtained under *in situ* electrochemical operating conditions for the Fe-CTS and Fe-AApyr catalysts synthesized at 900ºC and second heat treatment in NH_3 at 950 ºC. The measurements were performed at 0.3 and 0.9 V vs RHE in the N_2-saturated 0.1 M $HClO_4$ electrolyte at room temperature. Coordination number (N), phase-corrected bond length (R), Debye-Waller factor (σ^2), and edge shifts (E_0) are shown for each interaction.

Fe-CTS	Fe-C/N/O path				Fe-Fe path			
Potential	N	R (Å)	σ^2 (Å^2)×10^{-3}	E_0 (eV)	N	R (Å)	σ^2 (Å^2)×10^{-3}	E_0 (eV)
0.3 V	3.6(7)	2.02(2)	9(3)	-5(1)	1.2(3)	2.51(1)	9(3)	-5(1)
0.9 V	4.0(8)	2.01(2)	4(2)	-6(2)	1.3(3)	2.52(1)	4(2)	-6(2)
Fe-AApyr	Fe-C/N/O path				Fe-Fe path			
Potential	N	R (Å)	σ^2 (Å^2)×10^{-3}	E_0 (eV)	N	R (Å)	σ^2 (Å^2)×10^{-3}	E_0 (eV)
0.3 V	4.3(6)	2.05(2)	7(3)	-3(1)	-	-	-	-
0.9 V	5.2(8)	2.03(2)	5(2)	-2(2)	-	-	-	-

S_0^2 fixed at 0.88 as obtained by fitting the iron reference foil. The Fourier-transformed (FT) EXAFS data were fitted under simultaneous $k^{1,2,3}$ weighting, R range 1.0 - 3.0 Å, k range 1.95 - 10.96 Å^{-1}. The statistical errors of the least-squares fits were determined by ARTEMIS.

The first FT peak at ~1.6 Å arises from the Fe-N/Fe-C/Fe-O (nitrogen, carbon, and oxygen cannot be distinguished as surrounding atoms by XAS) scattering. Owing to the bulk average nature of EXAFS technique, the corresponding coordination number at 0.3 V (3.6) is a weighted average of the coordination number of the Fe-N bonds in the Fe-N_x species and the Fe-C bonds in the iron carbide. As the iron carbide content is relatively low, and the first shell Fe-C coordination number is small (≤ 3), it is reasonable to deduce that the Fe-N coordination number in the Fe-N_x species is 4. The increase in the coordination number as the potential is increased to 0.9 V suggests the adsorption of oxygenated species onto the Fe-N_4 sites. These hypotheses are further supported by the $\Delta\mu$ analysis shown below. Dislike Fe-CTS, Fe-AApyr contains only one FT peak locating around 1.6 Å, and the corresponding EXAFS fitting result of N is around 4. This indicates Fe-AApyr is dominated by Fe-N_4 moiety. The lack of the second FT peak shows that Fe-AApyr does not contain metallic Fe species under *in situ* operation conditions. Therefore, the combined characterization results show that by tuning the preparation parameters, we are able to have the control over the final product species by using the SSM methods.

Task 1.4 Development of Catalyst Structure Using Enzyme Mimics

First, two types of polymer-based catalysts with varying preparation parameters were synthesized from branched polyethyleneimine (50–100 kMW) and ferric chloride as nitrogen and metal source, respectively. Initially, 10 wt.% solution of the metal salt was added drop wise to 10 wt.% solution of the PEI while stirring. In case of the FePEI-1, the mixture was left stirring over 12 h (Fe-PEI-1) to allow full complexation, while the Fe-PEI-2 was stirred for 15 min, followed by evaporation of solvent in vacuum oven at 80 ◦C over period of 12 h. The metal-polymer network was then supported on high surface area carbon black (Ketjen Black 600 JD) at 1:1 complex to carbon ratio using dry impregnation method. The supported polymer-carbon hybrid materials were pyrolyzed at T = 850 ◦C in argon atmosphere. In order to increase ORR activity the second heat treatment was performed for both materials at the same conditions as a first pyrolysis: T = 850 ◦C in argon atmosphere.

Physical characterization Scanning electron microscopy was performed on a Hitachi S-800 instrument. XPS spectra were acquired on a Kratos Axis DLD Ultra X-ray photoelectron spectrometer using an Al K-source monochromatic operating at 150 W with no charge compensation. The base pressure was about 2×10^{-10} Torr, and operating pressure was around 2×10^{-9} Torr. Survey and high-resolution spectra were acquired at pass energies of 80 and 20 eV respectively. Acquisition time for survey spectra was 2 min, for C1s and O1s spectra −5 min, for N1s and Fe 2p −30 min. Data analysis and quantification were performed using CasaXPS software. A linear background subtraction was used for quantification of C1s, O1s and N1s spectra, while a Shirley background was applied to Fe 2p spectra. Sensitivity factors provided by the manufacturer were utilized. A 70% Gaussian/30% Lorentzian line shape was utilized in the curve-f it of N1s.

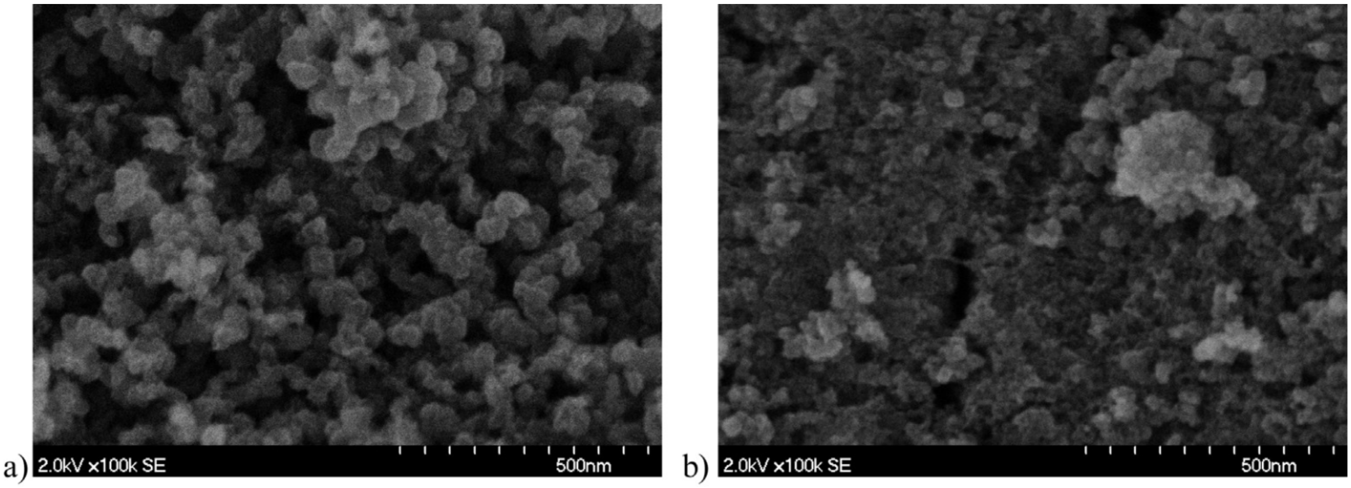

Figure. 1.14 SEM images for Fe-PEI-1 (a) and Fe-PEI-2 (b) catalysts.

It was observed by SEM that Fe-PEI-1 and Fe-PEI-2 have different morphology (Figure. 1.14). While Fe-PEI-1 has uniform and well dispersed particles, Fe-PEI-2 is substantially agglomerated. The surface area of the Fe-PEI-1 (estimated with 5 points Brunauer–Emmett–Teller method) was found to be more than two times higher compared to SA of Fe-PEI-2 (870 vs. 430 m^2/g, respectively). Such a difference in morphology and surface area can be explained by variations in synthesis due to differences in complexation efficiency through various rates of metal salt addition into the polymer, insufficient stirring and shorter reaction time in case of Fe-PEI-2. As a result, part the iron precursor was poorly dispersed, resulting in inhomogeneous distribution of polymer-carbon-iron material.XPS analysis revealed that materials mainly consist of carbon with several atomic percents of nitrogen and oxygen. Fe-PEI-1 sample has 1.6 % of N while Fe-PEI-2 has only 0.3 % of N.

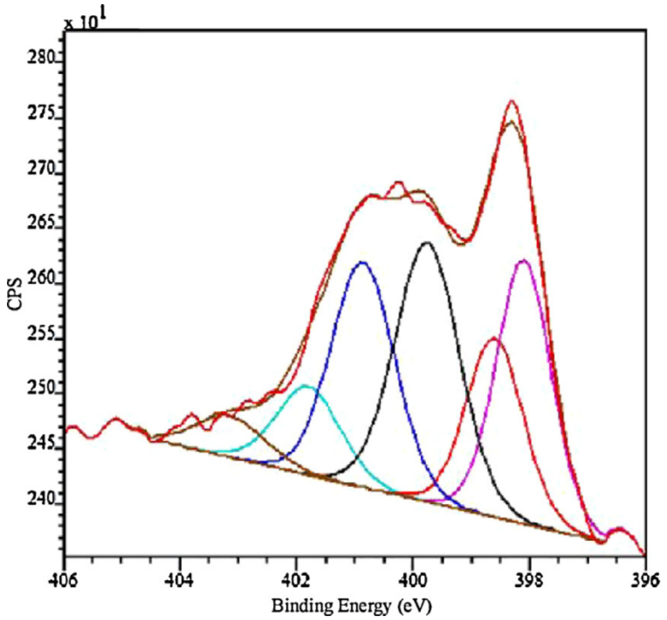

Figure 1.15 High resolution N1s spectra for (a) pyrolyzed Fe-PEI-2 (b) Fe-PEI-1 pyrolyzed in Ar atmosphere.

Figure. 1.15 shows N1s high resolution spectra representative of good and bad electrocatalysts. Six peaks of the same full width half maximum (FWHM), determined at the same acquisition setting for polypridine to be 1.2 eV, was used to curve fit N1s spectra. These six peaks correspond to six types of nitrogen, such as nitrile (398 eV), pyridinic (398.6 eV), N_x-Fe (399.6 eV), pyrrolic N (400.7 eV), quaternary (401.8 eV) and graphitic (403 eV)

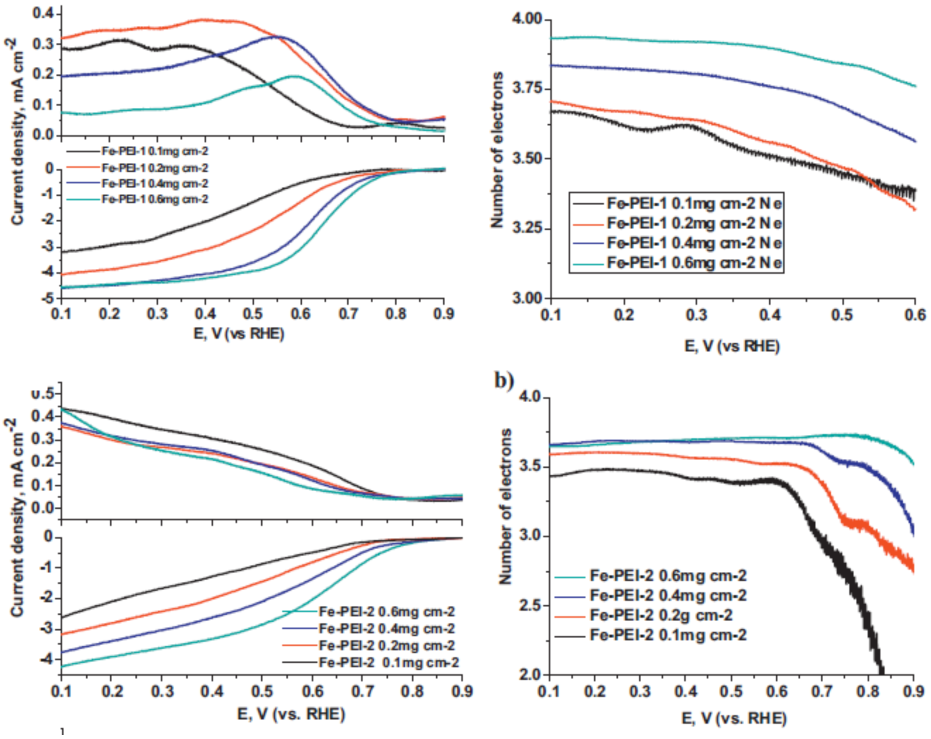

Figure. 1.16 Electrochemical data for Fe-PEI-1(top) and Fe-PEI-2 (bottom) catalysts with different loadings: (left) ORR performance, (right) number of electrons. Conditions: 0.5 M H_2SO_4 saturated with O_2, 1200 rpm, 5 mVs^{-1},

nitrogens. The Fe-PEI-1 and Fe-PEI-2 catalysts have obviously different distribution of N species Figure. 1.15. Relative amount of N_x-Fe centers is higher for Fe-PEI-1 compared to Fe-PEI-2 sample. The amount of pyrrolic N, which was shown to be responsible for the first 2e− step of O_2 to H_2O_2 reduction, in the Fe-PEI-2 sample is significantly larger than in Fe-PEI-1 sample.

Ring disk electrode testing. Electrochemical analysis for synthesized catalysts was performed using the Pine Instrument Company electrochemical analysis system. The rotational speeds were: 400, 900, 1200 and 1600 rpm, with a scan rate of 10 mV s^{-1}. The electrolytes were 0.5 M H_2SO_4 and 1 M KOH saturated in O_2 at room temperature. A platinum wire counter electrode, Ag/AgCl reference electrode in case of acidic media and Hg/HgO in case of alkaline media were used. Working electrodes were prepared by mixing 5 mg of the Fe-PEI electrocatalyst with 850 μL of isopropyl alcohol, and 150 μL of Nafion (0.5 wt.%, DuPont). The mixture was sonicated before 5, 10, 20 and 30 μL was applied onto a glassy carbon disk with a sectional area of 0.2474 cm^2. The loadings of catalyst on the electrode were: 0.1, 0.2, 04 and 0.6 mg cm^{-2}.

As for both catalysts, the ORR activity and number of electrons increase with increasing catalyst loading (Figure 1.16) in both acidic and alkaline electrolytes,[26] which points to indirect $2{\times}2e^-$ mechanisms for which two adjacent actives sites are required to complete the $2{\times}2e^-$ charge transfer. In addition, the Tafel slope of the Fe-PEI-2 catalyst in acid is different from other Tafel slopes. Detailed mechanistic studies revealed that Fe-PEI-2 catalyst has a different mechanism of oxygen reduction in acid compared to alkaline media, while Fe-PEI-1 has the same.[26] These mechanistic studies lead us to synthesize Fe-based catalysts containing both Fe-N_x and inorganic Fe species in order to efficiently promote deliver the $2{\times}2e^-$ reactions as shown below.

The PVAG-Fe catalysts was prepared by pyrolysis of the prior synthesized poly(vinylamine guanidine)−Fe complex (PVAG-Fe) supported on functionalized carbon black (Ketjen Black 600JD) precursor at 950 °C for 1 h in argon atmosphere. The PVAG polymer was synthesized following procedure previously employed by Bromberg *et al*. Briefly, the procedure follows three step syntheses. The first radical polymerization of N-vinylformamide to poly (N−vinylformamide) (PVF). The PVF is hydrolyzed to poly (N-vinylamine) (PVA)

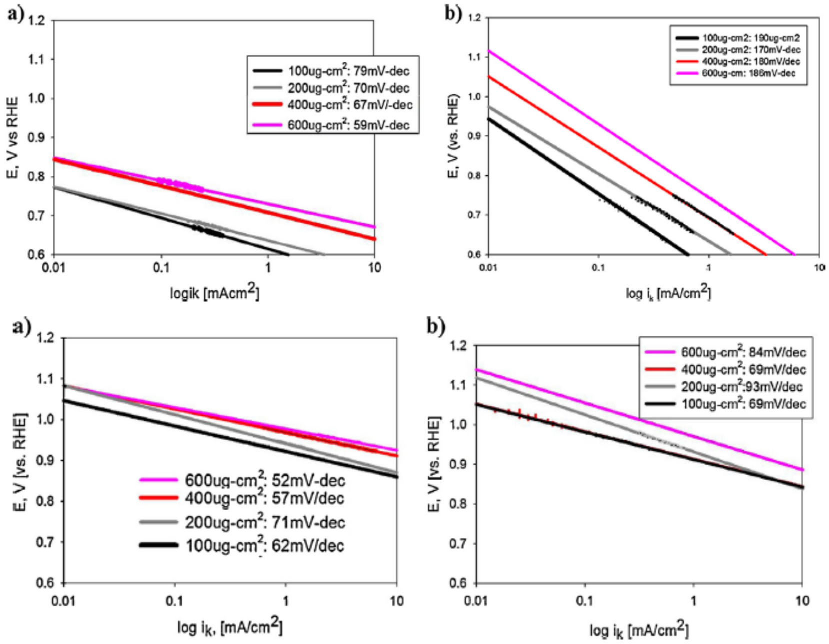

Figure. 1.17 Tafel plot for Fe-PEI-1(left) and Fe-PEI-2 (right) catalysts with different loadings: (top) acid, (bottomalkaline. Conditions: 1200 rpm, 5 mVs^{-1}, catalyst loading 0.6 mg cm^{-2}.

in the second step, and finally, the PVA is partially (~30−40% quanidized) to form poly (Nvinylamine quanidine) (PVAG). The separated and dried PVAG powder was dissolved in DI Millipore water, supported on functionalized carbon black, and then complexed with ferric chloride ($FeCl_3$) to form carbon-supported PVAG-Fe precursor.

Figure 1.18a,b show a comparative ORR activity analysis on several Fe−N_x−C catalysts mentioned above including the PVAG-Fe catalysts. This was accomplished using diverse precursors such as poly(N-vinylamine guanidine) (PVAG), poly(ethylene imine) (PEI), aminoantipyrine (AAPyr), and varied synthetic methodologies such as the reactive polymer approaches (Materials Preparation section) on standard carbon support and the sacrificial support method.[27] Despite the different synthesis procedures and precursors employed, each of these materials facilitate ORR at close range of onset potentials (~0.85−0.87 V vs RHE). The variations in diffusion-limited current densities are a result of differences in density, nature, and distribution of the available active centers in the high surface area microporous carbon scaffolds. The observation of similar Tafel slopes with values in the range of 56−63 mV/decade (Figure 18 inset) is suggestive of a common rate-limiting step involving one-electron transfer. However, such a rudimentary interpretation is predicated on fact that this data is derived from high loading of catalysts, hence relatively lower active site density in an otherwise thick electrode necessitating an in-depth fundamental understanding of the catalyst structure and reaction mechanisms using other complementary methodologies. Even though the presence of a redox behavior in similarly derived group of catalysts has been proposed earlier,[28] here we show using a combination of both electrochemical and element-specific spectroscopic results a clear correlation between the redox transition and onset of ORR.

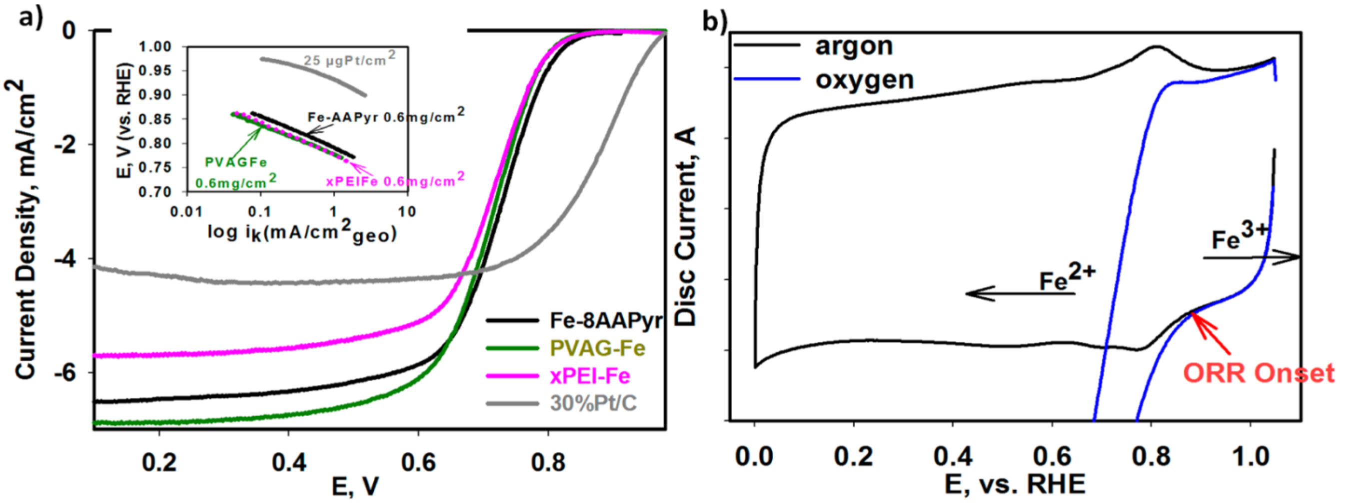

Figure 1.18. Electrochemical study of Fe-AAPyr, PVAG-Fe, and Fe-PEI compared to BASF-ETEK 30% Pt/C in 0.1 M $HClO_4$. (a) ORR polarization curves, with Tafel slopes in the inset, collected at 1600 rpm. (b) A typical for Fe−NC catalysts CV in O_2-free (black) electrolyte with the clear Fe$^{2+/3+}$ redox transition between 0.7 and 0.9 V and corresponding ORR polarization curve (blue) collected with PVAG-Fe catalyst. Scan rate: 20 mV/s. Loading of FeNC catalysts: 0.6 mg/cm2 on 5.61 mm glassy carbon disk electrode. Loading of Pt/C: catalyst 25 µg$_{Pt}$/cm^2.

Development of MOF-based non-PGM catalysts

Besides the polymer-based non-PGM catalysts introduced above, an iron-based non-PGM ORR electrocatalyst is developed that utilizes a MOF as the source for embedding Fe-based sites. In order to achieve this, a MOF based on Zn (ZIF-8) is used as an encapsulator for Fe-chelated with a nitrogen complex. The MOF support was chosen in order to take advantage of the porosity and high surface area, which are features known to improve the catalytic activity. Also, encapsulation of the chelated iron complex in the pores was employed in an effort to obtain equal distribution and high density of active sites. ORR was investigated in alkaline and acidic media to better understand the reduction mechanism of the studied electrocatalyst. The synthetic approach featuring chemical encapsulation is an important distinction to another reported approach with the same MOF structure that used ball milling for extended periods. The derived catalyst in this work is referred to as "FePhen@MOF". The corresponding MOF procured commercially (BASF) has a trade name of "Basolite®". MOF based structures with and without incorporation of iron precursor were heat treated and etched to form the active electrocatalyst, hereby referred to as "FePhen@MOF-ArNH$_3$" and "Basolite®-ArNH$_3$" respectively. The most critical advantage however was that this approach enabled proper comparison with samples derived wherein no Fe was chelated, everything else remaining the same. This is in contrast to previous reports where a complete absence of Fe cannot be claimed.[29] By combining electrochemical and spectroscopic methods we are able to show that while the derived Fe containing non-PGM catalysts exhibits one of the best-reported ORR activities, coordination environment for Fe is predominantly Fe/Fe$_x$C particulate in nature. Because of the unusual activity and structure, detailed characterization and mechanistic studies were performed on this particular sample, in comparison to previous polymer-based or macrocycled-based samples, to elucidate the structure and kinetics related to the newly found active sites. Using *in situ* X-ray absorption spectroscopy (XAS) we are able to characterize the iron coordination of the electrocatalyst (FePhen@MOF-ArNH$_3$) under actual simulated operating conditions of a PEM fuel cell and are unable to detect any direct Fe-N$_x$ coordinated sites present in the non-PGM electrocatalyst. To our knowledge this is the first definitive report of a non-PGM electrocatalyst without the presence of Fe-N$_x$ sites exhibiting one of the highest reported activities for ORR in acidic media. The electrochemical performance (both RRDE and PEM fuel cell polarization) is correlated with active site function determined using *in situ* synchrotron XAS and aided by *ex situ* physicochemical methods such as X-ray diffraction (XRD) and high-resolution transmission electron microscopy (HR-TEM). In addition to the absence of direct Fe-N$_x$ coordination, we also show the complete absence of any direct involvement of the Fe in the electrocatalytic pathway as a result of its presence subsurface to the carbo-nitrided fibers and hence its important implication in avoidance of any Fenton type process related to onset of peroxide induced free radical formation as detailed earlier.[30]

Catalyst Synthesis and Electrochemical Measurements

The commercial Pt/C (46%) electrocatalyst used as a standard in this study is obtained from Tanaka Kikinzoku International KK (Japan). For the synthesis of FePhen@MOF 2-methylimidazole (5.90g, 0.072mol, 160eq) was dissolved in methanol (20mL) at room temperature with stirring in flask A. In flask B, zinc(II) nitrate χ-hydrate (10.80g, 0.036mol, 80eq) and 1,10-phenanthroline monohydrate (12.96g, 0.072mol, 160eq) were dissolved in methanol (30mL) and water (45mL) at room temperature with stirring. Once both flasks' contents were fully dissolved, flask B was added to flask A. Iron(II) acetate (0.081g, 4.66E-4mol, 1eq) was added to the reaction, and this was stirred at room temperature for 24h. A second reaction identical to the aforementioned vessel was assembled, and the two separate reactions progressed in tandem. Before addition of iron(II) acetate, the reaction began to turn slightly milky white/turbid in appearance. This intensified over the course of the reaction, resulting in a fine suspension turbid and pale orange in color. The two reaction vessels were then combined in 6x50mL centrifuge tubes and centrifuged at 4000 rpm for 25min, washed 3 times with methanol (6x40mL each time), centrifuging at 3700 rpm for 17 minutes in between each washing. The resulting orange/white solid was dried in a vacuum oven for 6-12 hours at 60-70°C and afforded formation of the desired FePhen@MOF, a light tan powder (typically 4.5-5.5g total yield from the two combined reaction vessels). The dried powder was then subjected to either one or two heat-treatments, i.e., in argon at 1050 °C with a 1 hour dwell time (FePhen@MOF-Ar) and ammonia at 1050 °C with an 18 minute dwell time (FePhen@MOF-ArNH$_3$) respectively. The weight percent of Fe used in the synthesis of FePhen@MOF and its retention throughout the heat treatment process (FePhen@MOF-Ar and FePhen@MOF-ArNH$_3$) was quantified using ICP-MS and is listed

SAMPLE	%Fe	%Zn
FePhen@MOF	0.65	21.85
FePhen@MOF-Ar	2.5	0.56
FePhen@MOF-ArNH$_3$	3.1	0.13
Basolite	-	25

Table 1.4: Elemental composition. Quantification of Fe and Zn in non-PGM materials based on ICP-MS measurements (0.012 gm/L limit of detection).

Perchloric acid electrolyte (0.1 M) was prepared using double-distilled 70% perchloric acid (GFS Chemicals) and potassium hydroxide electrolyte (0.1 M) was prepared using pellets (Alfa Aesar). Electrochemical measurements were carried out on glassy carbon (GC) disk (5.61 mm diameter, Pine Instruments) that was polished with 0.05-micron alumina paste (Buehler, Lake Bluff, IL) and then sonicated in distilled water and Isopropyl alcohol. Catalysts inks were prepared by dispersing the catalyst in a volume of 1:1 Millipore water:isopropyl alcohol with 10 vol% of 5 wt% Nafion® as a binder. The ink solution was then sonicated approximately 60 minutes to get a uniform suspension. A small volume of the catalyst ink was deposited on the GC substrate to obtain a platinum metal loading of 15 μg/cm^2 and a non-PGM loading of approximately 600 μg/cm^2. All electrochemical measurements were carried out at room temperature (20-25 °C) in a standard electrochemical cell (Chemglass) with an acid or base electrolyte using a rotating disk electrode (RDE) setup from Pine Instrument Company connected to an Autolab bipotentiostat (PGSTAT302N). Cyclic voltammetry was run on both Pt and non-Pt catalysts in 0.1 M perchloric acid ($HClO_4$) and 0.1M potassium hydroxide (KOH) bubbled with argon. ORR was investigated by the RDE technique after bubbling oxygen in the electrolyte solution followed with rotations at 100, 400, 900, 1600 and 2500 rpm. Scans were recorded at 20 mV/s and all potentials are referenced to a reversible hydrogen electrode (RHE) scale made from the same solution as the electrolyte. Carbon corrosion treatment of FePhen@MOF-ArNH$_3$ was performed in argon saturated 0.1M $HClO_4$ by cycling 1-1.5 V vs RHE at 100 mV/s and 1600 rpm rotation speed for 7,500 cycles.

Membrane electrode assemblies (MEAs) for fuel cell testing were prepared using FePhen@MOF-ArNH$_3$ cathode on Gas Diffusion Layer (Sigracet BC25 GDL), Pt/C (Tanaka, 46%) anodes on GDL (Sigracet BC25), Nafion 5wt% ionomer solution, and Nafion 211 ionomer membrane. To prepare the cathode, a catalyst ink composed of FePhen@MOF-ArNH$_3$ dispersed in a water-alcohol mixture with the requisite amount of ionomer (Nafion 5wt%) was sprayed on gas diffusion layer (Sigracet, BC25). Typical cathode loading consisted of 0.2 mg/cm^2 with an ionomer content of 60% by weight of the catalyst. After drying the cathodes, a layer of interfacial ionomer was sprayed to achieve a loading of 0.4mg$_{\text{Nafion}}$/cm^2. Anodes were prepared with commercial Pt/C (Tanka, 46%) in the same manner as the cathode. Electrodes for the Pt- based cathode MEA were supplied by industry. Hot pressing of the electrodes together with a Nafion 211 membrane was carried out at 130 °C and 1,000 lbs. for duration of 5 minutes. MEAs were then assembled in a fuel cell consisting of 5 cm^2 serpentine flow fields. Humidification of the MEA was performed for 60 minutes by flowing N_2 (100% RH) at a cell temperature of 80 °C. The operating temperature of the fuel cell was 80 °C and the cell was activated with H_2/O_2 (inlet temperatures 85 °C, 100% RH, 22 psi back pressure). Durability cycling followed protocols from Nissan Technical Center North America (NTCNA) designed to simulate accelerated drive cycle conditions based on transitions between open circuit voltage and idling in automobile operation. Durability was tested at 80 °C with N_2 flowing on the cathode while stepping potential from 0.6 to 1.0 V vs. RHE with 3s hold at each potential step.

Physicochemical Characterization

X-ray diffraction was performed on a Rigaku (model Ultima-IV) diffractometer with Cu Kα radiation (λ=1.5418 Å) at 40 kV and 40 mA. The scan speed was 2-20 seconds and the step size was 0.1°. N_2 sorption analysis was performed on a Quantachrome NOVA 2200e at 77 K. Total surface area was determined by the

Brunauer-Emmett-Teller (BET) method and pore size distribution was determined using Non-Local Density Functional Theory (NLDFT) split pore method from the NovaWin software. Thermogravimetric analyses (TGA) were performed on TA Instruments SDT Analyzer Q600 from 22-1100°C with a ramp rate of 5°C/min and dwelling for 5min at maximum temperature. All studies were conducted under argon atmosphere, with a flow rate of 100mL/min. UV-Vis quantification performed on Thermo-Fisher UV-Vis spectrophotometer collecting absorbance spectra from 190-700 nm. Calibration curve generated from 12.5-100.0 μM 1,10-phenanthroline monohydrate dissolved in 1 M HCl. 300 μM solutions of FePhen@MOF and Basolite Z1200© standard dissolved in 1 M HCl were run under the same conditions. Scanning electron microscopy was performed on a Hitachi S-4900 FSEM instrument with an accelerating voltage of 3-5 keV with samples mounted on a carbon adhesive stub attached to an aluminum sample stage. High-resolution transmission electron microscopy images were taken on a JEOL 2010 field emission gun (FEG) TEM at 200 kV with samples deposited on a holey carbon film on a 300 mesh copper grid.

^{57}Fe Mössbauer spectroscopy was measured with a ^{57}Co source embedded in rhodium matrix. The measurement was performed keeping the source and absorber at room temperature. The spectrometer was operated with a triangular velocity waveform, and a gas filled proportional counter was used for the detection of the γ-rays. Velocity calibration was performed with an α-Fe foil. The spectra were fitted with a combination of Lorentzian lines. In this way, spectral parameters such as the isomer shift (IS), the electric quadrupole splitting (QS), the linewidth at half maximum (LW), the hyperfine fields (H) and the absorption spectral areas of the various spectral components were determined. No constraints were applied to the fitting parameters except on the IS of the singlet assigned to γ-Fe, fixed at -0.08 mm s^{-1} on the basis of previous experimental studies on Fe-N-C catalysts showing the presence of the ubiquitous singlet assigned to γ-Fe.

The *in situ* XAS studies at the Fe K-edge (7112 eV) were performed at X3B beamline of National Synchrotron Light Source (NSLS, Brookhaven National Laboratory, NY). The detailed information of the experiments and data analysis has been provided above.

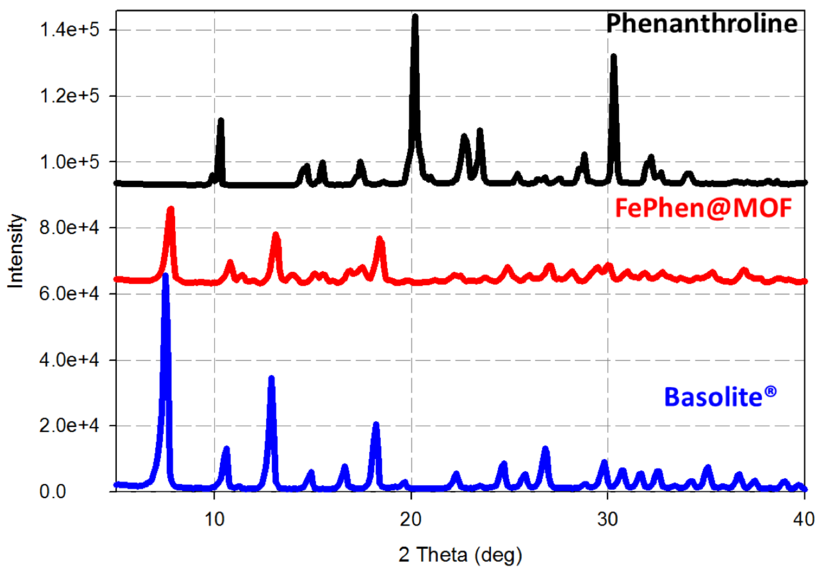

Figure 1.19: XRD. Powder pattern comparison of non-heat treated Basolite Z1200©, FePhen@MOF and 1, 10-phenanthroline to confirm formation of MOF structure with encapsulation synthesis of FePhen@MOF and absence of crystalline 1,10-phenanthroline.

The 2θ values and symmetry of the powder XRD of FePhen@MOF (prior to heat treatment) as compared with the as purchased Basolite® (Sigma, Basolite Z1200) confirm the formation of the crystalline MOF structure (Figure. 1.19).

The concomitant diminished intensity of the signal from FePhen@MOF (Figure. 1.20, inset) is indicative of the presence of guest molecules within the MOF structure as a result of encapsulation, this is in agreement with similar observations reported earlier. In addition the absence of the diffraction lines characteristic of 1,10-phenanthroline (Figure. 1.19) (N-chelating agent for Fe) imply that it is not present as a separate entity in crystalline form.

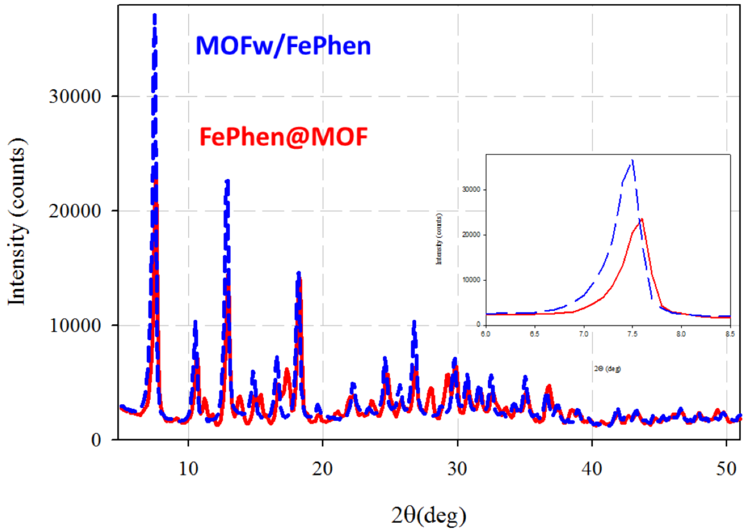

Figure 1.20: XRD. Powder pattern comparison of two samples: ZIF-8 MOF mixed with FePhen complex (MOFw/FePhen) and FePhen@MOF from encapsulation synthesis. First peak of FePhen@MOF compared to MOFw/FePhen (inset) shows diminished intensity and positive shift due to encapsulation.

However, ultraviolet-visible (UV-Vis) spectroscopy (Table 1.4) confirmed retention of 1,10-phenanthroline in the FePhen@MOF and thermogravimetric analysis (TGA) indicated its enhanced thermal stability as a result of the encapsulation (Figure. 1.21).

Further, FePhen@MOF exhibited a much smaller Brunauer-Emmet-Teller (BET) (Figure. 1.22) surface area than the commercial ananlogous Basolite® (424 m^2/g vs. 1813 m^2/g) which is likely attributable to the encapsulation of the chelated iron complex within the MOF-pore reducing the overall pore volume (Figure. 1.19).

The FePhen@MOF material was subjected to an initial heat treatment (1050 °C) in Ar atmosphere (FePhen@MOF-Ar) for a tailored breakdown of the MOF structure and removal of Zn nodes via sublimation resulting in an initial rendering of a carbonaceous material with significant electronic conductivity. The XRD powder pattern (Figure. 1.24 a) shows emergence of an elevated baseline typical for presence of amorphous material as well as diffraction lines of graphite and several iron phases (Figure. 1.24 b) (iron-Fe (Im-3m) and iron carbide-Fe_5C_2 (C2/c)). We were not able to accurately determine the exact stoichiometry of the iron carbide and believe we have mixture (Fe_xC).

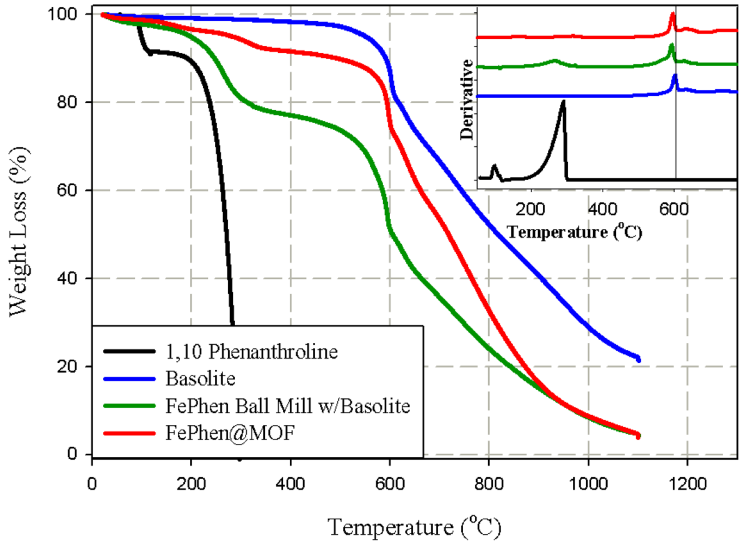

Figure 1.21. Thermogravimetric analysis of 1,10 Phenanthroline precursor, Basolite Z1200©, FePhen precurors mixed with Basolite Z1200© (MOFw/FePhen), and non-heat treated FePhen@MOF. Thermal stability of 1,10-phenanthroline in enhanced due to encapsulation in FePhen@MOF. All measurements were run under argon with 100 mL/min flow rate.

An additional heat treatment (900 °C) in ammonia (FePhen@MOF-$ArNH_3$) led to the formation of several new diffraction lines (Figure. 1.24) that indicate the incorporation of nitrogen into the carbon scaffold in the vicinity of the iron. These new diffraction lines post NH_3 heat treatment show emergence of Fe-nitrides ($Fe_3N_{1.59}$ (P6322) and Fe_2N (P-31m(162))), however XRD alone could not unambiguously determine the exact nitrogen content. Comparing these XRD results with those obtained from Basolite®-$ArNH_3$ (subjected to the same heat treatments as FePhen@MOF-$ArNH_3$) lead us to believe that in the latter case the iron is converted to its metallic form during the initial argon heat treatment and subsequently acts as a catalyst that graphitizes the vicinal carbon-nitrogen's from MOF precursor. The second heat treatment in ammonia thus is effective in etching a portion of the remaining amorphous carbon and introducing nitrogen functionalities into the carbon scaffold.

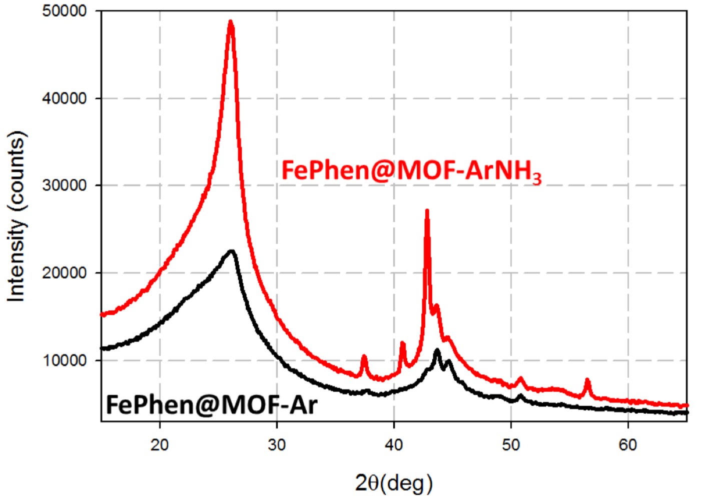

Figure 1.23: XRD. Powder pattern comparison of effect of heat treatment of FePhen@MOF in argon alone or argon followed by ammonia. Subsequent heat treatment in ammonia shows emergence iron nitride diffraction lines indicating incorporation of nitrogen functionalities.

encapsulation of FePhen in the pores.

The BET surface area increased with each heat-treatment (Figure. 1.25) resulting in FePhen@MOF-ArNH$_3$ exhibiting a surface area of 1200 m^2/g, comparable to that of the original Basolite® (no heat treatment). Basolite® and FePhen@MOF are originally microporous (<20 Å) materials, however the microporosity is increased with each heat-treatment and mesopores (20-40 Å) are introduced (Figure. 1.25) to FePhen@MOF-ArNH$_3$.

X-ray absorption spectroscopy (XAS) was used to further probe the local coordination of the iron present after heat treatment. Fourier transform (FT) of the extended X-ray absorption fine structure spectra (EXAFS) of the Fe K-edge (Figure. 1.26) measured on the electrode *in situ* (held at 0.3 V, free of adsorbates) was dominated by a peak at ~2.2 Å, which corresponds well with the known Fe-Fe bond length in bulk iron (2.49 Å) and/or iron carbide (2.48 Å).

	γ-Fe	α-Fe	Doublet	Fe$_3$C
IS$^{(1)}$ / mm s^{-1}	- 0.08$^{(2)}$	- 0.03	0.16	0.19
QS / mm s^{-1}	0.00	0.00	0.50	0.00
LW / mm s^{-1}	0.29	0.40	0.54	0.42
HF / Tesla	0.00	33.2	0.00	20.7
% Area	13	6	45	36

Table 1.5: Table of fitted Mössbauer parameters for the catalyst FePhen@MOF-ArNH$_3$. Fitted spectral parameters for the four components used to fit the ^{57}Fe Mössbauer spectrum of FePhen@MOF-Ar-NH$_3$. The isomer shift (IS), quadrupole splitting (QS), linewidth, (LW) and hyperfine field (HF) are given as well as the relative absorption area corresponding to each component (% Area).

(1) Relative to a calibration performed with an α-Fe foil.

(2) Fixed spectral parameter, on the basis of previous studies on Fe-N-C catalysts.

The qualitative comparison of the FePhen@MOF-ArNH$_3$ spectrum with the spectra of the standard metallic iron foil (Fe foil) and a Fe$_3$C standard (Figure. 1.27) suggests that the iron is predominantly converted to its metallic state with a minor carbide phase. However it should be noted that an inherent limitation of XAS is the inability to differentiate between C, N and O neighbors. Visual examination of the EXAFS data cannot rule out the presence of small amount of Fe-N$_x$ species by itself, especially considering the normal uncertainties of EXAFS fits (usually <1 for coordination number). In this work EXAFS is only used as additional evidence of the absence of Fe-N_x species. Therefore we cannot use FT EXAFS to conclusively identify the presence or absence of Fe nitrides or carbides in the final catalyst.

In order to further investigate the different iron coordination environments in FePhen@MOF-ArNH_3 and to unambiguously confirm the absence of FeN_xC_y moieties, the sample was examined with *ex situ* ^{57}Fe Mössbauer spectroscopy (Figure. 1.28). The absorption spectrum measured at room-temperature (RT) was fitted with four components and their parameters are reported in Table 1.2.

The singlet with an isomer shift (IS) of - 0.08 mm s^{-1} is ubiquitous in pyrolyzed Fe-N-C catalysts and assigned to paramagnetic γ-Fe.[31] While α-Fe nanoparticles could also result at RT in a singlet with similar parameters, it would turn into a sextet at 5 K due to a super-paramagnetic transition. The Mössbauer spectrum of FePhen@MOF-ArNH_3 measured at 5 K (not shown) still showed the singlet, thereby foreboding its assignment to α-Fe nanoparticles. Next, the most intense sextet in Figure. 1.28 with a IS of 0.19 mm s^{-1} and a hyperfine field (HF) of 20.7 T corresponds to ferromagnetic Fe_3C.[32] The minor sextet with an IS-value close to zero and a larger hyperfine field of 33.2 T is unambiguously assigned to ferromagnetic α-Fe. The last component is a doublet with an IS of 0.16 mm s^{-1} and a quadrupole splitting (QS) of 0.50 mm s^{-1}. It may not be assigned to iron-rich nitrides such as ε-Fe_3N and γ'-Fe_4N, but can be assigned to either paramagnetic amorphous iron carbide, Fe_xC[33] or nitrogen-rich iron nitrides.[34] On the basis of the experimental X-ray diffraction pattern (Figure. 1.24) and doublet's Mössbauer parameters (especially QS), the doublet is assigned to ξ-Fe_2N or ε-$Fe_{2+x}N$ with x = 0.1, featuring an interstitial binary nitride with Fe atoms defining a hexagonal close-packed structure. Its presence after a pyrolysis at 1050°C in pure NH_3 is in agreement with the Fe-N phase diagram and actually expected since the pyrolysis conditions are typically those employed for producing Fe_2N.[35]

Thus, the analysis of the Mössbauer spectrum of FePhen@MOF-ArNH_3 demonstrates the absence of the doublets D1 and D2 that had been identified in all Fe-N-C catalysts investigated with Mössbauer spectroscopy thus far. D1 and D2 have been assigned to FeN_xC_y moieties covalently integrated in graphene sheets, with the ferrous ion in low- and medium-spin state, respectively.[36] Their Mössbauer spectral parameters resemble those of Fe(II)-phthalocyanine adsorbed on carbon (D1) and crystalline iron phthalocyanine (D2). The IS and QS values of D1 typically range from 0.26-0.39 mm s^{-1} and 0.90-1.16 mm s^{-1}, respectively.[37] For D2, the typical range of IS and QS values are 0.36-0.37 mm s^{-1} and 2.40-2.65 mm s^{-1}, respectively. The doublet D observed here with IS and QS values of 0.16 and 0.50 mm s^{-1} is fundamentally different and cannot be assigned to any FeN_xC_y moiety integrated in a graphene sheet. Thus, the doublet D observed in the present work can be confidently and entirely assigned to a nitrogen-rich iron nitride crystalline structure. Hence, it is concluded that FeN_xC_y moieties integrated in graphene sheets are absent in the sample FePhen@MOF-ArNH_3.

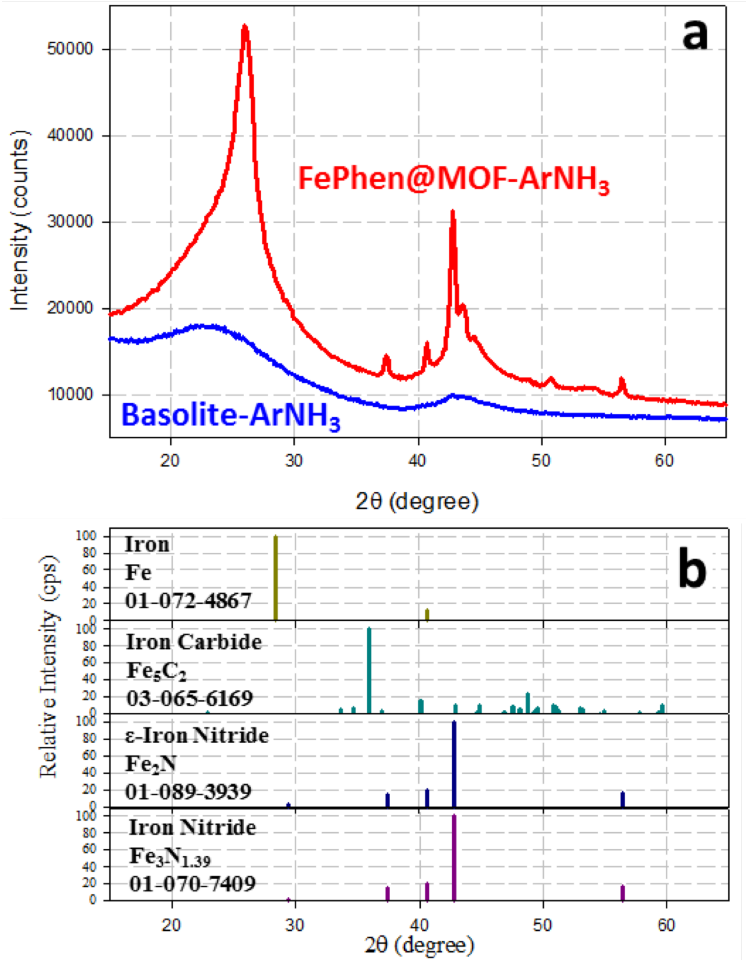

Figure 1.24: Physicochemical Characterization. (a) X-ray diffraction pattern of FePhen@MOF-ArNH$_3$ and iron-free Basolite-ArNH$_3$. (b) diffraction patterns of iron, iron carbide, and iron nitride.

The surface morphology of FePhen@MOF-ArNH$_3$ (Figure 1.29 b) was probed with scanning electron microscopy (SEM) and revealed that the heat treatment produces a heterogeneous material that is comprised of several different carbon morphologies. The MOF framework decomposed during the heat treatment forming a porous carbon framework. Additionally, some of the Fe agglomerated into Fe NPs that catalyzed the growth of Carbon nanotubes (CNTs) of varying sizes and possessed distinct bamboo-like joints, which are characteristic of N-doped carbon.[38] High-resolution transmission electron microscopy (HR-TEM) revealed that Fe/Fe$_3$C particles were contained within the compartments of the CNTs (Figure 1.29 c and d) and the compartment wall thickness varied with the size of the Fe/Fe$_3$C particles. Conversely, the surface morphology of Basolite®-ArNH$_3$ (Figure 1.29 a) had no CNTs present, which suggests the iron present in FePhen@MOF primarily acts as a catalyst for the graphitization of carbon.

Electrochemical Performance

Basolite® (Basolite-ArNH$_3$) was subjected to the same heat treatment as FePhen@MOF-ArNH$_3$ (i.e., Ar followed with NH$_3$ at 1050 and 1050 °C respectively) to be used as a reference for an iron-free catalyst in our RRDE studies. Typically, Pt/C is known to proceed predominantly through the 4 e$^-$ path in both alkaline and acidic media, as long as the surface is free of poisonous adsorbates.[16]

However, in alkaline media it has been shown that specifically adsorbed hydroxyl species non-covalently interact with solvated oxygen molecules and the reduction proceeds through a 2e$^-$ outer sphere charge transfer process producing the peroxide anion intermediate (HO$_2^-$), (as detected at the ring electrode of RRDE at ~0.8 V[17] (Figure 1.30)) followed with an additional concerted 2e$^-$ reduction step to water. The same report showed that in contrast to this a non-PGM catalyst derived from heat treated Fe-tetraphenylporphyrin (Fe-TPP)[17] exhibits an exclusive inner sphere concerted 4e$^-$ reduction in alkaline media due to direct adsorption of O$_2$ and the kinetically favored hydrogen peroxide reduction reaction (HPRR).[17] Central to this mechanism was its correlation with Fe-N$_x$ (predominant four coordination) active sites formed in the divacant defects in the carbon basal plane.[17]

In alkaline media Basolite®-ArNH$_3$ has an onset potential of 0.97 V (Figure 1.30) and the oxidation of the peroxide intermediate detected at the ring electrode coincides with the onset of reduction at the disk (Figure 1.30). This indicates that the peroxide is not stabilized on the active-site and ORR proceeds predominantly

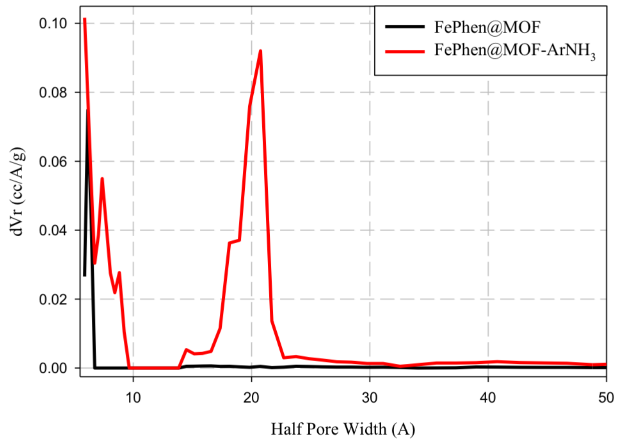

Figure 1.25: Pore sized distribution of non-heat treated FePhen@MOF compared to FePhen@MOF-ArNH$_3$, determined from NLDFT model of nitrogen adsorption data. Heat treatment introduces mesopores (20-40 Å) and new micropores (<20 Å).

through a 2e$^-$ reduction pathway. However, the presence of the iron in FePhen@MOF-ArNH$_3$ provides a 60mV improvement (w.r.to Basolite®-ArNH$_3$) in the onset potential (1.03 V vs. 0.97 V) as well as a 40 mV improvement in half-wave potential ($E_{½}$) (0.86 V vs 0.82 V) (Figure 1.31). In addition, the onset of the peroxide oxidation peak at the ring electrode is shifted cathodically to ~0.45 V (Figure 1.30). Peroxide oxidation at 0.45 V is also observed on Pt/C electrocatalyst (Figure 1.30) and has been attributed to 2e$^-$ reduction of oxygen by the quinone functionalities of the carbon support.[17]

However, FePhen@MOF-ArNH$_3$ did not demonstrate enhanced HPRR activity (Figure 1.32) and therefore this increase in activity cannot be attributed to peroxide specific Fe-N$_x$ sites. These electrochemical results suggest incorporation of iron moieties in FePhen@MOF-ArNH$_3$ in a different coordination environment as compared to classical Fe-N$_x$ active site based electrocatalyst (as exemplified by Fe-TPP). Considering the XRD, SEM and TEM results presented above, it can be conjectured that Fe is present in the form Fe/Fe$_3$C, sub-surface to the N-doped carbon overlayer. As shown later in this chapter based on *in situ* element specific XAS spectroscopy results, subsurface Fe/Fe$_3$C are inactive towards O$_2$ adsorption, and the ORR activity predominantly appears to arise from the N-doped carbon surface. It appears the presence of the subsurface Fe/Fe$_3$C acts to stabilize the peroxide intermediate on the active-site in the alkaline medium.

When the same experiment was conducted in acidic media FePhen@MOF-ArNH$_3$ exhibited a 90 mV improvement in $E_{½}$ (0.77 V vs 0.68 V) for ORR when compared with Basolite®-ArNH$_3$ (Figure 1.31). This is evidenced by the higher onset potential (E=0.93 V vs. E=0.89 V) of FePhen@MOF-ArNH$_3$ vs. Basolite®-ArNH$_3$ in oxygen saturated 0.1M HClO$_4$. More interestingly, the onset of peroxide oxidation for both of the non-PGM electrocatalyst in acidic media now coincides with the onset of ORR (Figure 1.33).

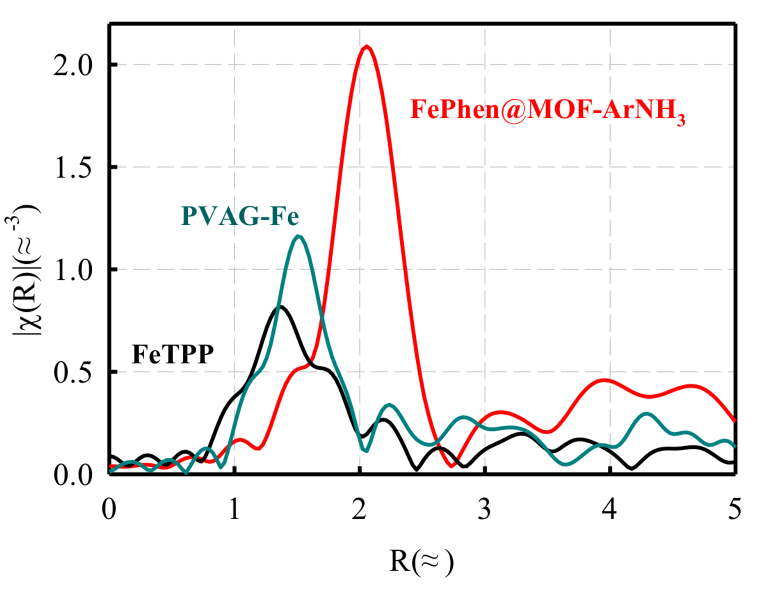

Figure 1.26. FePhen@MOF-ArNH$_3$, FeTPP pyrolyzed at 800 °C and PVAG-Fe in N$_2$ saturated 0.1M HClO$_4$.

When switching to the low pH environment the peroxide intermediate is no longer present as anion, but as a neutral species (H_2O_2) that has been shown to desorb more easily into the bulk electrolyte due to the absence of intermediate stabilization on the active site[17]. Our results confirm this finding, but we also find that the oxidative ring current of Basolite®-ArNH$_3$ is an order of magnitude higher than FePhen@MOF-ArNH$_3$. This suggests that the presence of the iron moieties in FePhen@MOF-ArNH$_3$ still promotes the selectivity toward the 4e$^-$ ORR pathway in acidic media. As mentioned above in our discussions on alkaline media results, sub-surface Fe appears to be critical in the electrocatalysis in close concert with

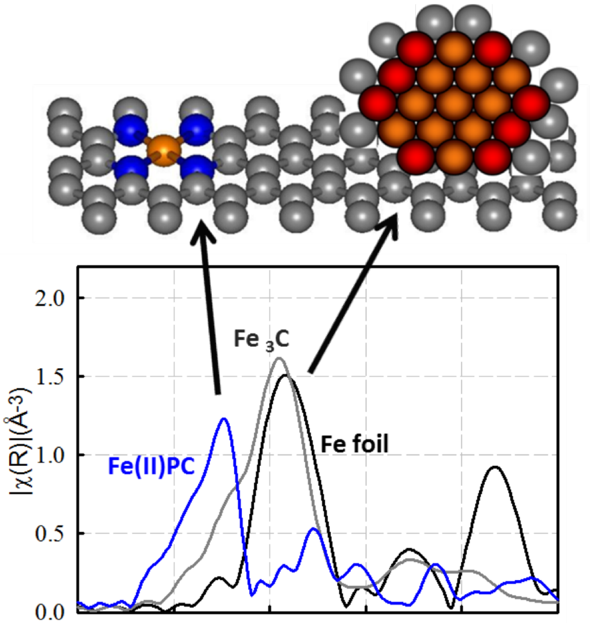

Figure 1.27: Fourier Transform EXAFS. Fe(II)Pc, Fe_3C and Fe foil standards collected at Fe K-edge (7112 eV).

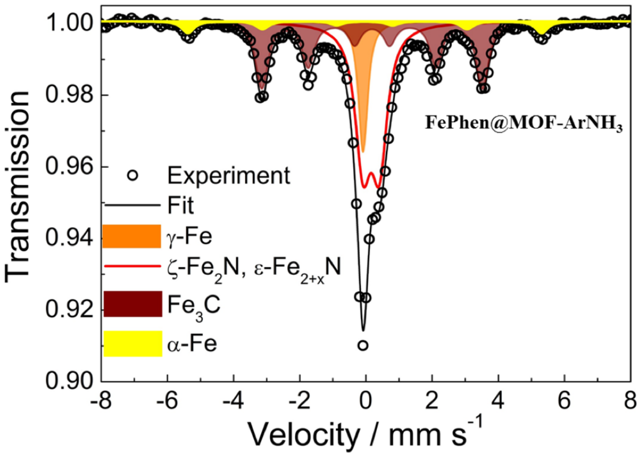

Figure 1.28: ^{57}Fe Mössbauer spectrum of FePhen@MOF-ArNH_3.

synergistic effect of N-doped carbon (Figure 1.29 c and d). This hypothesis is supported by the DFT calculations from Deng *et al.*,[39] in which the electronic properties of the carbon are enhanced by the interaction with nitrogen and Fe enabling easier adsorption of O_2 and reduction to H_2O.

The inherent ORR activity exhibited by RRDE measurements of FePhen@MOF-ArNH_3 in acidic media (Figure 1.31) are corroborated by single PEM fuel cell measurements. Polarization and durability curves were collected, on a membrane electrode assembly (MEA) employing a FePhen@MOF-ArNH_3 cathode, under the U.S. Department of Energy (US DOE) suggested testing conditions of 80 °C, 100% relative humidity, 1 bar partial pressure of H_2/O_2 (1.5 bar total pressure) and/or 0.4 bar partial pressure of O_2 in H_2/air (2.5 bar total pressure). In a H_2/O_2 fuel cell FePhenMOF-ArNH_3 MEA generated a kinetic current density of more than 100 mA/cm^2 at 0.8 $V_{iR\text{-}free}$ (a detailed discussion is given later in the fuel cell testing section), ranking it as one of the most active non-PGM cathodes reported to date with no FeN_x moieties. Non-PGM cathodes require higher catalyst loadings (3 mg/cm^2 compared to 0.4 mg_{Pt}/cm^2 for Pt/C) that traditionally introduces mass-transport limitations, however FePhen@MOF-ArNH_3 was able to reach 75% the power density of a state-of-the-art Pt/C cathode run under the same conditions. Although microporosity is a prerequisite for good catalytic activity in non-PGM's, mesopores are essential for effective mass-transport, and we believe the increase in mesoporosity upon heat-treatment imparted superior mass-transport properties that

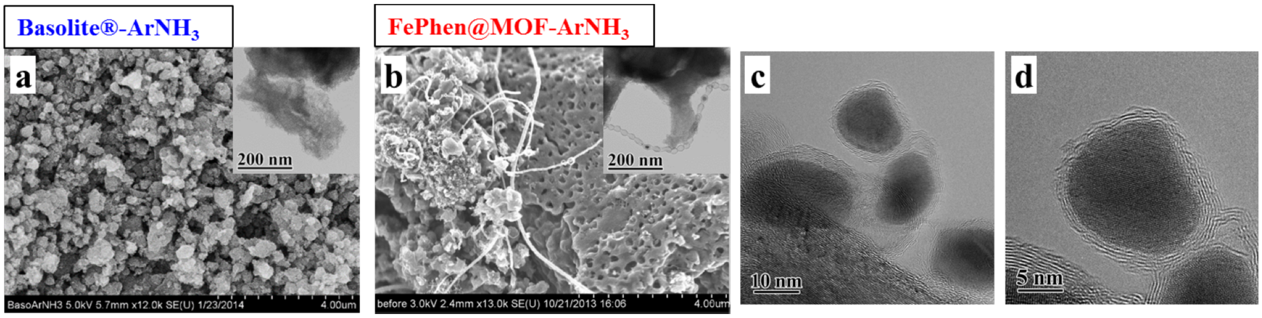

Figure 1.29: (a) SEM image of Basolite-ArNH_3, inset TEM image of amorphous carbon, scale bar 100 nm. (b) SEM image of FePhen@MOF-ArNH_3, inset TEM image of bamboo-jointed CNT, scale bar 100 nm. (c) HR-TEM image of iron encapsulated in bamboo-joints of CNT in FePhen@MOF-ArNH_3, scale bar 10 nm. (d) HR-TEM image of Fe/Fe_3C nanoparticle surrounded by graphite layers, scale bar 5 nm.

result in the enhanced activity.

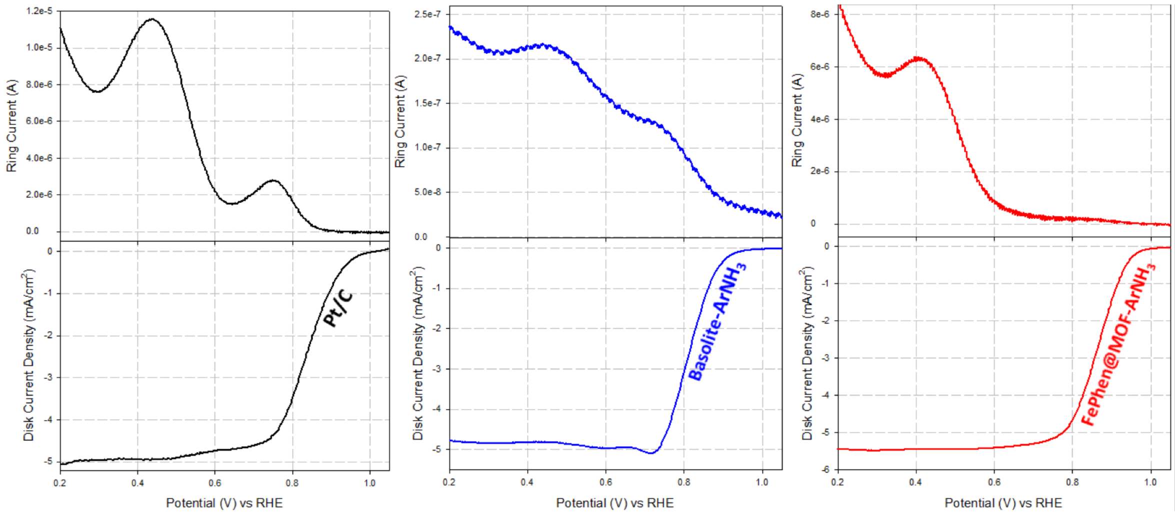

Figure 1.30: Disk- and ring-currents measured during ORR on Tanaka Pt/C, Basolite-ArNH$_3$ and FePhen@MOF-ArNH$_3$ in O_2 saturated 0.1M KOH electrolyte at 20 mV/s with rotation rate of 1600 rpm. E_{ring}=1.1 V vs RHE. Ring-current due to peroxide oxidation coincides with onset of reduction at the disk or Pt/C and Basolite-ArNH$_3$, however with FePhen@MOF-ArNH$_3$ oxidation of peroxide is shifted cathodically and attributed by the quinone functionalities on the carbon.

Identification of Fe-coordination

Earlier observations of heat treated Fe-TPP[17] (heat treatment of existing macrocycle) and PVAG-Fe[40] (Fe-based catalysts prepared from precursors using a reactive polymer approach), clearly indicated the presence of Fe-N$_x$ active sites in addition to relatively small but stable Fe NPs in both electrocatalysts despite the different precursors/synthetic routes used. They also represent different types of defect structures on the carbon and hence Fe spin states. Among the key features associated with ORR on such Fe-N$_x$ containing electrocatalyst elucidated using *in situ* XAS are (a) The Fe^{2+}-N$_4$ active site undergoes a redox transition to (H)O-Fe^{3+}-N$_4$ between 0.7 and 0.9 V vs. RHE, which correlates with an edge shift of the X-ray absorption near-edge spectra (XANES) characteristic of such a change in oxidation state with increasing potential (Figure 1.34 a and (b) a concomitant increase in the magnitude of the FT peak at ~1.6 Å (associated with Fe-N/O scattering) in the same corresponding potential showing oxide formation on the Fe in oxidation st

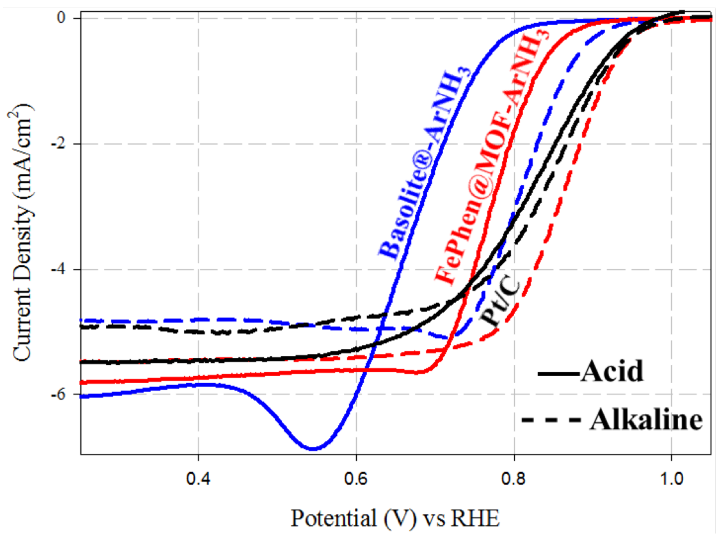

Figure 1.31: ORR polarization plots collected with FePhen@MOF-ArNH$_3$, Basolite-ArNH$_3$ and Tanaka Pt/C in O_2 saturated electrolyte (0.1M $HClO_4$ and 0.1M KOH) at 20 mV/s with rotation rate of 1600 rpm at room temperature.

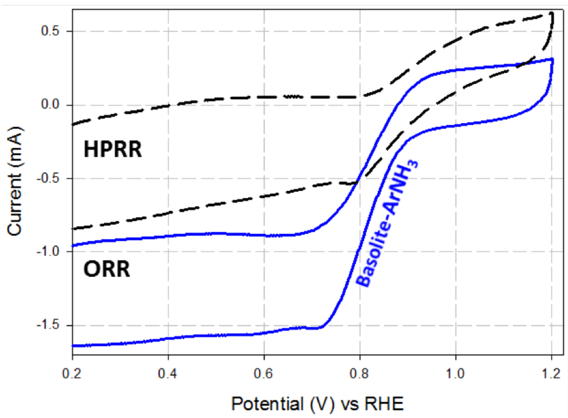

Figure 1.32: Rotating disk electrode (RDE) ORR polarization plots. Disk-currents measured on Basolite-$ArNH_3$ and FePhen@MOF-$ArNH_3$ in O_2 saturated 0.1M KOH electrolyte at 20 mV/s with rotation rate of 1600 rpm at room temperature. HPRR is shown in Ar saturated electrolyte with 3.5 mM H_2O_2 added externally. Basolite-$ArNH_3$ and FePhen@MOF-$ArNH_3$ did not show HPRR activity.

ate 3 (Figure 1.34 b). Fe^{III}-N_x (OH) formation close to 0.9 V vs. RHE clearly indicated by the forward FT at Fe K-edge (Figure 1.34 b) also means that the onset of oxygen reduction is intimately related to such a redox transition (this is also supported by redox peaks in alkaline and acidic media). In contrast to these observations on non-PGM catalysts containing Fe-N_x coordination, the Fe K edge FT of the EXAFS for FePhen@MOF-$ArNH_3$ does not contain the characteristic Fe-N/O peak at 1.6 Å (indicative of Fe-N interaction at and below 0.7 V and an additional Fe-O(H) interaction at higher potentials) and is characterized instead by a peak at ~2.2 Å coinciding with Fe-Fe scattering as seen by comparison with characteristic corresponding peaks from metallic Fe and Fe_3C standards. However, *in situ* XANES is much more sensitive than EXAFS at detecting the presence of FeN_x species and as the potential is increased the Fe K edge XANES energy of FePhen@MOF-$ArNH_3$ remains unchanged. These results also clearly point towards the fact that since FePhen@MOF-$ArNH_3$ constitutes of subsurface Fe/Fe_3C type moieties and their role in any Fenton's type peroxide induced free radical formation is

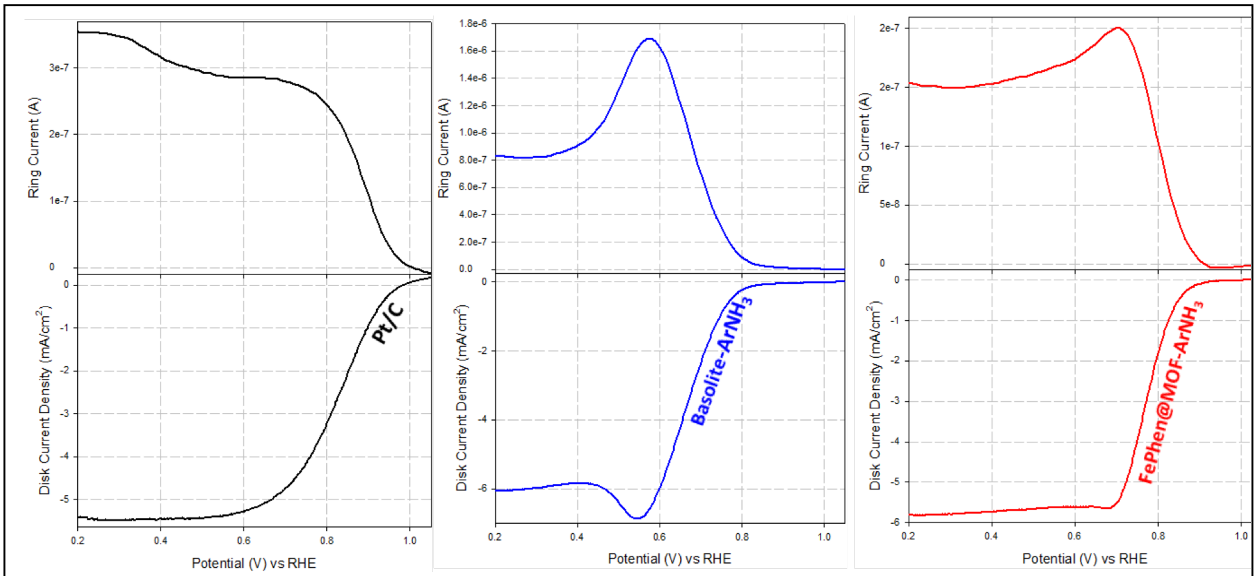

Figure 1.33: Disk- and ring-currents measured on Tanaka Pt/C, Basolite-$ArNH_3$, and FePhen@MOF-$ArNH_3$ in O_2 saturated 0.1M $HClO_4$ electrolyte at 20 mV/s with rotation rate of 1600 rpm at room temperature. E_{ring}=1.3 V vs RHE.

unlikely. This is a very critical distinction from the Fe-N_x based non-PGM electrocatalysts.

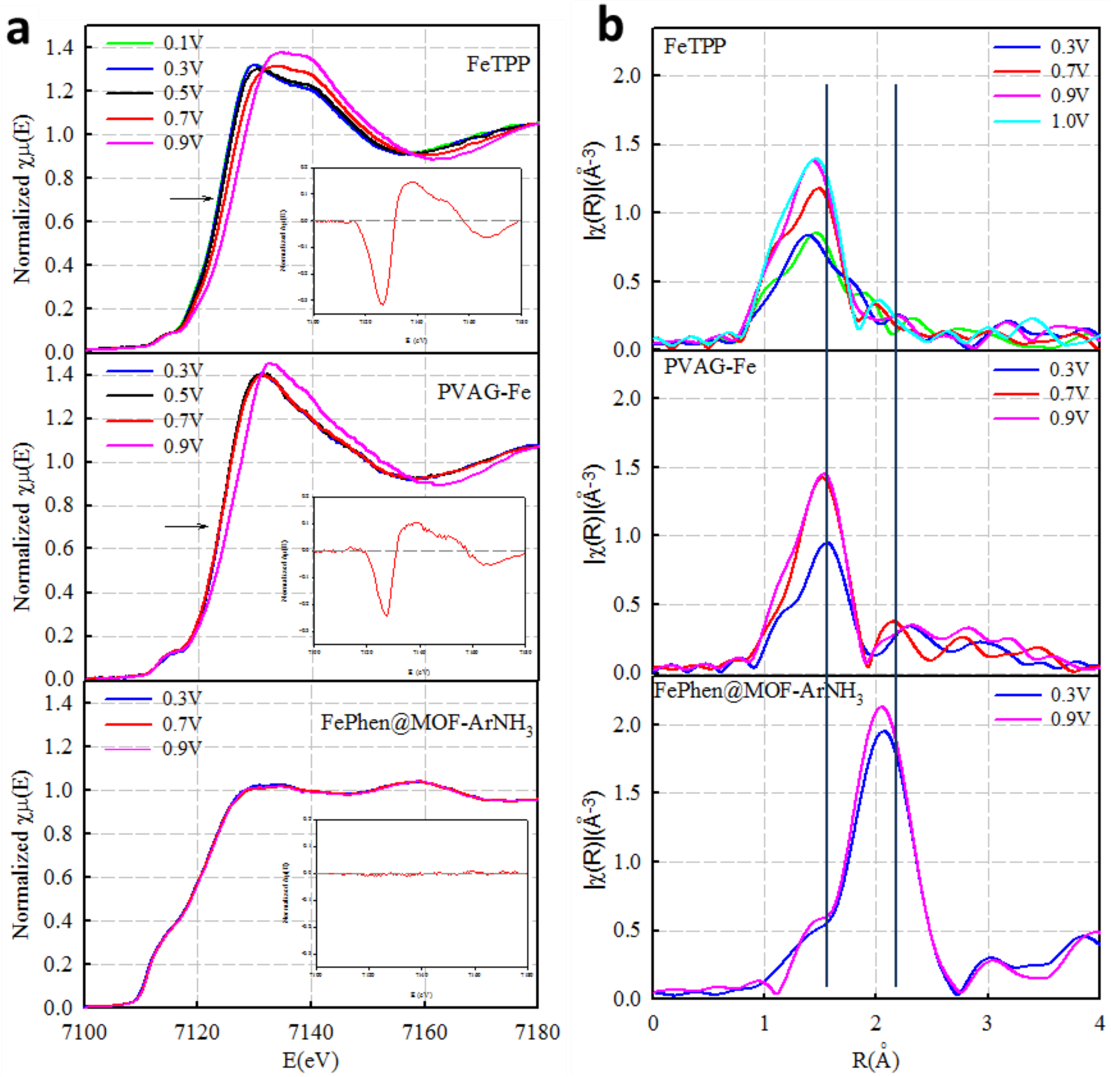

Figure 1.34: *In situ* XAS Investigation. Potential dependent normalized Fe K-edge XANES of FeTPP, PVAG-Fe, FePhen@MOF-ArNH$_3$ and carbon corroded Fe-Phen@MOF-ArNH$_3$ collected in N_2 saturated 0.1M $HClO_4$, inset $\Delta\mu = \mu$ (0.9 V) - μ (0.3 V). (d) Potential dependent FT-EXAFS of same electrocatalysts in b collected in O_2 saturated 0.1M $HClO_4$.

In conclusion, we introduced a Fe-based non-PGM ORR electrocatalysts, FePhen@MOF-ArNH$_3$, which utilizes a MOF-support that acts as a host for the Fe-based sites. Orderly dispersion of the Fe-chelates is achieved with the encapsulation synthesis and gives rise to an electrocatalyst with a distinct active site. In addition, FePhen@MOF-ArNH$_3$ exhibits one of the highest reported activities for ORR in acidic media and outperforms the benchmark Pt/C catalyst in alkaline media. The exceptional ORR activity measured using a RRDE setup in acid translated to the superior PEM fuel cell performance where FePhen@MOF-ArNH$_3$ showed excellent mass-transport properties and stability that has not been demonstrated by previous non-PGM cathodes. Characterization techniques revealed the Fe is present as Fe/Fe_3C nanoparticles that are sub-surface to N-doped carbon overlayer, however they seem to play an important role in the electrocatalysis by imparting a synergistic effect on the N-doped carbon that allows stabilization of the peroxide intermediate and enables the full 4e$^-$ reduction of oxygen to water. What sets this work apart from others is the definitive proof that this exceptionally active non-PGM electrocatalysts lacks direct Fe-N$_x$ coordination when studied using *in situ* synchrotron XAS at the Fe K-edge under simulated conditions of operating PEM cell. All previous reports in the literature have been obtained under *ex situ* conditions that cannot account for catalyst structure changes at the catalyst-electrolyte interface with an applied potential. This is the first Fe-based non-PGM catalyst reported to date that shows no empirical evidence of the Fe-N$_x$ coordination witnessed in the most active materials, but is predominantly comprised of Fe/Fe$_3$C nanoparticles encapsulated by N-doped carbon structure. The lack of evidence suggesting the presence of Fe-N$_x$ moieties under *in situ* conditions allows us to conclusively attribute the majority of the ORR activity to the N-doped carbon structure. Based on our results we believe the Fe first acts as a catalyst for the graphitization of N-doped carbon during the heat treatment in which some iron is integrated into the carbon and enhances the electrocatalytic properties enabling the 4 e$^-$ reduction of oxygen.

Task 1.5 Scale-up of Catalysts Formulations

Pajarito Powder is scaling up the Charge Transfer Salt (Fe-CTS) catalyst developed by the University of New Mexico (UNM) and Metal Organic Framework (MOF) based catalyst developed by Northeastern University for the DOE contract. The UNM catalyst is made using a Sacrificial Support Synthesis Method (SSM) developed at UNM where C/N precursors are mixed with iron metal salts and silica. The mixture is then pyrolized at ambient pressure, the silica and excess iron are etched and leached, and then pyrolyzed again to achieve better performance and stability. This chemically intensive approach has several key steps requiring optimization in the scale-up effort. The initial scale-up effort was focused on a 10-20 gram batch, then scaled to 50gram batches, with trajectory to 100+ gram batches established. For the previous grant period Pajarito scaled the Fe-CTS catalyst to 200 gram batch level, demonstrating improved performance and good intra-batch consistency levels.

The synthesis, physical characterization, and the PEMFC performance of the scaled-up Fe-CTS catalysts are summarized in Figure 1.35. The approach adopted for this catalyst involved blends of materials derived using two separate approaches: one of a University of New Mexico group's silica templating methodology, referred to as Fe-CTS, and a UNM-CBDZ approach. The Fe-CTS was derived using the mechano-chemical approach of ball milling an organic charge transfer salt (nicarbazin) in the presence of Fe salt and the latter using an aqueous formulation of a non-chelating material, carbendazim, with Fe salt, and both were supported on silica followed by

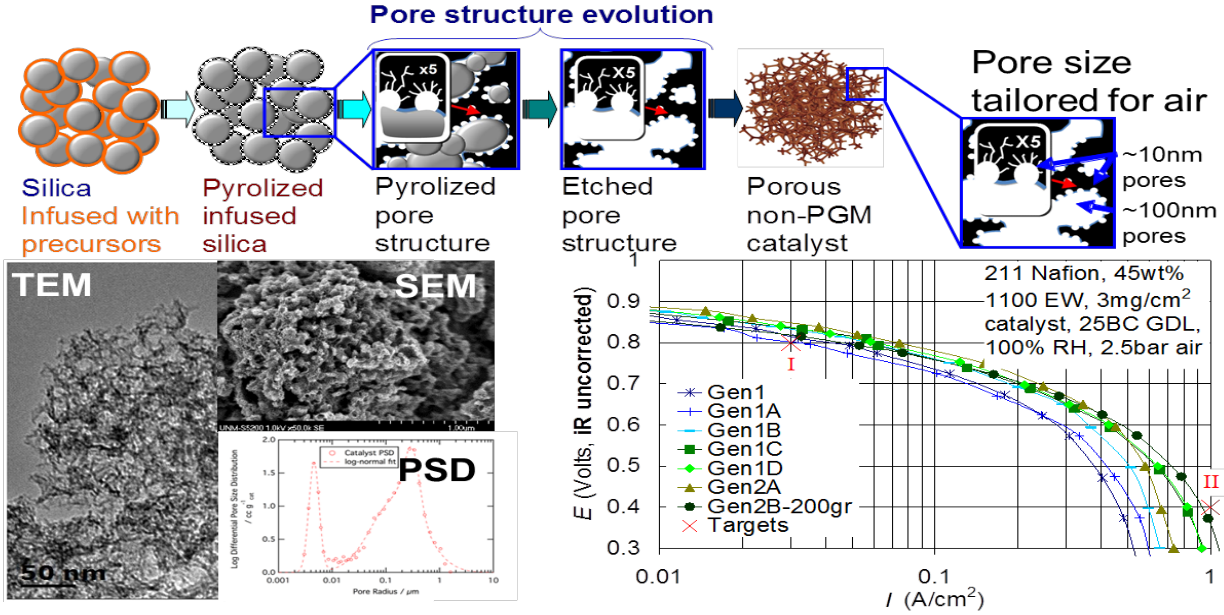

Figure 1.35. Fe-CTS catalyst porosity modified for air operations and scaled to 200gram per batch.

several pyrolysis and etching steps. Typical blends comprised of a 1:1 mixture. As a result, this catalyst exhibit a highly porous carbon matrix structure, which not only hosts high active site density, but also provides high mass transport; both are critical for PEMFC performance.

These materials were tested in single cells (5 cm^2) using a commercial anode electrode (Alfa Aesar) with a 0.1 mg/cm^2 Pt loading. The typical cathode loading was 3 mg/cm^2 and the membrane used was a Nafion® 211, with 50% Nafion® loading at the cathode. Tests were conducted under steady-state potentiostatic conditions with each point measured for a minimum of 60 s. In this annual report all reported tests were conducted at PPC using scaled up batches of 50 grams and above for the Fe-CTS approach. Common test protocols were replicated at Nissan Technical Center North America (NTCNA) and Northeastern University (NEU). Durability measurements were performed using two well-established protocols (catalyst durability) and carbon corrosion tests (both are DOE protocols).

PPC has scaled up formulations of both the Fe-CTS sample and the NEU-developed approach and also modified the Fe-CTS catalyst for improved performance. Brief descriptions of the approaches employed for both catalysts are given sbove. The Fe-CTS catalyst was reformulated to (a) improve mass transport to meet the areal activity target in hydrogen/air as well as to (b) provide higher durability under the two above-mentioned (see approach section) DOE mandated protocols. The chemically intensive approach for scale up involved several key steps requiring optimization. The initial scale up effort was focused on a 10-20 gram batch with the goal that the methods developed could be applied for synthesizing between 30 and 50 grams, with a long-term goal of 200-gram batches.

Demonstration of progress towards 200-gram per batch synthesis of the original Fe-CTS catalyst involved pre-treatment of precursors to reduce and eliminate residual precursors and batch consistency effects on manufacturing. As mentioned above the milestone is to meet the hydrogen/air areal performance target of 30 mA/cm^2 @ 0.8 V and 1000 mA/cm^2 @ 0.4V in 2.5 bar air and 80 ^{o}C at 100% humidification.

Progress towards 200-gram batches was established through use of larger volume processing equipment, processing vessel materials changes, and tuning of processing parameters such as the pyrolysis temperature trajectory, etching times and agitations, and mixing times and intensity. In this way, 200-gram batches have been prepared. In addition, the PEMFC performance of the scaled-up catalyst meets up the DOE target (Figure 1.35).

A brief summary illustrating these developments is presented showing a nearly 80% improvement in performance in air (compared to previous reporting period) with 70 mA/cm^2 @ 0.8V and 1000 mA/cm^2 @ 0.8V achieved using 3mg/cm^2 loading gas diffusion electrodes. Figure 1.35 (a), shows two separate blend formulations, Gen 1 and Gen 2, made using variations in silica templates. Comparison of Gen 2 (100% CTS batch) and Gen 2A (CTS/CBDZ blend with variation of silica template show remarkable inter-batch reproducibility in hydrogen/air performance in accordance to this project's targeted operating conditions. The low current density target of 30 mA/cm^2 at 0.8 V (uncorrected) has been met and exceeded with current state-of-the-art performance at 70 mA/cm^2 current density. The higher current density target of 1 A/cm^2 at 0.4 V (infrared (IR)-corrected) (Q-2, FY15 end of project target) has nearly been met with an uncorrected current activity of 0.92 A/cm^2 (uncorrected) and 1.05A/cm^2 (IR-corrected). These performance figures are better delineated in the corresponding Tafel (semi-log plot) shown in Figure 1.35 (a). Both of these results are reported without any IR correction.

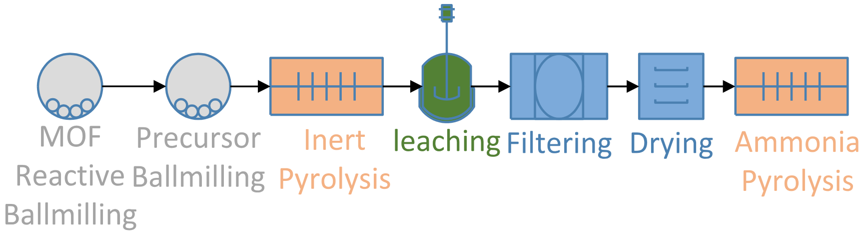

In the next period Pajarito concentrated on ongoing Technology transfer and scale up for the MOF catalysts from NEU. Technology transfer and scale up for the NEU MOF based catalysts continues in Q1 (2015). In the past period agreements with NEU have been put in place and preliminary discussion has identified unique processing equipment and supplies needed for the technology transfer and scale up. These have been identified to be large volume centrifugation and ball-milling containers and media, as well as high temperature processing tubes. All of these have now been ordered and delivered as have a beginning set of precursors identified. Lengthy visits by Pajarito personnel to NEU led to creating of SOPs and critical points of manufacturing to be: 1) Making the MOF 2) Mixing the MOF and precursors 3) and pyrolysis a) in Inert atmosphere and b) in reactive atmosphere. Further, a series of materials at the different stages of manufacturing identified have been sent and are being characterized to determine point of congruency in the processing.

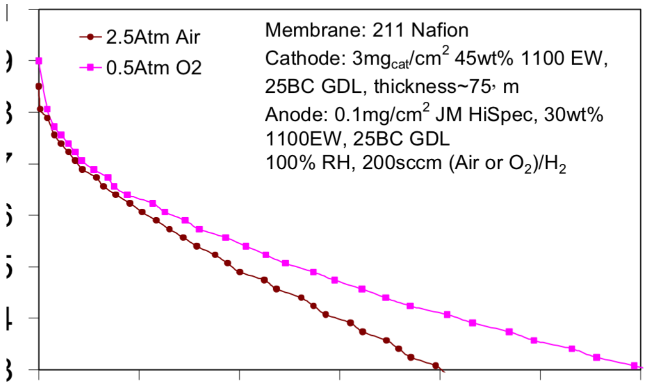

Figure 1.36 Steady state polarization measurements reported on scaled up NEU-MOF catalysts measured in both H_2/O_2 (1.5 bar total pressure) and H_2/Air (2.5 bar total pressure).

Progress on the scale up of the first stage has been steady, with several different milling containers, media, and intensity attempted in an attempt to make the MOF through reactive ball-milling. A combination of very gentle and high intensity mixing seems to be best for 20x sizes with XRD illustrating the formation of MOF phases. Alternate formulations and key descriptors such as surface area and tapped density are being identified and correct measurement techniques being developed, since standard degassing techniques for example lead to precursor degradation.

In addition, several catalyst batches made entirely at Pajarito have shown promising performance, as illustrated. Membrane electrode Assemblies(5cm^2) were made from Gas Diffusion Electrodes(GDE) pressed onto 211 Nafion® membrane with PTFE-impregnated glass-fiber sub-gaskets at 131°C for 10minutes under 450psi, then allowed to cool under 1psi pressure. Sub-gaskets thickness for the anode was 150 micrometer and 250micrometer for the cathode. The gas diffusion electrode were sprayed using Sono-tek Exacta-Coat automated spray system delivering 3 ml/min ink through a 25kHz ultrasonic nozzle onto SGL 25BC Gas Diffusion Layer(GDL) materials heated to 65°C. Ink was deposited in a rate of 40microgram/cm^2 per deposition pass. The ink was composed of 4mL Isopropyl Alcohol, 2mL deionized water, 200mg of catalyst, and 300mgs D2021 Nafion® dispersion. A 50mL vessel containing the ink ingredients was placed in a water bath and mixed for 30minutes using an IKA T-18 high shear mixer with S18-19G dispersing element set for 18,000RPM.

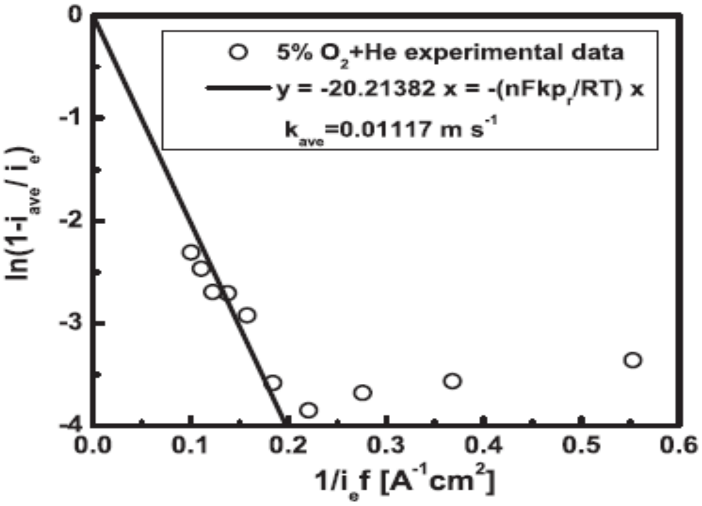

Figure 1. 37. Ratio of limiting current to theoretical limiting current as a function of flow rate.

The MEAs were loaded into the cell testing assembly using single serpentine pattern graphite flow plates and the cell hardware was assembled using 4.5N torque. The cell was allowed to come up to temperature under a feed 200sccm of 90% RH O_2 and H_2 and pressurized to a total of 1.5Atm total pressure. After cell temperature reached 80°C load was applied potentiostatically to 0.8V for 10 minutes, and 2 sequential polarization curves were measured. Polarization curves were also measured potentiostatically, with current measurement after 60 second hold at each potential. Ongoing work continues with scale up efforts focused on 20x scale manufacturing of MOF, adjusting thermal treatment, and yield improvement scheduled for Q2. Pajarito is currently on schedule for successful completion of all contracted scale-up work on both catalyst formulations by the end of the grant period II.

Helox Experiments on NEU-MOF Catalysts:

As a control, steady state polarization measurements were conducted using a 5 cm^2 single cell with anode and cathode electrodes comprising of 0.4mg Pt/cm^2 in conjunction with a Nafion 211 membrane. This was compared with an MEA comprising of NEU-MOF solution reaction catalyst incorporated onto a Sigracet BC25 GDL (2.7mg/cm^2) as cathode and a premade 0.4mg/cm^2 Pt/C anode electrode from Johnson Matthey Fuel Cells (ELE0162), using the same membrane.

Studies were conducted in order to analyze the difference in the mass transport capabilities and limitations of the MOF catalyst compared to the platinum standard. Once the platinum sample was established as having a high performance baseline via polarization curves taken at various backpressures both in oxygen as well as in air, polarization curves were taken at 8 different flow rates using 3 cathode gasses. The cathode gasses used in these cases were all 4% oxygen, but using a series of inert carrier gasses (He, Ar, N_2). Flow rates were established using the St-Pierre et al methodology of maintaining an optimum stoichiometry for water transport in the cell. The gas flows used (sccm anode gas/sccm cathode gas) were as follows: 424/1008, 376/882, 318/756, 260/627, 212/504, 154/366, 77/183, 38/91. This procedure was followed for both the Platinum standard MEA as well as the MOF MEA.

With both the platinum MEA as well as with the MOF MEA, the varying of the flow rate had a direct impact on the maximum achievable limiting current. When mass transport factors were calculated from the platinum cell, they showed a good correlation to the St-Pierre et. al., data, while the slight deviations can be accounted for in that the operating temperature in this case was 80C, while the St-Pierre et al experiments utilized a 60C operating temperature. Mass transport factors were calculated by plotting $\ln(1-(i_{ave}/i_e))$ vs $(1/i_e f)$ where i_{ave} is the limiting current, i_e is the inlet reactant flow rate equivalency current density, and $i_e f$ is proportional to the flow rate. A line was fitted to this data, with the slope being equal to -nFkp/RT, with k representing the mass transport (MT) coefficient, and 1/k representing the mass transport resistance. The figure 1.37 below (from the St-Pierre literature) shows the above process by which the mass transport resistances are calculated.

Gas	St-Pierre Pt Lit. MT Resistance	NEU Pt MT Coefficient	NEU Pt MT Resistance (m s-1)	NEU MOF SR MT Coefficient	NEU MOF SR MT Resistance (m s-1)
4% O2 + N2	140	0.005016	194	0.0009465	1060
4% O2 + He	89	0.00817	122	0.001178	850

Table 1.6 PEMFC testing parameters and results on scaled Fe-based catalysts.

When the same transport factors were calculated for the MOF catalyst, it was determined that the mass transport resistances were 8-10 times higher for the MOF than for the platinum cell. Below is a table showing the NEU mass transport data for platinum as well as MOF compared to the St-Pierre literature data. The argon data is currently excluded, as it needs to be confirmed due to a potential issue during the testing.

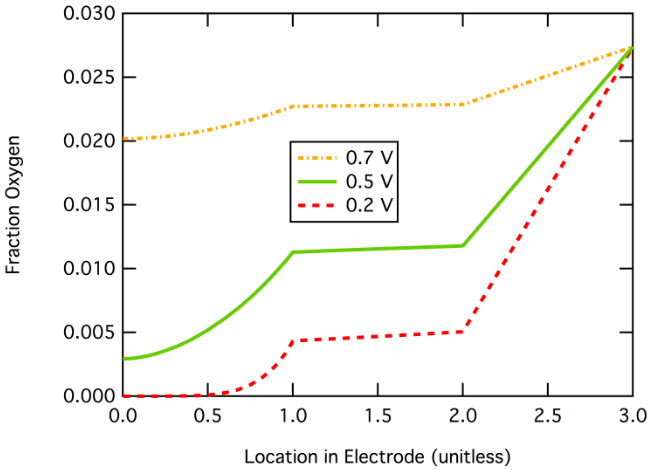

Figure 1.38. Oxygen fraction at various locations within the cathode. The left side represents the catalysts layer, the middle (between 1 and 2) represents the gas diffusion layer, and right side represents the channel.

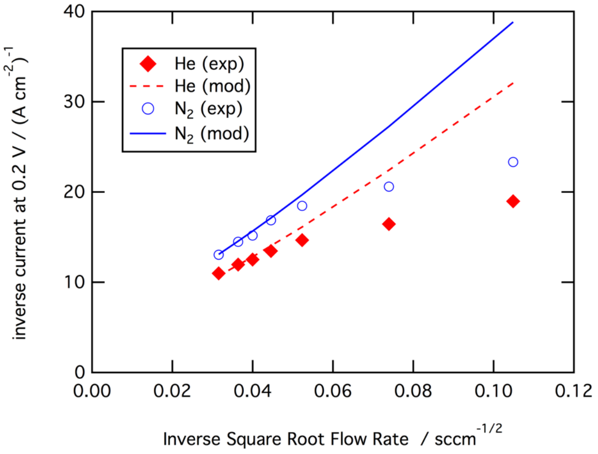

Figure 1.39. Plot of current at 0.2 V as it varies with square root of cathode flow rate.

Preliminary mass transport studies have begun on the scaled-up synthesis of the solid state reaction MOF from Pajarito Powder, although those studies are not yet complete.

Model Results based on NEU MOF Catalyst

An electrode-scale, transport model for a proton-exchange-membrane fuel cell (PEMFC) cathode has been developed in previous reports. This report considers improvements to this model with regards to understanding the impact of flow rates and diluents on the cathode system. It was found that transport losses are attributable to oxygen diffusion limitations in the catalyst layer as well as mass transfer to the channel. The model was used to fit MEA data obtained at four different oxidant flow rates: 504, 627, 756, and 1008 sccm by **Northeastern University**. The cathode inlet flow was composed of 4% oxygen in various dilutants (He and N_2). The parameters fit were hydrophobic pore fraction (for GDL and CL), exchange current density, boundary layer coefficient, and catalyst layer ionic conductivity. The boundary layer coefficient represents and effective parameter that establishes the boundary layer thickness in the channel based on Reynolds number and Schmidt number. A comparison of the model with experimental values is shown in Figure 1.39.

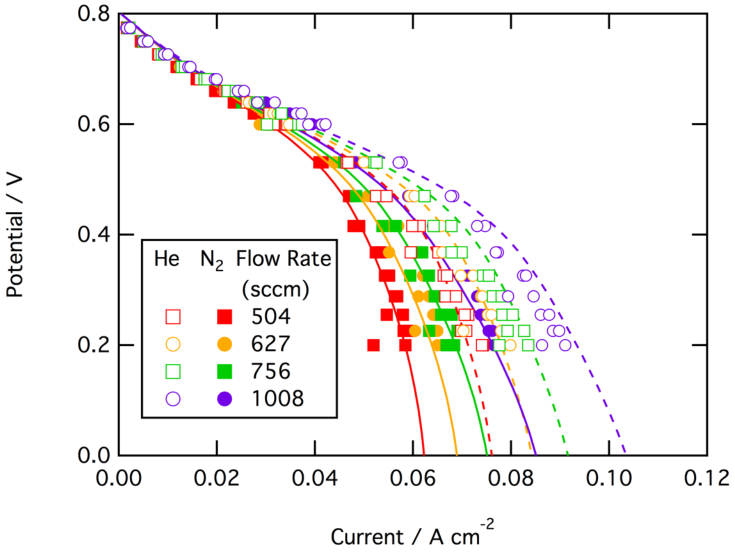

Figure 1.39. Comparison of experimental and model results at four different gas flow rates containing 4 % oxygen. Conditions: Temp. 80 C, 25BC GDL, 2.6 mg/cm^2 Catalyst Loading, 45 wt% Nafion, Cell Area: 4.62cm^2

The fit parameters can be compared to values found previously with the Pajarito Powder (PPC) catalyst. The most notable difference is the ionic conductivity in the catalyst layer. The MOF catalyst shows an ionic conductivity of 2.5 mS/cm whereas the PPC catalyst showed 18.1 mS/cm. The poor conductivity is indicated in steep slopes of the transport-limited regime. The hydrophobic pore fraction of the MOF catalyst (16%) was slightly lower than the PPC catalyst (29%). The effective exchange current density for the MOF catalyst was 3.3 $A/cm^3/bar\ O_2$, which is less than the PPC catalyst (8.6 $A/cm^3/bar\ O_2$). This lower performance can be partially attributable to the lower hydrophobicity of the MOF catalyst, and indicates the need for better water management strategies in the catalyst layer.

Now that the fit has been established, profiles in the catalyst layer can be used to better understand transport phenomena. Figure 1.38 shows oxygen fraction profiles at three different potentials. The large gradients on both sides of the graph indicate that oxygen diffusion limitations occur primarily in the channel and catalyst layer. The relative flatness in the center region indicates that the gas diffusion layer does not cause a significant amount of diffusion limitations.

Looking at the flow rate dependence at low potentials elucidates the impact of convection on the cathode. A plot of inverse square root of the flow rate and inverse current density is shown in Figure 1.39. The linear slope confirms the assumption made in the model that the diffusional boundary layer scales with flow rate to the negative one half power. On the right side of the plot the model deviates from the experimental data, these points represent the slower flow rates. This deviation could be due to a second flow regime at these low flow rates.

Task 2/5. Development of Novel Reaction Layer Formulations and Design of Gas Diffusion Medium for Enhanced Mass Transport and Fabrication of Membrane Electrode Assemblies

Although Metal-Nitrogen-Carbon (MNC) catalysts are a potential solution to the cost and availability challenges that come with using PGMs, these catalysts generally involve lower volume-specific activity than platinum, which results in thicker electrodes. It has been previously proposed that a low-cost catalyst may be allowed to have 10-fold lower activity than platinum, as long as the catalyst layer was 10-fold thicker.[41] This proposal was based on the assumption that transport loses would not be significant in this thickness regime. This task is to understand quantitatively how the thickness of these electrodes will impact membrane electrode assembly (MEA) performance for MNC catalyst.

A number of models have addressed electrode scale transport issues.[42,43] These models generally concentrate on water flooding in the gas diffusion layer (GDL) and consider a relatively thin catalyst layer. Here, gas and liquid transport in the catalyst layer are considered in a way that is similar to treatment of gas diffusion layers in previous models. We also treat the GDL consistently with previous models.

Multiple works have addressed gas diffusion in the cathode catalyst layers,[44,45], with a subset considering flooding impacts on gas diffusion.[46] The works that do consider flooding are primarily concerned with thin, precious-metal catalyzed layers of ~10 μm thickness.[46] In the task, we consider the impact of flooding on both electrochemically active surface area (ECSA) and gas diffusion in catalyst layers of 60–120 μm thickness. ECSA impact is treated by incorporating a flooding term in the kinetics model similar to Eikerling et al. Treatment of gas diffusion limitations are based on the decrease in effective porosity due to flooding, as well as the dilution of oxygen by water vapor and nitrogen, similar to the treatment of the GDL by Weber *et al.*[47] This second consideration is likely more significant than in thin Pt-based catalyst layers due to increased catalyst layer thickness as well as the increased hydrophilicity that can accompany heat-treated carbon materials.

Experimental Catalysts were synthesized by Pajarito Powder using the previously introduced Fe-CTS catalyst. To summarize, a silica template material is thoroughly mixed with iron nitrate and various nitrogen precursors. After pyrolyzing the mixture, the silica template is removed by etching in hydrofluoric acid. A second pyrolysis follows etching. Catalyst ink containing a 9:11 mass ratio of ionomer to catalyst with 500 mg catalyst per 20 mL solvent was sprayed on a 5 cm2 Sigracet 25BC GDL using a Sono-tek Exacta-Coat automated spray system. The catalyst layer (CL) plus GDL was assembled with a 211 membrane and an anode containing 0.2 mg_{Pt}/cm^2. This assembly was hot pressed at 131◦C and 90 psi for six minutes. MEAs, fabricated as explained in previous section, were loaded onto single serpentine pattern graphite flow plates and assembled with 4.5 N torque. The cells was allowed to equilibrate under a feed of 200 sccm, 1.5 bar total pressure. After reaching a temperature of 80◦C, they were broken in by holding for 15 minutes at 0.3 and 0.6 V. MEA activity was measured potentiostatically at various backpressures over a potential range from open-circuit voltage (OCV) to 0.3 V, and then back to OCV. At each potential, a current was recorded after a one minute hold, and a high frequency resistance measurement was recorded. The MEA was poised at 0.6 V for 15 minutes between polarization measurements. For additional break-in, an initial polarization from OCV to 0.3 V and back was discarded. Inlet gases were hydrogen and air at 100% relative humidity and 200 sccm. Electrochemical impedance spectroscopy (EIS) was used to analyze two electrodes of loadings 2 mg/cm2 and 4 mg/cm2. Spectra were obtained using a 10 mA/cm2 amplitude sinusoidal current signal over the frequency range of 10 kHz to 1 Hz with 10 frequency per decade.

Physical characterization. Catalyst layer material for physical characterization was created by spraying the catalyst ink onto a glass plate. Catalyst ink contained a 9:11 mass ratio of ionomer to catalyst with 500 mg catalyst per 20 mL solvent. After the material was dry, it was scraped off and compressed into pellets for porosity measurements. Porosity measurements were taken of the pure catalyst as well as of catalyst/ionomer pellets. Three pellets were tested of varying densities as shown in Fig 2: 0.222, 0.304, and 0.336 g/cc.

The pore size distribution (PSD) of catalyst layer material was measured via mercury intrusion porosimetry (Micromeritics AutoPore IV 9500.) A 3 mL penetrometer with a stem volume of 1.1 mL was loaded with 0.1 g of CL material. Mercury intrusion was measured over the pressure range of 0.1 to 30000 psi$_a$. The pressure is related to a pore radius with the Washburn equation:[48]

$$r_\mathrm{p} = \frac{2\gamma\cos\theta}{p_\mathrm{meas}} \qquad [1]$$

where the measured pressure, p_meas, contact angle, θ, and surface tension of mercury, γ, establish the pore radius, r_p. In this way the change in mercury volume from one pressure to another can be associated with intrusion into a certain pore size and a pore size distribution can be calculated.

Model Description

This section describes the governing equations for a two-region, multi-phase, transport model of an electrolyte membrane - catalyst layer (CL) - gas diffusion layer (GDL) assembly. This one-dimensional, steady-state model consists of two regions (CL and GDL) with the electrolyte membrane being considered as a boundary condition at the CL surface (Figure 2.1). Each region has different properties, but the governing equations are similar.

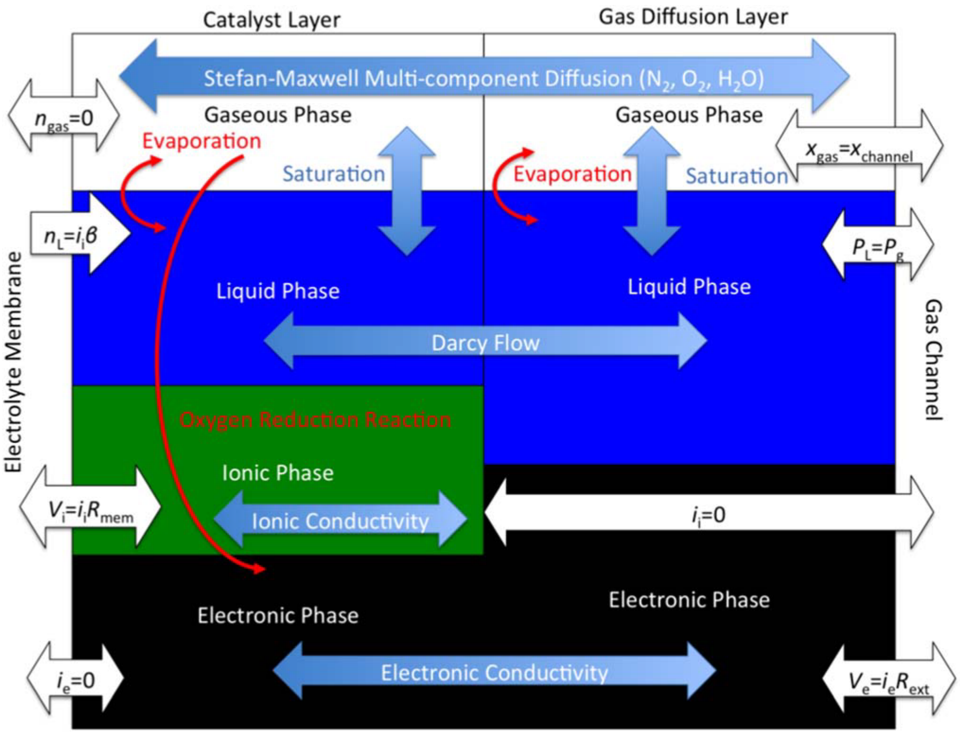

Figure 2.1. Schematic of cathode showing different phases and regions of the model with boundary conditions (black-outlined, white arrows), transport phenomena (blue arrows), and generation terms (red arrows).

Within each region there are four phases: an electron-conducting solid phase, an ion-conducting ionic phase, and non-conducting liquid and gas phases. The primary dependent variables in these phases are electronic phase potential, V_e, ionic phase potential, V_i, liquid pressure, P_L; and vapor fractions of oxygen and water vapor, x_o and x_w. Currents and species flux are also dependent variables, but can all be related to gradients of primary dependent variables, as discussed in detail below. The governing equations consider the conservation of electrons, protons, liquid water, and water vapor (Equations **Error! Reference source not found.**, **Error! Reference source not found.**, and **Error! Reference source not found.** respectively):

$$0 = -\kappa_{\mathrm{e}} \nabla^2 V_{\mathrm{e}} + nFr_{\mathrm{ORR}} \qquad [2]$$

$$0 = -\kappa_{\mathrm{i}} \nabla^2 V_{\mathrm{i}} - nFr_{\mathrm{ORR}} \qquad [3]$$

$$0 = -\frac{k_{\mathrm{L}}}{\mu} \nabla^2 P_{\mathrm{L}} + 2r_{\mathrm{ORR}} - r_{\mathrm{evap}} \qquad [4]$$

$$\nabla N_{\mathrm{w}} = r_{\mathrm{evap}} \qquad [5]$$

where κ_e is electronic conductivity, V_e is electronic phase potential, n is electrons per mole oxygen, F is Faraday's constant, r_{ORR} is an oxygen reduction reaction rate, κ_i is ionic conductivity, V_i is ionic potential, k_L is liquid permeability (a function of saturation), μ is viscosity, P_L is liquid pressure, r_{evap} is an evaporation rate, and N_w is flux of water vapor. Flux of nitrogen in air is set to zero everywhere, because it does not participate in any reaction, and the membrane is considered to be gas-impermeable.

Boundary conditions for the governing equations fall into three categories: membrane, CL-GDL interface, and channel (shown in Figure 2.1 in the black-outlined, white arrows). The membrane is treated as an electrical insulator (i_e =0), with ionic resistance, R_{mem}, that leads to an ohmic drop $V_i = i_i * R_{mem}$ in the electrolyte phase. Electroosmotic flux of water through the membrane is calculated based on flux coefficient, β_{mem}, via the equation: $N_L = i_i * \beta_{mem} / F$.[49,50] The coefficient is a function of pressure as discovered by Jansen and shown in Table 4.[50] The membrane is also considered gas impermeable ($N_w = N_n = N_o = 0$). At the CL-GDL interface, all variables are considered continuous. The channel boundary is treated as an ionic insulator (i_i =0), and the solid phase overpotential at the channel is $V_e = i_e * R_{ext}$ to account for external resistances not included in this model (current collectors, contact resistances, bipolar plates, anode, and anode GDL). The resistance R_{ext} was estimated by subtracting GDL, membrane, and CL resistances from measured high frequency resistance. Using this approach, experimental data did not have to be iR corrected prior to fitting. At the channel boundary, all concentrations are fixed to bulk conditions for the inlet gas. The liquid phase pressure is in equilibrium with the gas phase pressure, making the capillary pressure zero.

Porous Phase. Void space in the catalyst layer consists of water-filled hydrophilic pores with contact angles less than 90°, and hydrophobic pores with contact angle $\theta_{\mathrm{obs}} \geq 90^{\circ}$, and filled by a combination of liquid and gas phases. The fraction of pores that are flooded with water is given by saturation, S, a measure of flooding. Saturation is in turn controlled by the capillary pressure, p_c, which is the pressure difference between the liquid phase and gas phase. Saturation impacts electrochemically active surface area as well as effective permeability and gas diffusivity. For hydrophilic pores, $S = 1$, because capillary pressure is always positive due to the generation of liquid water via oxygen reduction: the liquid flux results in a pressure gradient away from the channel. This gradient and boundary condition ensure all liquid pressures are greater than the gas pressure, which is considered constant and equal to the channel gas pressure.

In order to consider hydrophobic pores, a contact angle is required. The intrinsic catalyst contact angle was found to be hydrophilic because catalysts pellets were wetted by water. For this reason, it was assumed that hydrophobicity is caused by a combination of ionomer hydrophobicity and trapped air pockets. To model this phenomenon, a hydrophobic pore fraction was fitted to experimental data. Based on the hypothesis that the ionomer was a source of hydrophobicity, the hydrophobic contact angle was set to the contact angle of Nafion clusters, 90.02°, as calculated by Weber et al.[51]

For hydrophobic pores, the capillary pressure, p_c, apparent contact angle, θ_{obs}, and surface tension of water, γ, define a critical pore radius, r_c, via the Washburn equation:[42,52-54]

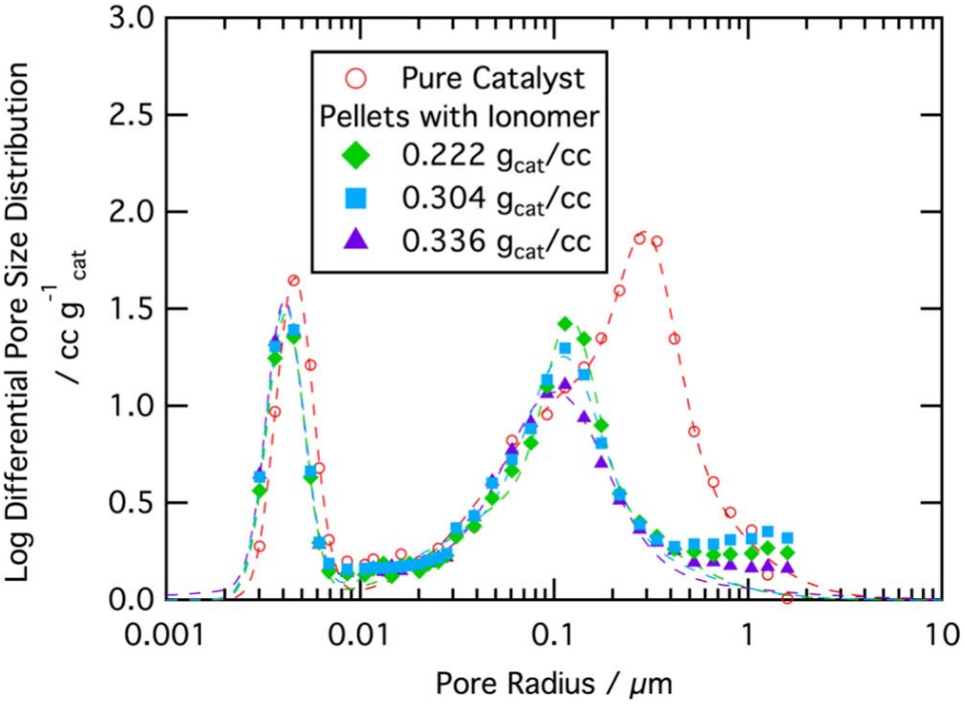

Figure 2.2. Pore size distribution of catalyst as well as three different pellets of catalyst layer material (including ionomer) as measured by mercury intrusion porosimetry with a fit composed of three lognormal pore size distributions. Fit characteristics are included in Table 2.1.

The saturation, S, of hydrophobic pores can be calculated by summing the volume of pores larger than the critical radius, r_c. This can be performed via an integration of the pore size distribution:[42]

$$S = \frac{\int_{r_c}^{\infty} \frac{dV}{dr} dr}{\int_{0}^{\infty} \frac{dV}{dr} dr} \qquad [2]$$

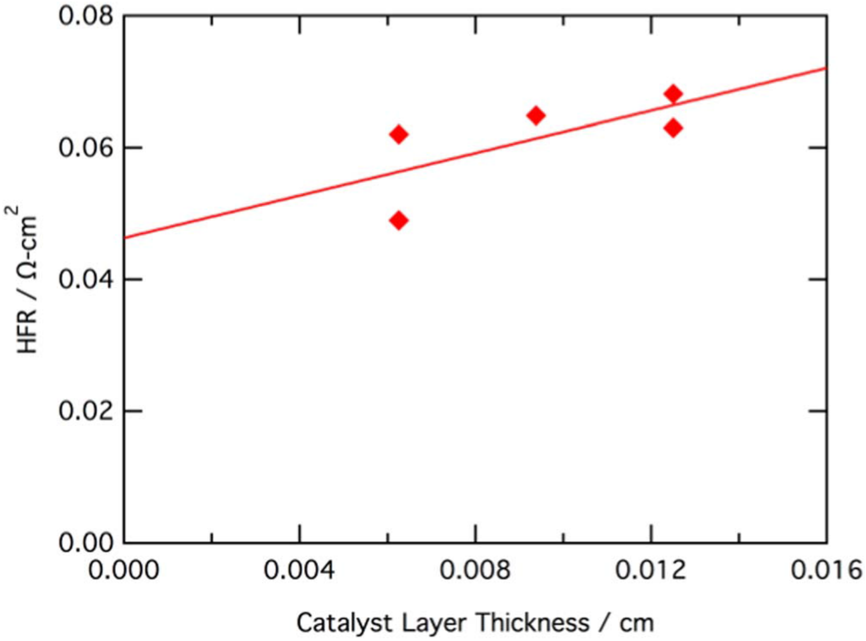

Figure 2.3. Conductivity of catalyst layer material by correlating high frequency resistance (HFR)with thickness of catalyst layers with varying loadings at constant density.

Essentially, as capillary pressure increases, water is forced into increasingly smaller pore sizes. Although direct integration of a measured pore size distribution (PSD) is achievable, a set of log-normal PSDs (LNPSDs) can be used to describe the PSD to make further calculations more manageable.[52] The use of lognormal PSDs also allows a means to differentiate pore modes. From the PSDs shown in Figure 2.2 it is evident that there are three different characteristic pore sizes: a small narrow pore size around 5 nm radius and a broad pore mode at around 300 nm radius (for neat catalyst) with a shoulder representing another characteristic pore size at a slightly smaller radius (at 100 nm for neat catalyst). Performing porosimetry of pellets composed of catalyst layer material (containing ionomer) allows the impact of the ionomer on porosity to be observed. By comparing porosity with and without ionomer it is evident that ionomer content primarily impacts macroporous and larger mesopores. The deviation between the two curves occurs around 25 nm pore radius which agrees well with literature values indicating that ionomer agglomerate size is about 40 nm diameter.[55] Furthermore, a large portion of the porosity, ~80%, is situated initially in macropores, and with the addition of ionomer the overall macroporosity decreases as well as the size of the macropores. The shift in pore size distribution with the addition of ionomer suggests that macropores are covered with an ionomer film, reducing the effective pore radius (film thickness ranging between 40 and 200 nm). Because ionomer thin films have been shown to have poor water uptake,[56-58] swelling of the ionomer phase is not considered in this model. The ionomer phase is considered at bulk density for the purposes of calculating volume fraction.

Table 2.1. Pore Size Distribution Fit

Parameter	Pore Mode	Pure Catalyst	Pellet (0.222 g_{cat}/cc)	Pellet (0.304 g_{cat}/cc)	Pellet (0.336 g_{cat}/cc)
Mean Radius/nm	1	4.57 ± 0.04	4.11 ± 0.03	4.08 ± 0.03	4.06 ± 0.02
	2	164.6 ± 8.3	98.6 ± 8.8	84.4 ± 17.5	51.9 ± 47.0
	3	307 ± 8	121.8 ± 2.4	113.3 ± 3.8	102.0 ± 3.5
Spread	1	0.222 ± 0.009	0.222 ± 0.008	0.225 ± 0.008	0.214 ± 0.007
	2	1.115 ± 0.035	1.097 ± 0.080	1.242 ± 0.140	1.943 ± 0.623
	3	0.320 ± 0.032	0.293 ± 0.026	0.416 ± 0.047	0.586 ± 0.046
Volume fraction	1	0.191 ± 0.033	0.266 ± 0.045	0.263 ± 0.093	0.261 ± 0.144
	2	0.656 ± 0.023	0.524 ± 0.033	0.451 ± 0.069	0.306 ± 0.109
	3	0.153 ± 0.022	0.210 ± 0.030	0.286 ± 0.063	0.433 ± 0.094

The various distributions are easily modeled by considering the porosity to be composed of three LNPSDs as shown in Figure 2.2. Each LNPSD, $V_j(r)$, can be represented as a function of a characteristic pore radius, r_j, spread, s_j, and fraction of total porosity, f_j:[42]

$$V_j(r) = f_j \left[\frac{1}{r s_j \sqrt{2\pi}} \exp \left(-\frac{1}{2} \frac{\ln r - \ln r_j}{s_j \sqrt{2}} \right)^2 \right] \qquad [3]$$

Saturation for each LNPSD, S_j, is calculated by integrating the PSD over the whole pore-radius range for the hydrophilic pore fraction (because $p_c > 0$) and for all pores greater than the critical radius for the hydrophobic pore fraction:[42]

$$S_{\mathrm{j}} = f_{\mathrm{HI,j}} + f_{\mathrm{HO,j}}[1 - erf(\frac{ln(r_{\mathrm{c}}) - ln(r_{\mathrm{j}})}{s_{\mathrm{j}}\sqrt{2}})] \quad [4]$$

where the saturation of the j^{th} LNPSD, S_j, is a function of the hydrophilic pore fraction, f_{HI}, and the hydrophobic pore fraction, f_{HO}. Here it is assumed that hydrophilicity and hydrophobicity is uniformly distributed over all pore sizes and throughout the catalyst layer. The hydrophobic pore fraction, $f_{HO,}$ is fitted to experiment. The hydrophilic pore fraction, f_{HI}, can then be calculated from $f_{HI} = 1 - f_{HO}$. The overall saturation is the sum of the contributions of all LNPSDs, $S = \sum S_j$.

Saturation impacts transport parameters via the permeability, k_L, and a reduction in effective diffusivity. In the liquid phase, an expression used by Weber et al accounts for tortuosity as well as weighting of pore sizes according to Poiseuille flow. In this case liquid permeability relative to saturated conditions, $k_{rel,HO}$, is calculated for hydrophobic pores:[42,52]

$$k_{\mathrm{rel,HO}} = \frac{S^2}{2} \sum_{\mathrm{j}} f_{\mathrm{j}}[1 - erf(\frac{ln(r_{\mathrm{c}}) - ln(r_{\mathrm{j}})}{s_{\mathrm{j}}\sqrt{2}} - s_{\mathrm{j}}\sqrt{2})] \quad [5]$$

where the relative liquid permeability can be represented as a function of saturation, S; the critical radius, r_c; the contribution of each pore distribution to the total porosity, f_j; characteristic pore radius, r_j; and spread, s_j. The actual liquid permeability, k_L, is calculated by volume averaging the conditions in hydrophobic and saturated hydrophilic pores:[42,52]

$$k_{\mathrm{L}} = k_{\mathrm{L,sat}}(f_{\mathrm{HO}}k_{\mathrm{rel,HO}} + f_{\mathrm{HI}}) \quad [5]$$

where the liquid permeability is a function of the saturated permeability, $k_{L,sat}$.

In the gas phase, the governing mass balance on the various constituents is coupled with Stefan-Maxwell multicomponent diffusion:[42,59]

$$\nabla x_{\mathrm{i}} = \sum_{\mathrm{i} \neq \mathrm{j}} \frac{N_{\mathrm{i}}x_{\mathrm{j}} - N_{\mathrm{j}}x_{\mathrm{i}}}{cD_{\mathrm{ij,eff}}} \quad [6]$$

where x_i represents mole fraction, N_i is the flux, c the total molar concentration, and $D_{ij,eff}$ a binary diffusion coefficient. This diffusion coefficient is an effective value due to the impact of porosity on the mean free path of constituents:[45,53,54]

$$D_{\mathrm{ij,eff}} = D_{\mathrm{ij}}(\epsilon(1 - S))^{3/2} \quad [7]$$

where the diffusivity, D_{ij}, is modified by the porosity (ε) and saturation (S from Eq.4). The diffusivity is also modified to account for Knudsen diffusion. Knudsen diffusion limits diffusivity in small pores where wall effects dominate. In order to incorporate the impact of Knudsen diffusion, a mean open pore radius is calculated. This mean open pore radius, r_K is used to calculate Knudsen diffusivity, D_K:[52,54]

$$D_{\mathrm{K,i}} = \frac{2r_{\mathrm{K}}}{3}\left(\frac{8RT}{\pi M_{\mathrm{i}}}\right)^{1/2} \quad [8]$$

where R is the ideal gas constant, T is the temperature, and M is the molar mass of the gas molecule. Contributions of the two diffusion modes can be combined via the Bosanquet equation:[60-63]

$$\frac{1}{D_{\mathrm{ij}}} = \frac{1}{D_{\mathrm{K,i}}} + \frac{1}{D_{\mathrm{M,ij}}} \qquad [9]$$

where the diffusivity, D_{ij}, is a function of Knudsen diffusivity, $D_{\mathrm{K,i}}$, and molecular diffusivity, $D_{\mathrm{M,ij}}$. This diffusivity is the value used in calculating effective diffusivity via Equation 7.

Darcy's Law governs liquid phase transport where liquid flux is proportional to the liquid pressure gradient: [52,54]

$$N_{\mathrm{L}} = -\frac{k_{\mathrm{L}}}{\mu}\nabla P_{\mathrm{L}} \qquad [10]$$

where N_{L} is the flux of liquid water, k_{L} is the effective permeability (a function of saturation, Eq. 5 and 5), μ is the viscosity of water, and ∇P_{L} is the liquid pressure gradient.

Although the GDL used in the present work (Sigracet 25BC) has a microporous layer (MPL) which might require the model to have three regions, this work will consider the GDL as a single region, because the combination of high hydrophobicity and no ORR causes the various transport processes to be mutually independent. As such the composite transport resistances in each phase are the weighted average of the MPL and remaining GDL resistances. Furthermore, the GDL properties obtained from the literature were composite GDL values.[64-66]

Conductive Phase. Two different conductive phases exist: solid electronic (*s*) and electrolyte (*e*) conductor. Here, Ohm's Law governs charge transport:[59]

$$i_{\mathrm{i}} = -\kappa_{\mathrm{i}} \nabla V_{\mathrm{i}} \; ; \; i_{\mathrm{e}} = -\kappa_{\mathrm{e}} \nabla V_{\mathrm{e}} \qquad [11]$$

where, for a given phase (i or e), the current density, *i*, is a function conductivity, *κ*, and potential, *V*.

Electronic conductivity was calculated from correlating high frequency resistance (HFR) with the thickness of MEAs of varying loading. This correlation, shown in Figure 2.3, assumes that ionic conductivity in the catalyst layer is much lower than electronic conductivity. Essentially, at high frequencies capacitors behave like short circuits eliminating the effect of transport and kinetic effects on the impedance. Without these effects the HFR is the ohmic resistance of the system. In the catalyst layer, the solid and electrolyte systems are in parallel making the HFR (R_{HFR}):

$$R_{\mathrm{HFR}} = R_{\mathrm{sys}} + \frac{R_{\mathrm{i}}R_{\mathrm{e}}}{R_{\mathrm{i}} + R_{\mathrm{e}}} \qquad [12]$$

where the HFR is function of the resistances of the electronic (R_{e}) and ionic phases (R_{i}) as well as the resistance of the remainder of the system (R_{sys}). When $R_{\mathrm{i}} >> R_{\mathrm{e}}$, the right hand side of Eq. 12 simplifies to $R_{\mathrm{HFR}} = R_{\mathrm{sys}} + R_{\mathrm{e}}$. By comparing HFR to the electrolyte resistance calculated in the next section we can confirm this assumption that $R_{\mathrm{i}} >> R_{\mathrm{e}}$. This intercept includes contact resistance between the CL and GDL, and contact resistance is therefore included in the sensitivity study presented below. The slope of the HFR with respect to catalyst layer thickness represents the electronic conductivity of the catalyst layer. From

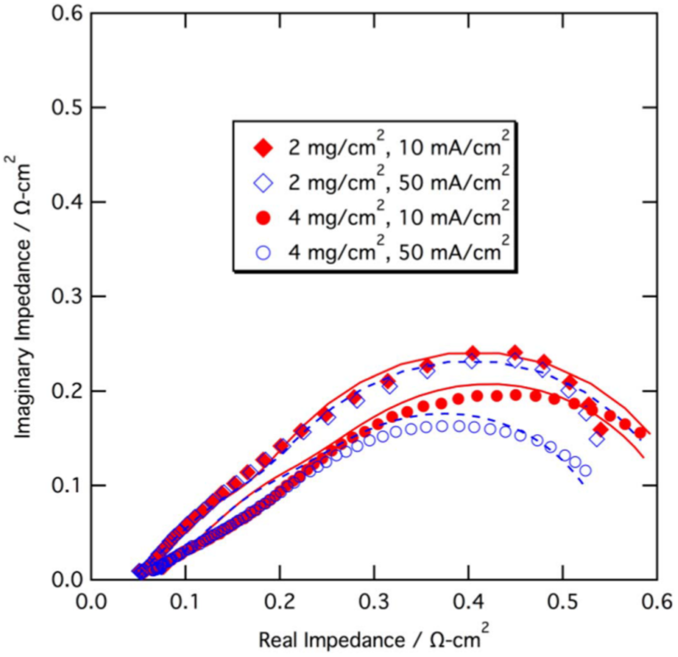

Figure 2.4. Impedance spectra of MEA with two different loadings at two different current densities.

Table 2.2. Impedance Fit Parameters.

Loading / mg cm^{-2}	Current / A cm^{-2}	Electrolyte Resistance (R_i)/Ω cm^2	Charge Transfer Resistance (R_CT)/Ω cm^2	Capacitance (C_CT) / mF cm^{-2}	External Resistance (R_ext)/Ω cm^2
2	0.01	0.434 ± 0.066	0.468 ± 0.029	126 ± 18	0.045 ± 0.003
2	0.05	0.466 ± 0.074	0.447 ± 0.029	131 ± 20	0.044 ± 0.003
4	0.01	0.580 ± 0.165	0.385 ± 0.046	151 ± 44	0.070 ± 0.005
4	0.05	0.544 ± 0.166	0.322 ± 0.044	153 ± 48	0.068 ± 0.005

this correlation two model parameters can be found: the electronic conductivity, κ_e= 0.62 ± 0.38 S/cm and the resistance of the remainder of the system (contact resistance, etc.) R_sys= 0.046 ± 0.010 Ω-cm^2. While the error on the conductivity is quite large, we consider this a reasonable estimate for our purposes.

Electrolyte conductivity was calculated from electrochemical impedance spectroscopy. Makharia et al[67] and Eikerling et al[68] show that impedance of catalyst layers can be well modeled by transmission line circuits. Specifically, when the electrode potential is small and the electronic and mass transfer resistance in the catalyst layer is insignificant, the impedance, Z, can be modeled by the expression: [52,67,68]

$$Z = R_\mathrm{ext} + \sqrt{R_\mathrm{i} Z_\mathrm{CT}} coth(\sqrt{R_\mathrm{i}/Z_\mathrm{CT}}) \qquad [13]$$

where R_ext is the resistance external to the catalyst layer, ω is frequency, R_i is the ionic resistance in the catalyst layer, and Z_CT is a charge transfer impedance. This charge transfer impedance is ostensibly a Voigt element, where the impedance is a function of some charge transfer resistance, R_CT, and a capacitance, C_CT:

$$Z_\mathrm{CT} = \frac{R_\mathrm{CT}}{1 + j\omega R_\mathrm{CT} C_\mathrm{CT}} \qquad [14]$$

Figure 2.4 shows impedance spectra of two loadings at two different current densities that are all well below the onset of mass transport limitations; lines represent the fit by the transmission line model, Eq. 13. The fit at 4 mg cm^{-2} loading is not ideal because the initial slope is 30° and should be 45° according to Eq. 20. A non-45° phase angle can be caused by a number of phenomenon including varying ionic resistance in the catalyst layer[69] and multi-scale porosity causing fractal Gerischer-like impedance.[70,71] Due to these concerns, and to confirm that experimental conditions satisfy model assumptions, conductivity was also calculated by fitting to experimental data. The fit with and without fixed ionic conductivity is discussed later in the results section.

From the fitted ionic resistance, R_i, an effective ionic conductivity for the catalyst layer was calculated to be K_i= 0.0181 ± 0.0049 S/cm based on the thickness of the catalyst layer. A comparison of this ionic conductivity with the electronic conductivity (κ_e= 0.62 ± 0.38 S/cm) calculated in the previous paragraph confirms the assumption that $\kappa_\mathrm{i} << \kappa_\mathrm{e}$ (or $R_\mathrm{i} >> R_\mathrm{e}$).

Generation Terms. The generation terms for oxygen reduction and evaporation are treated as first order reaction rates. Oxygen reduction is expressed in a symmetrical Butler-Volmer form, in which the forward reaction (oxygen reduction) is first order with respect to the local partial pressure of oxygen:[54,72]

$$r_\mathrm{ORR} = \frac{i_{0,\mathrm{eff}}}{nF}\left[p_\mathrm{o} \exp\left(\frac{\alpha F \eta}{RT}\right) - \exp\left(\frac{-(1-\alpha)F\eta}{RT}\right)\right] \qquad [15]$$

$$\eta = U_0 - V_0 - V_\mathrm{i} - V_\mathrm{e} \qquad [16]$$

where p_o is the partial pressure of oxygen, η is the over-potential, and α the transfer coefficient. The over-potential, η, is a function of U_0, the reversible potential; V_0, the electrode polarization (an independent variable); V_s, the ionic phase potential; and V_e, the electronic potential. The effective pre-exponential exchange current density, $i_{0,\mathrm{eff}}$, is considered to be a function of porosity, saturation, and ionomer volume fraction due to the requirement that protons, electrons, and oxygen have access to catalytic active sites. To incorporate the impact of these phases, the exchange current density is modeled as a three-phase effective parameter:[53]

$$i_{0,\mathrm{eff}} = i_0 f_\mathrm{i} f_\mathrm{s} \epsilon (1 - S) \qquad [17]$$

where f_i is the volume fraction of ionomer and represents the probability that protons are available at any given differential volume element. The ionomer volume is calculated based on the ionomer content and density. The volume fraction of solid catalyst, f_s, represents the probability that a given volume element has connectivity with the electronic phase. The solid catalyst volume is calculated by subtracting porosity as measured by porosimetry and ionomer volume from the volume of the pellets used for porosimetry experiments. The porosity, ε, is calculated for a given catalyst layer specific volume by subtracting solid catalyst volume and ionomer volume. The expression ε (1-S) represents the volume fraction of oxygen-accessible open pores. In the expression above, $f_\mathrm{s}\varepsilon$ can also be interpreted as an area per unit volume that is dependent on the quantity of porous and solid phases. Because the total volume fractions must equal one ($1 = f_\mathrm{s} + f_\mathrm{i} + \varepsilon$), an increase in one of these volume fractions necessitates a decrease in the remaining volume fraction.

The evaporation term, r_evap, is dependent on water vapor pressure and the partial pressure of water: [52,54]

$$r_\mathrm{evap} = k_\mathrm{m} a_\mathrm{T} (P_\mathrm{vap} - p_\mathrm{w}) \qquad [18]$$

where k_m is a mass-transfer coefficient, a_T the area per unit volume, P_vap, the vapor pressure of water, and p_w the partial pressure of water vapor. Because the reaction is fast and at equilibrium,[52,73] the rate can be thought of as the necessary evaporation necessary to keep the vapor pressure and water partial pressure equal.

Model Implementation. The model was written with MATLAB using the boundary value solver BVP5C. The boundary value solver generated the mesh density necessary to achieve 0.1% error for residuals above the threshold value 10^{-6}. Generally, the number of points was on the order to 20 in low-current regimes and 200 in high current regimes. A nonlinear, least-squares fitting function was used to fit the following parameters: hydrophobic pore fraction, f_HO; saturated liquid permeability, k_w; exchange current density, i_0; reversible potential, U; and exchange coefficient, α. The parameters were fitted simultaneously to polarization data at four different air pressures and nine potentials in the range 0.82 to 0.30 volts. Parameters were fit to a tolerance of 0.1%. The current density was calculated as the electronic current at the channel.

Sensitivity was calculated by running the model at a fixed step size of 1% for a given parameter. The change in current density, Δi, due to a change, Δx, in the value of a parameter x, leads to the sensitivity, B_x:

$$B_x = \frac{\Delta i / i}{\Delta x / x} \qquad [19]$$

A positive sensitivity indicates a correlation between current and the parameter of interest, whereas a negative value indicates anti-correlation. No correlation is indicated by a sensitivity of zero.

The model was used to fit MEA data obtained at three different backpressures: 2, 12, and 30 $\mathrm{psi_g}$. These pressures correspond to partial air pressures: 0.5, 1.2, and 2.4 atm respectively correcting for altitude in Albuquerque, NM (P_atm=0.83 bar)[74] and experimental conditions. Catalyst loadings of 2, 3, and 4 mg/cm^2 were studied. Five parameters were fit: hydrophobic pore fraction, f_HO; saturated liquid permeability, k_w; exchange current density, i_0; reversible potential, U_0 and transfer coefficient, α. The fitted parameters are shown in Table 2.3.

If a turnover number of 1 e^- site^{-1} s^{-1} is assumed, based on estimates by Gasteiger et al,[41] we calculate an active site concentration of ~2 mmol cm^{-3}. This is a very rough approximation considering that estimates of turnover number range from 0.023 to 25 e^- site^{-1} s^{-1}, but is comparable to a value of 0.5 mmol cm^{-3} estimated for 47% Pt/C.[41]

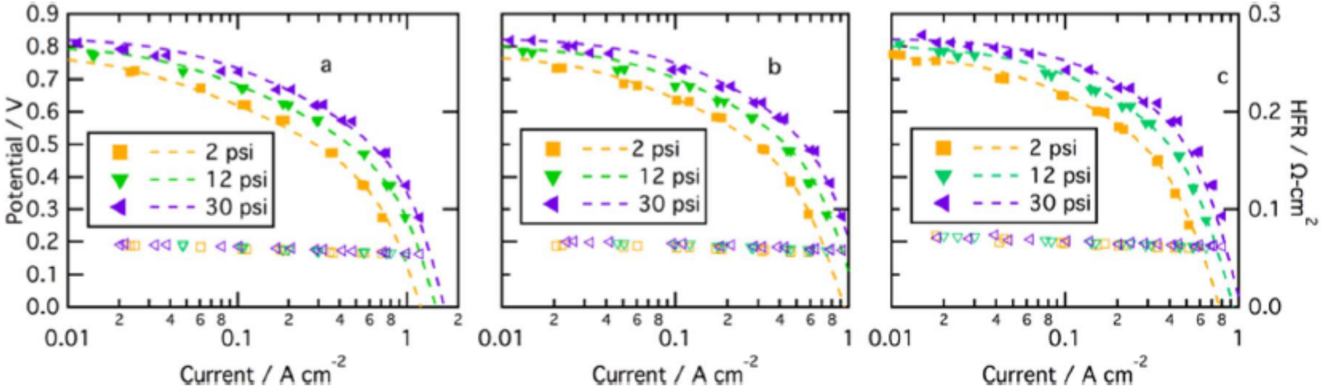

Figure 2.5. Comparison of experimental and model results at three different gas pressures for (a) 2 mg/cm2, (b) 3 mg/cm^2, and (c) 4 mg/cm^2. Conditions: Temp. 80 C, 25BC GDL, 4mg/cm^2 Catalyst Loading, 45 wt% Nafion, Cell Area: 5cm^2 membrane: NR211.

A plot of experimental polarization curves along with the fitted model is shown in Figure 2.5. From observation, the model fits the data well with regards to the shape of the curves. The model fit shown in Figure 2.5 can be further validated by comparing fitted values with expected values. The exchange coefficient, α is 0.407 ± 0.009 which is in the range of typical values (0.3-0.7).[72] The exchange current density is large because it represents a theoretical value as if all points in the electrode were on a triple-phase boundary. This is not possible for materials of finite thickness, so it is best to consider the effective exchange current density (Eq. 17) for comparison purposes. The effective exchange current densities are 28, 42, and 56 mA/cm^2 at 30 psi for 2, 3, and 4 mg/cm^2 loadings respectively. These values correspond well with the current density at which the experimental polarization curves deviate from the Tafel regime in the upper part of Figure 2.5.

The fitted permeability of $(5.27 \pm 2.58)\times10^{-13}$ agrees well with the value predicted by the Kozeny-Carmen Equation (4×10^{-13}).[75] The hydrophobic pore fraction was found to be 0.287 ± 0.110. Based on the assumption that all hydrophobicity is due to the ionomer, this number can be compared to the electrolyte solid fraction in the catalyst layer, 0.193 ± 0.070. The agreement between these values corroborates the theory that the majority of the hydrophobicity is due to the ionomer.

As mentioned in the Model Section, the model was also fitted to experiment using ionic conductivity as a fitting parameter. The results of this fit showed statistical agreement with the previous fit (Table 2.3) and the fitted conductivity (0.0195 ± 0.0025 S/cm) agrees well with the value from the impedance data (0.0181 ± 0.0049 S/cm). This agreement may be considered as validation of the model and the calculated value of effective ionic conductivity. A detailed physicochemical description of ionomer properties lies beyond the scope of this work and is strongly dependent on experimental conditions such as confinement,[56-58,76] humidity,[57,77] substrate,[58,77] and processing.[58,78]

Now that the fit has been established, profiles in the catalyst layer can be used to better understand transport phenomena. Figure 2.6 shows electronic current profiles (a), oxygen vapor fraction profiles (b), and flooding (c) in the catalyst layer at three different potentials. How these potentials correspond to the polarization curve is shown in Figure 2.6d: points I, II, and III correspond to potentials in the kinetically limited regime, ohmic limited regime, and catalyst layer oxygen transport limited regime respectively. Point I shows the most uniform current distribution (Figure 2.6a), reflecting kinetically-limited ORR in the absence of O_2 concentration gradients (Figure

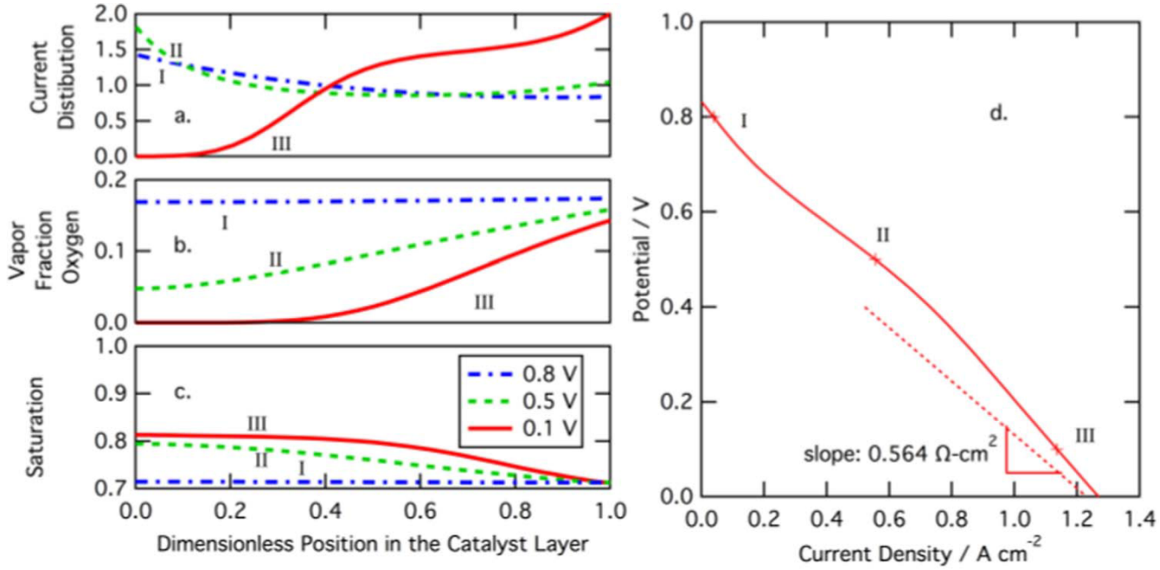

Figure 6. (a) Solid phase current, (b) ionic over-potential, and (c) flooding at dimensionless positions in the catalyst layer at three different potentials on the polarization curve (d) showing I, kinetic limitations; II, electrolyte conductivity limitations; and III, oxygen diffusion limitations. For position in the catalyst layer, zero represents the membrane interface and one represents GDL interface.

2.6b). Point II shows an ohmically-limited current profile, in which ohmic resistance in the catalyst layer electrolyte causes most of the ORR to occur near the membrane-CL interface, where a steep current gradient is observed. Continuing to lower potentials, in Figure 2.6b, point III shows conditions where the catalyst layer closest to the membrane has been completely exhausted of oxygen. Oxygen depletion makes those sections inert, and the current profile is flat and zero as shown in Figure 2.6a between 0 and 0.1. The limiting case (not shown) is where the catalyst layer is almost entirely oxygen starved and all the ORR occurs at the CL-GDL interface. At this extreme, the polarization becomes linear due to the ionic resistance of the catalyst layer.

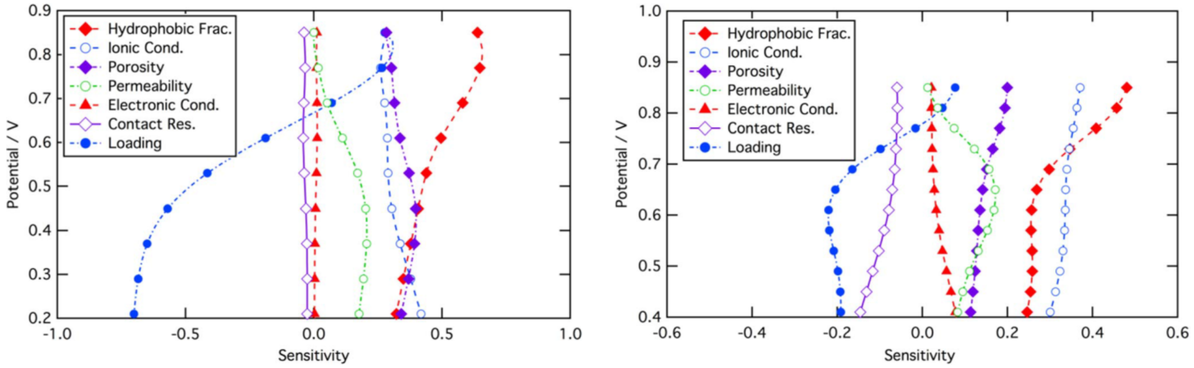

Figure 2.7. Plot of current sensitivity in air (left) and oxygen (right)varying with potential.

A sensitivity study of performance in air is shown in Figure 2.7. Sensitivity is defined as a ratio of relative change in performance (current) to relative change in a given parameter. Figure 2.7 shows sensitivity as it varies with potential (on the *y*-axis). At all potentials hydrophobic pore volume shows high sensitivity, this indicates that flooding is high. Essentially, flooding limits electrochemically active surface area at high potentials (kinetically limited, I) and limits oxygen diffusion at low potentials (oxygen transport limited, III). Around 0.6 V there is a dip in the hydrophobic pore fraction sensitivity. This dip correlates to an increase in electrolyte conductivity sensitivity. This confirms the ohmic limited regions identified by point II in Figure 2.6. The significant anti-correlation is loading: at high potentials increased loading means increased electrochemically active surface area, but at low potentials this increased loading only inhibits oxygen diffusion, leading to lowered utilization and reduced performance.

A sensitivity study can also be calculated for oxygen, as shown in Figure 2.7 right. The sensitivity in oxygen is similar to air at high potentials, but not at low potentials. The similarity in sensitivity is expected at high potentials due to kinetic limitation. Once outside of this regime, the similarities decrease substantially due to the lack of transport limitations in oxygen. In this ohmically-limited regime flooding only impacts electrochemically active surface area causing the hydrophobic pore fraction sensitivity to decrease as kinetics become less limiting at lower potentials. In oxygen, electron transport limits current density at low potentials. This is shown by the increase in ionic conductivity sensitivity around 0.8 V. At low potentials activity reaches a mixed domination region. In this region performance is equally controlled by hydrophobic porosity, ionic conductivity, and kinetic parameters. Essentially the current profile is similar to point II in Figure 2.6a, but as the potential decreases further the current distribution becomes increasingly concentrated at the CL-membrane interface due to ionic conductivity limitations. As the current distribution becomes more concentrated at that interface, less charge is conducted through the catalyst layer electrolyte, which decreases the ionic conductivity sensitivity. External ohmic losses also become more significant at low potentials. This value is not a fitted parameter, but it does include contact resistance between the CL and GDL due to the high Nafion content in the CL. For this reason, external resistance was added to the oxygen sensitivity study (purple line with open diamonds) and represents the impact of contact resistance between assembly layers.

To return to air sensitivity, two recommendations can be made for future non-PGM catalysts and their application in fuel cells. Loading should be optimized with current density at key operating potentials in mind. For applications running at max power, lower loadings are desired to increase performance in the 0.6-0.4 V range. A second observation that can be gleaned from the air sensitivity is that increasing ionomer content near the CL-membrane interface could mitigate ohmic losses resulting from poor catalyst utilization at low potentials, as previously observed by other workers for platinum based catalyst layers.[79,80] This would be the result of optimizing catalyst ink for different depths in the catalyst layer, and the catalyst layer close to the GDL would be optimized for oxygen diffusion, while the catalyst layer close to the membrane would be optimized for electrolyte conductivity.

Finally, optimization studies were conducted for loading and catalyst layer density. For each parameter, the value was obtained that provided maximum current density with all other parameters at baseline values (Table 2.3). From Figure 2.8a, it is apparent that optimal loading changes with potential, because mass transport limitations are more significant at low potential and kinetic limitations more significant at high potential. CL density represents how compressed the catalyst layer is during MEA construction and the optimal value does not vary much with potential as shown in contour plots Figure 2.8c and 2.8d.

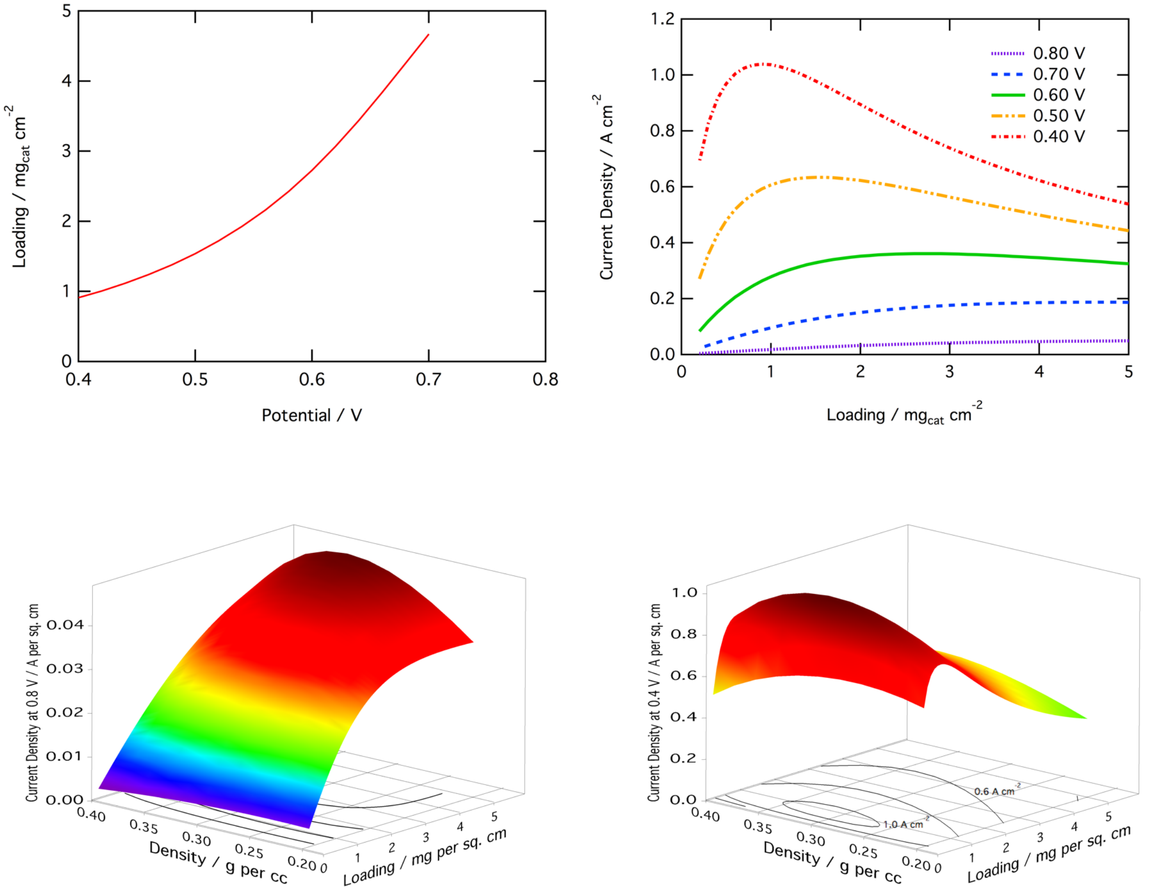

Figure 2.8. (a) Optimal loading as it varies with potential, (b) current as it varies with loading at various potentials, (c) current as it varies with density and loading at 0.8 V, and (d) current as it varies with density and loading at 0.4 V. Conditions: 30 psi, Temp. 80 C, 25BC GDL, 45 wt.% Nafion, Cell Area: 5cm^2, membrane: NR211.

In conclusion, a one-dimensional, steady-state model was developed for electrode-scale transport in a non-PGM PEMFC cathode. It was found that flooding limits oxygen transport in air due to reduced effective porosity and active surface area. At low potentials the flooding limitations result in poor catalyst utilization and increased ohmic losses. In contrast to air performance, oxygen performance depends primarily on active surface area and electron conductivity. The difference in sensitivity between air and oxygen performance suggests that oxygen MEA performance is not an effective indicator for non-PGM catalysts.

Finally, cathodes can be designed for improved air performance by improving catalyst utilization. Utilization can be improved in two different ways. Most simply, utilization can be increase by decreasing loading. Although this model predicts improved performance with decreased loading, it is important to note that as catalyst thickness decreases, the relative importance of interfacial effects between CL and GDL will increase. Utilization can also be improved by optimizing sections of the catalyst layer for different phenomena. Optimization would include improving gas diffusion near the GDL and improving ionic conductivity near the membrane.

Task 3/7. Fuel Cell Testing and Initial Durability Measurements

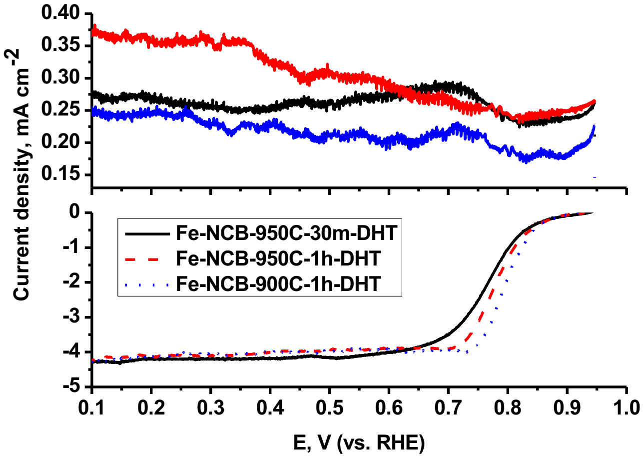

Figure 3.1 RRDE data for Fe-CTS catalysts heat treated at different conditions: T=950°C t=30min (black), T=850°C t=1h (red) and T=900°C t=1h (dashed) second heat treatment T=950°C t=30min, NH_3. Conditions: 0.5M H_2SO_4 saturated with O_2, 1200RPM, 5 mVs^{-1}, catalyst loading 0.6 mg cm^{-2}.

We have optimized the heat-time trajectory (total heat integral accumulated by the sample during pyrolysis) and have discovered that Fe-CTS heat treated at T=900°C for 1 hour has the highest activity (Figure 3.1). The value of $E_{1/2}$ =0.8V is significantly higher than for many other non-PGM catalysts tested under the same conditions. After optimization, we have synthesized a large batch (~5 g) of Fe-CTS catalyst. This batch was tested at Nissan Technical Center North America in order to validate the high performance and durability of this promising catalyst under automotive performance and durability cycling that simulate actual stack conditions.

RDE measurements at Nissan of the large batch catalyst sample revealed a high kinetic current density at 0.8V of i_k = 4.6 mA cm^{-2} with a Tafel slope of 52 mV/decade. The Fe-CTS sample also showed an active reduction peak at around 0.75V, which might be associated with the active site of the catalyst. The durability of the catalyst was evaluated using the DOE Durability Working Group (DWG) proposed protocol and Nissan load-cycling protocol (Figure 3.2). Under both durability tests, the catalyst presented an $E_{1/2}$ drop of only 3-4% from the initial value, indicating excellent durability.

Rotating disk electrode (RDE) measurements at Nissan of a large laboratory batch of the catalyst revealed a high kinetic current density at 0.8V of i_k=4.6 $mAcm^{-2}$ with a Tafel slope of 52mV/decade (Figure 3.1). The durability of the catalyst was evaluated using the DOE Durability Working Group (DWG) proposed protocol and Nissan load-cycling protocol (see Figure 3.2). Under both durability tests, the catalyst presented a drop of the half-wave potential of only 3–4% relative to the initial value, which prompted us to further evaluate it in an automotive-type MEA.

RDE testing is a powerful tool for measuring catalyst activity, but MEA testing in an operating fuel cell provides a realistic evaluation of performance of the catalyst in the full MEA configuration. MEAs were fabricated and evaluated at Nissan Technical Center North America. Figure 3.3 shows the MEA performance of the Fe-CTS catalyst under the recommended DOE conditions of H_2/O_2 operation, 100%RH, and 1 bar O_2

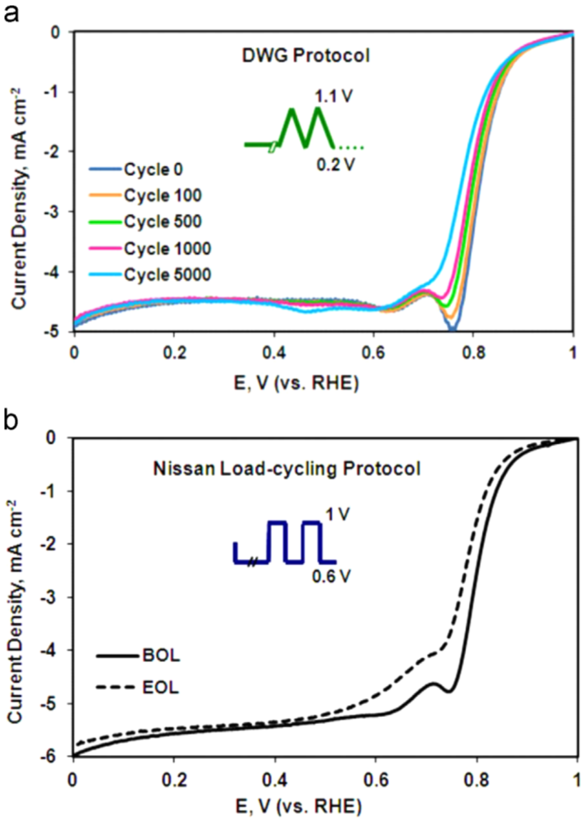

Figure 3.2 Durability in RDE tests under (A) DWG: 900 RPM and (B) Nissan load-cycling protocols: 1600 RPM. Both in 0.5 M H_2SO_4 saturated with (A) O_2 and (B) N_2.

partial pressure (1.5 bar total pressure or 0.5 bar_g backpressure). Three MEAs with the same catalyst loading of 4 mg/cm^2, but different Nafion content, were investigated. The open circuit voltage (OCV) was 0.92V and did not change with increasing Nafion content. Figure 3.3A shows that increasing the ionomer content from 35% to 55% significantly changes the iV performance. The poor iV performance of the 35wt% Nafion MEA may be attributed to incomplete Nafion coverage of the non-PGM active sites. Better ionomer coverage was achieved upon increasing the Nafion content to 45% and 55% as supported by the significant improvement in the iV curve. Increasing the ionomer content from 45% to 55% resulted in further increased kinetic currents. As shown in Figure 3.3B, the MEA containing the Fe-NCB catalyst with 55% Nafion gave kinetic current of 100 mA cm^{-2} at 0.8 $V_{iR\text{-}free}$. This is the first report of a fuel cell performance that meets the current DOE design target for non-PGM cathode PEMFC catalysts for potential future automotive applications. The reproducibility of the high current densities obtained with this catalyst is confirmed by the overlapping Tafel plots. This is the first report of a non-PGM catalyst achieving such high current density values at $0.8V_{iR\text{-}free}$ using Nafion NRE 211 membrane, a significantly thinner membrane than Nafion 115 or Nafion 117, which is typically used by other research groups working on non-PGM catalysts. [81]

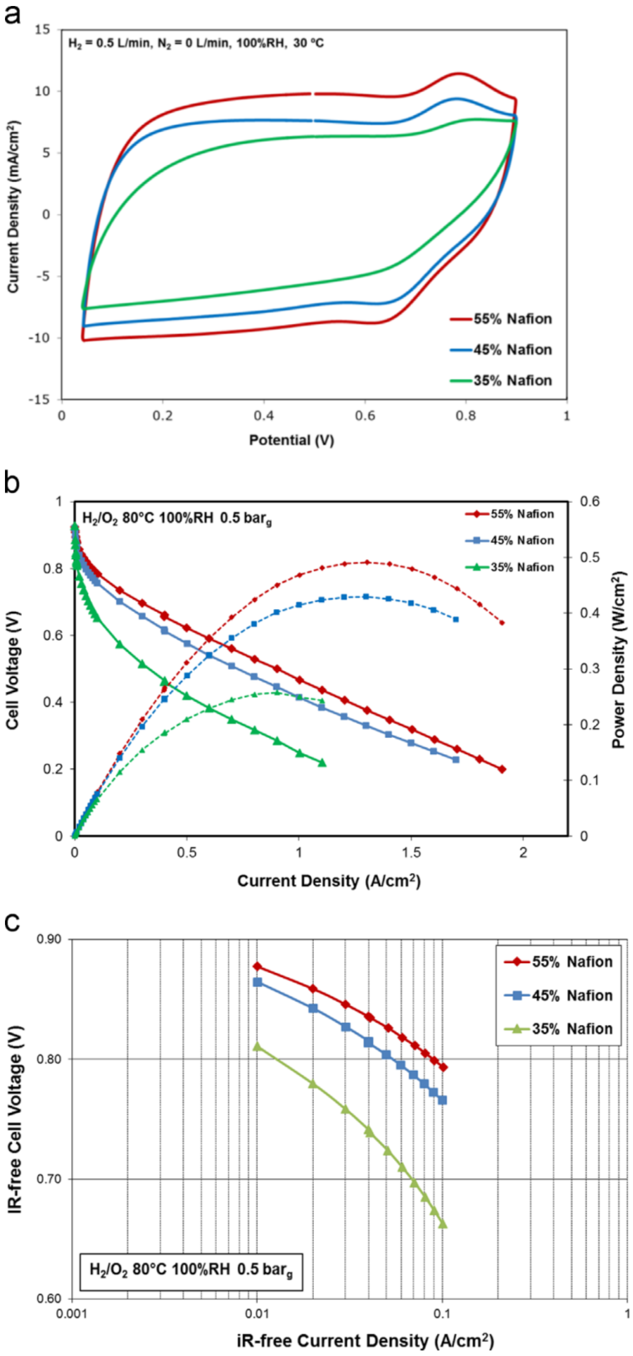

Figure 3.3 CV (a), MEA performance (b) and kinetic current density (c) of the Fe-CTS catalyst with varying Nafion content. Conditions: T_{cell}=80 °C, 100% RH,0.5 bar back pressure; anode catalyst: Johnson Matthey Fuel Cell (JMFC) 0.4mg_{Pt}/cm^2, an NRE 211 membrane,and cathode Fe-CTS-based catalysts loading of 4$mg_{catalyst}/cm^2$.

We have also evaluated the durability of the Fe-CTS catalyst using automotive accelerated stress tests (AST), which simulate the actual stack conditions under FECV operating conditions. The catalyst showed excellent durability under the Nissan load cycling protocol (for protocol details, see discussions above) with polarization performance undergoing minimal change after 10,000 potential cycles (shown in Figure 3.4 for the 45% Nafion sample). All MEAs that were tested under the load cycling protocol showed the same durability regardless of Nafion content. The difference in the beginning of life (BoL) iV curve in Figure 3.4 and the corresponding curve in Figure 4 for the 45% Nafion MEA are attributed to variations between MEAs. Substantial performance losses, however, were observed for the Fe-CTS catalyst after undergoing Nissan's highly stringent start-stop AST (Figure 3.2), but this drastic performance loss is also observed for conventional platinum supported on high surface area carbon catalysts. The similar behaviour of platinum supported on carbon and non-PGM M-N-C catalysts under start-stop test conditions (polarization above 1.23V) is related to intrinsic thermodynamic carbon corrosion. It should be noted that this is the first report on the evaluation of a non-PGM catalyst under AST protocols designed by automotive manufacturers. Materials and system approaches should be explored to improve start-stop durability of carbon-containing catalysts.

To summarize, this work is the first report of M-N-C catalysts derived from the pyrolysis of nitrogen containing charge-transfer precursors and using the sacrificial support method to obtain open-frame structure. High kinetic current densities and overall performance was observed in both RDE and MEA tests. The Fe-NCB catalyst was found to be extremely durable under different independent test protocols, which simulate actual vehicle driving conditions, including that recommended by US Department of Energy Durability Working Group and Nissan's load cycling protocol. The high performance and excellent durability was independently validated at Nissan North America's Fuel Cell and Battery Laboratory.

Unprecedented high performance and durability may be related to successful formation of large amounts of FeN_xC_y sites, which are active towards oxygen reduction, and uniform open area morphology with hierarchy of pores in which these active centers are homogeneously distributed and easily accessed by reactants. Water management is also optimized through such unique morphology obtained by SSM.

The durability evaluation was also conducted on the MOF-based catalysts develop at NEU, which is highly active toward ORR as shown above. Membrane electrode assemblies (MEAs) for fuel cell testing were prepared using FePhen@MOF-$ArNH_3$ cathode on Gas Diffusion Layer (Sigracet BC25 GDL), Pt/C (Tanaka, 46%) anodes on GDL (Sigracet BC25), Nafion 5wt% ionomer solution, and Nafion 211 ionomer membrane. To prepare the cathode, a catalyst ink composed of FePhen@MOF-$ArNH_3$ dispersed in a water-alcohol mixture with the requisite amount of ionomer (Nafion 5wt%) was sprayed on gas diffusion layer (Sigracet, BC25). Cathode loading consisted of 0.2 mg/cm^2 with an ionomer content of 60% by weight of the catalyst. After drying the cathodes, a layer of interfacial ionomer was sprayed to achieve a loading of $0.4mg_{Nafion}/cm^2$. Anodes were prepared with commercial Pt/C (Tanka, 46%) in the same manner as the cathode and served as the reference, reversible hydrogen electrode (RHE). Hot pressing of the electrodes together with a Nafion 211 membrane was carried out at 130 °C and 1,000 lbs. for duration of 5 minutes. MEAs were then assembled in a fuel cell consisting of 5 cm^2 serpentine flow fields. Humidification of the MEA was performed for 60 minutes by flowing N_2 (100% RH) at a cell temperature of 80 °C. The operating temperature of the fuel cell was 80 °C and the cell was activated with H_2/O_2 (inlet temperatures 85 °C, 100% RH, 22 psi back pressure). Load cycling followed a protocol from Nissan Technical Center North America (NTCNA) designed to simulate accelerated drive cycle conditions based on transitions between open circuit voltage and idling in automobile operation. Durability was tested at 80 °C with N_2 flowing on the cathode while stepping potential from 0.6 to 1.0 V *vs* RHE with 3s hold at each potential step. ORR durability cycling followed a protocol from Department of Energy's Durability Working Group (DOE-DWG) designed to evaluate the electrocatalyst durability mechanistically. Durability was tested at 80 °C with O_2 flowing on the cathode while cycling potential from 0.2 to 1.1 V *vs* RHE at 50 mV/s, each cycle lasting approximately 43 s.

Perchloric acid electrolyte (0.1 M) was prepared using double-distilled 70% perchloric acid (GFS Chemicals). Electrochemical measurements were carried out on glassy carbon (GC) disk (5.61 mm diameter, Pine Instruments) that was polished with 0.05-micron alumina paste (Buehler, Lake Bluff, IL) and then sonicated in distilled water and Isopropyl alcohol. The gold ring electrode was held at 1.3 V *vs* RHE to detect stable peroxide intermediate. Catalysts inks were prepared by dispersing the catalyst in a volume of 1:1 Millipore water:isopropyl alcohol with 10 vol% of 5 wt% Nafion® as a binder. The ink solution was then sonicated approximately 60 minutes to get a uniform suspension. A small volume of the catalyst ink was deposited on the GC substrate to obtain a non-PGM loading of approximately 600 μg/cm^2. All electrochemical measurements were carried out at room temperature (RT, 20-25 °C) in a standard electrochemical cell (Chemglass) with a 0.1 M perchloric acid ($HClO_4$) electrolyte using a rotating disk electrode (RDE) setup from Pine Instrument Company connected to an Autolab bipotentiostat (PGSTAT302N). Cyclic voltammetry (CV) was run on non-PGM catalysts in 0.1 M $HClO_4$ bubbled with argon. ORR was investigated by the RDE technique after bubbling oxygen in the electrolyte solution followed with rotations at 100, 400, 900, 1600 and 2500 rpm. Scans were recorded at 20 mV/s and all potentials are referenced to a RHE scale made from the same solution as the electrolyte. ORR durability cycling followed a similar protocol from the DOE-WG fuel cell evaluation designed to evaluate the electrocatalyst durability mechanistically. Durability was tested at RT in O_2 saturated 0.1 M $HClO_4$ electrolyte while cycling potential from 0.2 to 1.1 V *vs* RHE at 50 mV/s and 900 rpm for 6,200 cycles. ORR performance measurements were collected at RT in O_2 saturated 0.1 M $HClO_4$ electrolyte while cycling potential 0.05 to 1.2 V *vs* RHE at 20 mV/s and 1600 rpm after certain number of ORR durability cycles. Hydrogen peroxide cycling protocol was designed to address any issues related to (a) unstable exposed Fe and (b) stability of the carbon nitride structure, both being very sensitive to the presence of relatively high concentration of peroxide. The catalyst durability was tested at RT in argon saturated 0.5 M H_2SO_4 electrolyte, with and without 70 mM H_2O_2, while cycling potential 0.05 to 1.2 V *vs* RHE at 20 mV/s and 900 rpm for 50 cycles. ORR performance measurements were collected at RT in O_2 saturated 0.1 M $HClO_4$ electrolyte while cycling potential 0.05 to 1.2 V *vs* RHE at 20 mV/s and 1600 rpm after certain number of hydrogen peroxide cycles. Start-Stop cycling was designed as a fast aggressive protocol to simulate the fuel cell stack conditions related to fuel starvation, in which insufficient current from the anode due to lack of hydrogen causes the cell potential to increase until oxidation of carbon occurs. The catalyst durability was tested at RT in argon saturated 0.1 M $HClO_4$ electrolyte while cycling potential 1.0 to 1.5 V *vs* RHE at 100 mV/s and 1600 rpm for 6,700 cycles. ORR performance measurements were collected at RT in in O_2 saturated 0.1 M $HClO_4$ electrolyte while cycling potential 0.05 to 1.2 V *vs* RHE at 20 mV/s and 1600 rpm after certain number of start-stop cycles.

Two distinct durability protocols were carried out on a single PEM fuel cell to estimate the lifetime of a fuel cell operating with a FePhen@MOF-$ArNH_3$ cathode. The nitrogen cycling protocol employs an inert oxidant gas on the cathode and simulates fuel cell stack conditions using a potential step excitation (3 s hold at 0.6 and 1.0 V *vs* RHE). The oxygen cycling protocol employs a reactive oxidant gas on the cathode while simulating drive cycles by using a cyclic potential sweep excitation (50 mV/s from 0.2 to 1.1 V *vs* RHE).

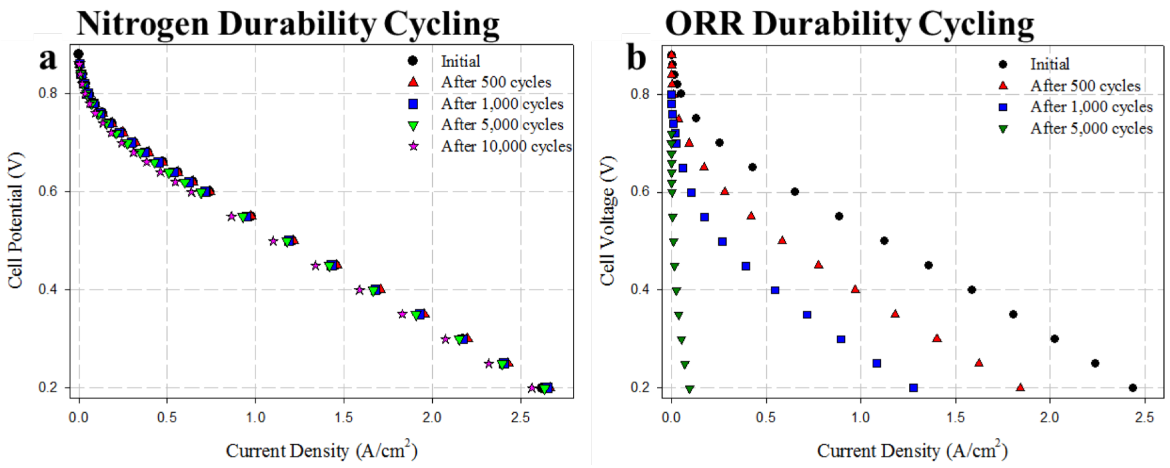

Figure 3.4: (a) H_2/O_2 fuel cell polarization curves for FePhen@MOF-$ArNH_3$ cathode (loading of 2 mg/cm^2) using Nafion (NRE 211) membrane measured intermittently 0 to 10 k load cycles (using 3 second hold and pulses between 0.6 to 1.0 V under nitrogen flow). (b) H_2/O_2 fuel cell polarization curves for similar MEA from (a) measured intermittently 0 to 5 k accelerated stress cycles (50 mV/s potential cycling between 0.2 to 1.0 V under oxygen flow).

Polarization curves were collected under the U.S. Department of Energy (US DOE) suggested testing conditions of 80 °C, 100% relative humidity, 1 bar partial pressure of H_2/O_2 (1.5 bar total pressure) and/or 0.4 bar partial pressure of O_2 in H_2/air (2.5 bar total pressure). A constant ionomer/carbon ratio of 60% and cathode catalyst loading of ~2 mg/cm_2 was maintained for both durability tests. H_2/O_2 polarization plots were measured initially and periodically throughout the durability tests (Figure 3.4) to evaluate the effect of cycling on cell performance.

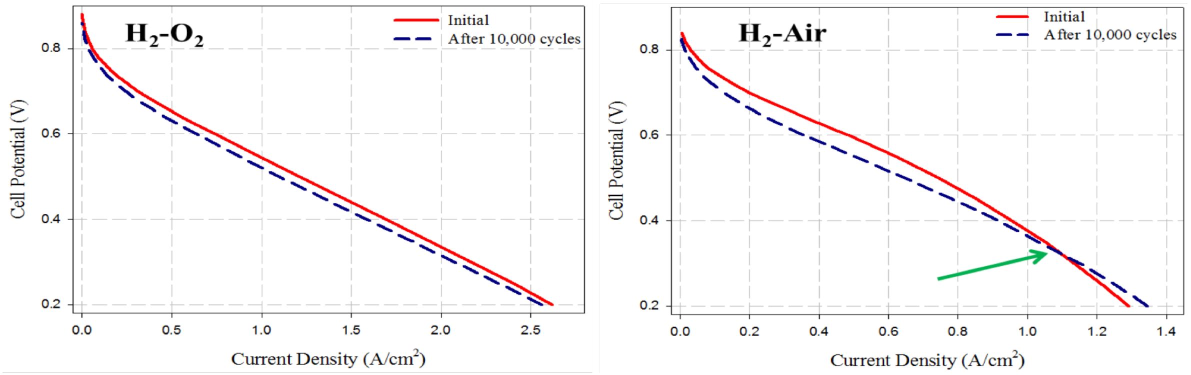

Figure 3.5: (a) H_2/O_2 fuel cell polarization curves for FePhen@MOF-ArNH$_3$ cathode (loading of 2 mg/cm^2) using Nafion (NRE 211) membrane measured initially and after 10k load cycles (using 3 second hold and pulses between 0.6 to 1.0 V under nitrogen flow). (b) H_2/Air fuel cell polarization curves for same MEA from (a) measured initially and after 10k load cycles.

As shown in Figure 3.4 a, the H_2/O_2 cell performance with a FePhen@MOF-ArNH$_3$ cathode was remarkably stable during the nitrogen durability cycling. The cell maintained an OCV of 0.95 V *vs* RHE throughout 10,000 load cycles and the high-frequency resistance (HFR), a measure of the resistance of all the MEA components, remained at 5 mΩ/cm^2 after the durability cycling. After 10,000 cycles there were no changes to the shape of the polarization curve indicating that FePhen@MOF-ArNH$_3$ seems to be electronically stable in the potential range scanned (0.6 to 1.0 V *vs* RHE). At a cell voltage of 0.8 V, where ORR is mostly under kinetic control, the current density dropped by 39% indicating either degradation of ORR active sites or reduced electrochemical surface area. At a cell voltage of 0.6 V, where ORR is controlled by kinetics and mass transport, the current density only dropped by 14% indicating that mass transport properties of the electrode were not negatively affected. The H_2/Air polarization curves were more telling of the mass transport properties of a cathode catalyst due to the lower concentration of oxygen (~20% *vs* 100%). As can be seen in Figure 3.4 b, there is a hysteresis at approximately 0.3 V at which point the current density of the cycled MEA actually increases above the current density obtained with the fresh MEA. This indicates that the mass transport properties are actually enhanced after the nitrogen durability cycling of FePhen@MOF-ArNH$_3$.

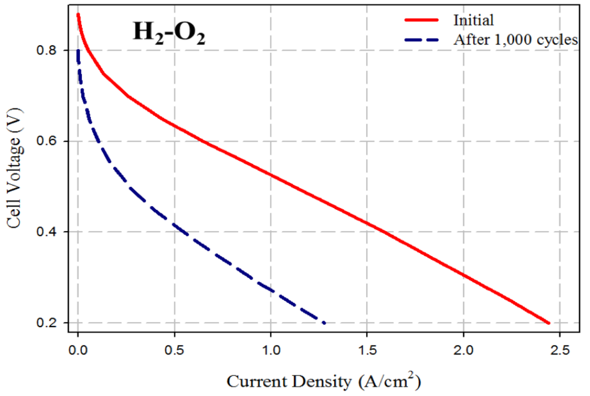

Figure 3.6: H_2/O_2 fuel cell polarization curves for FePhen@MOF-ArNH$_3$ cathode (loading of 2 mg/cm^2) using Nafion (NRE 211) membrane measured initially and after 5k (50 mV/s potential cycling between 0.2 to 1.0 V under oxygen flow).

The FePhen@MOF-ArNH$_3$ cathode based MEA was much less stable with the oxygen cycling durability test (Figure 3.4). The OCV dropped by 11% after just 1,000 cycles (0.89 vs 0.73 V *vs* RHE) and there was a 26% increase in the HFR (6 mΩ/cm^{2}to 8 mΩ/cm^2). At 0.8 V the current density decayed by 98% indicating significant destruction of the ORR active site under these conditions. At 0.6 V the current density experienced an 84% drop and at 0.2 V the reduction in current density was only 47%. Although the oxygen durability cycling was far more destructive to the FePhen@MOF-ArNH$_3$ cathode based MEA, it still appears that the degradation mechanism is most catastrophic in the low current density region. Cycling with oxygen flowing to the cathode enables ORR, which results in the formation of water in cathode catalyst layer. The presence of water could cause flooding issues that would inhibit oxygen from reaching the active site.[82] Another possibility is the presence of water while cycling the cell could induce oxidation of the carbon support causing a decrease in the conductivity of the catalyst layer.[83] If the carbon is being electrochemically oxidized, the hydrophobicity/hydrophilicity of the carbon would change and increased hydrophillicity would decrease the gas permeability.[84] However, there are different types of carbon present in the catalyst layer (graphite, CNTs, etc.) as well as the gas diffusion layer (GDL). Since the fuel cell is made up of several components (electrocatalysts, membranes, GDLs, and bipolar plates) it is difficult to determine the degradation mechanism and which component is affected.

In an effort to isolate the degradation mechanisms that are happening to the electrocatalyst alone, three different durability tests were performed using the RRDE technique. First, the ORR durability cycling protocol used previously in PEM was also carried out in 0.1 M $HClO_4$ for 6,200 cycles. Next, cycling of larger potential window (0.05 to 1.2 V *vs* RHE) was carried out in the presence of hydrogen peroxide (H_2O_2, product of $2e^-$ ORR mechanism) to explore the possibility of catalyst degradation from H_2O_2 attack of active sites. Finally, high voltage cycling (1.0 to 1.5 V vs RHE) was conducted to explore electrocatalyst degradation from the electrochemical oxidation of the carbon (carbon corrosion). Fuel starvation on the anode due to fuel cell start/stop conditions can cause the cell potential to increase and consume the carbon in place of the absent fuel.

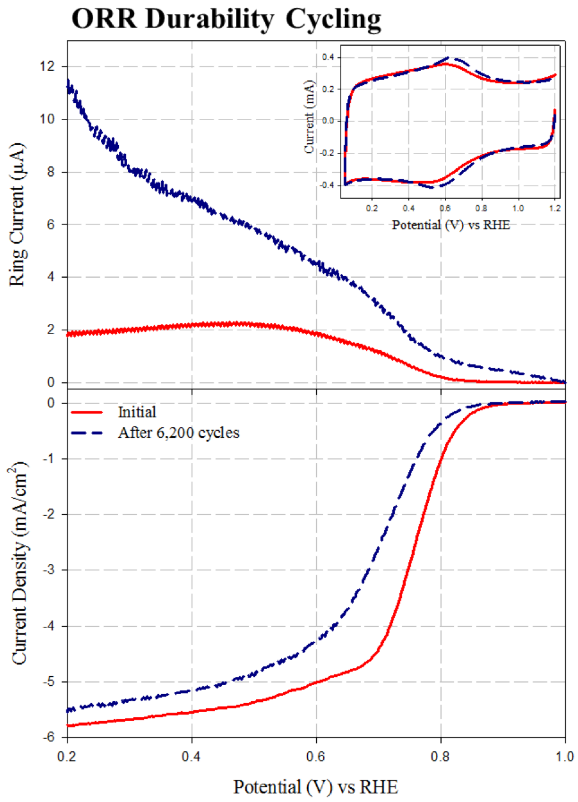

Figure 3.7: Disk- and ring-currents measured on FePhen@MOF-ArNH$_3$ in O_2 saturated 0.1 M $HClO_4$ at 20 mV/s with a rotation rate of 1600 rpm at room temperature. E_{ring}=1.3 V *vs* RHE. FePhen@MOF-ArNH$_3$ ORR polarization plots initially and after 6,200 accelerated stress cycles (0.2 – 1.1 V *vs* RHE at 50 mV/s and rotation rate of 900 rpm in Ar saturated 0.1 M $HClO_4$).

The ORR mechanism on FePhen@MOF-ArNH$_3$ was investigated in detail in Chapter 3. Briefly, Fe/Fe_3C nanoparticles are encapsulated in a nitrogen-doped (N-doped) carbon structure and ORR activity is attributed to the N-doped carbon surface. The presence of Fe in the synthesis is critical for catalyzing the graphitization of the carbon precursors, but could enhance the electronic properties of the carbon to enable easier adsorption of O_2 and promote the full $4e^-$ reduction to water in acidic media. The RRDE profile of FePhen@MOF-ArNH$_3$ before and after ORR durability cycling in 0.1 M $HClO_4$ is shown in Figure 3.7. The potential was cycled from 0.2 to 1.1 V *vs* RHE with a scan rate of 50 mV/s in oxygen saturated 0.1 M $HClO_4$ with an electrode rotation of 900 rpm The performance RDE profiles were measured in O_2 saturated 0.1 M $HClO_4$ using a scan rate of 20 mV/s and an electrode rotation rate of 1600 rpm, before and after 6,200 durability cycles. Following the ORR durability cycling of FePhen@MOF-ArNH$_3$ the overpotential for ORR increased by 30 mV and the half-wave potential (E½) shifted cathodically by 60 mV (0.69 V *vs* 0.75 V). Additionally, there is a slight reduction in the magnitude of the diffusion limiting current ($i_{\lim}$) which is defined by the Levich equation:

$$i_{\lim}=0.62nFD^{2/3}v^{-1/6}C_o \qquad (3.1)$$

where n is the number of electrons transferred, F is the Faraday constant, D is the diffusion coefficient of O_2 in 0.1 M $HClO_4$, v is the kinematic viscosity and Co is the concentration of O_2 in the electrolyte. The electrolyte used in the RRDE experiment remained constant, which implies the number of electrons transferred is the only variable from eqn (5.2) that could be affected by the ORR durability cycling. A second working electrode (ring electrode held at 1.3 V *vs* RHE) was used to detect the peroxide intermediate produced from the 2e$^-$ reduction mechanism of oxygen. As can be seen in Figure 3.7, the onset of the peroxide oxidation peak detected at the ring electrode coincides with the onset of ORR at the disk electrode for the fresh electrocatalyst. At very high overpotentials (E < 0.5 V) FePhen@MOF-ArNH$_3$ becomes more efficient for ORR and the peroxide detected at the ring decreases. After ORR durability cycling the oxidation of peroxide still commences with the onset of ORR, but the peroxide detected continues to increase at high overpotentials (~0.4 V). It has been shown in basic media that an increase in peroxide production at this potential is due to the 2e$^-$ reduction of oxygen by the hydroquinone/quinone functionalities on the carbon support.[16,85] The CV of FePhen@MOF-ArNH$_3$ (Figure 3.8 inset) after ORR durability cycling shows an increase in the peak current at ~0.55 V from the hydroquinone/quinone redox couple formed on the surface of the carbon.[86] The CV is only able to quantifiy the surface oxides that are electrochemcally active, but these results suggests that the carbon is electrochemically oxidized during the ORR durability cycling protocol and the new surface oxide groups either destroy some of the original active sites or inhibit oxygen from reaching the active site. ORR on the original active site proceeds predominantly through a 4e- reduction pathway, but the increace of surface oxides on the carbon results in an increase of the peroxide produced. The increase in peroxide produced by ORR durability cycled FePhen@MOF-ArNH$_3$ could be due to the contribution of 2e- reduction of oxygen by the quinone functionalities.

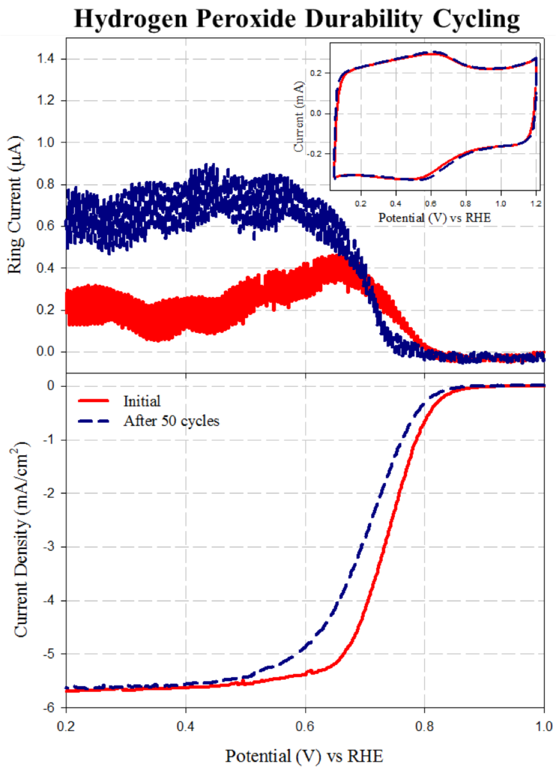

Figure 3.8: Disk- and ring-currents measured on FePhen@MOF-ArNH$_3$ in O_2 saturated 0.1M $HClO_4$ at 20 mV/s with a rotation rate of 1600 rpm at room temperature. E_{ring}=1.3 V *vs* RHE. FePhen@MOF-ArNH$_3$ ORR polarization plots initially and after 50 cycles (0.05 – 1.2 V *vs* RHE at 20 mV/s and rotation rate of 900 rpm) in argon saturated 0.5 M H_2SO_4 with 70 mM H_2O_2.

Next, the stability of the active sites of FePhen@MOF-ArNH$_3$ in the presence of a high concentration of H_2O_2 was investigated. The RRDE profile of FePhen@MOF-ArNH$_3$ in 0.1 M $HClO_4$ before and after H_2O_2 durability cycling is shown in Figure 5.5. To test the catalyst durability the potential was cycled from 0.05 to 1.2 V *vs* RHE with a scan rate of 20 mV/s in argon saturated 0.5 M H_2SO_4 with 70 mM H_2O_2 and an electrode rotation of 900 rpm. The performance RDE profiles were measured in O_2 saturated 0.1 M $HClO_4$ using a scan rate of 20 mV/s and an electrode rotation rate of 1600 rpm, before and after 50 durability cycles. Following the H_2O_2 durability cycling of FePhen@MOF-ArNH$_3$ the overpotential for ORR increased by 30 mV and the E½ shifted cathodically by 40 mV (0.7 V *vs* 0.74 V). Despite the decay in the ORR activity the magnitude of the diffusion limiting current was unaffected by the H_2O_2 durability cycling, which implies that the original active site is not degraded. The peroxide oxidation ring current of the H_2O_2 durability cycled catalyst still coincides with the onset of ORR at the disk, but has a slightly higher magnitude. Additionally, the H_2O_2 durability cycled FePhenMOF-ArNH$_3$ still exhibits efficient 4e$^-$ reduction of oxygen at higher overpotentials. The CV of the H_2O_2 durability cycled catalyst does display a very slight increase in the redox peak from the hydroquinone/quinone redox couple, indicating the introduction of some surface oxides. It is known that H_2O_2 will decompose in acidic media to form peroxide radicals (•OH and •OOH) that lead to corrosion of carbon. Based on these results it appears that active site of FePhen@MOF-ArNH$_3$ is stable in the presence of H_2O_2, but it is likely that some of the carbon will be oxidized by the peroxide radicals to form oxygen functionalities on the surface.

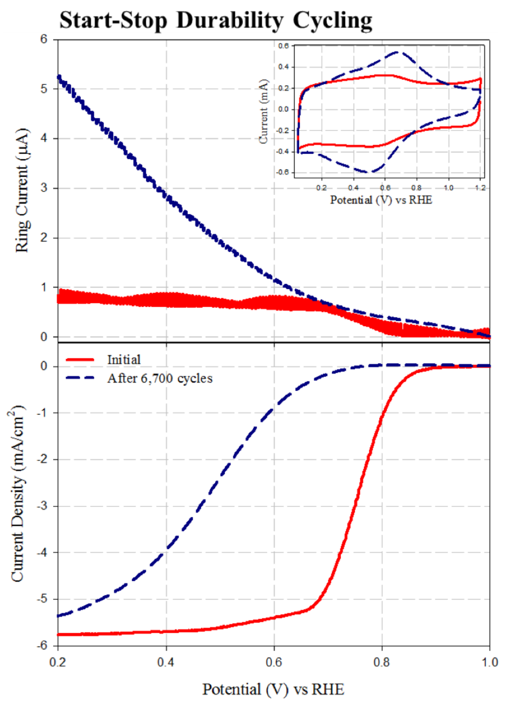

Figure 3.9: Disk- and ring-currents measured on FePhen@MOF-ArNH$_3$ in O$_2$ saturated 0.1M HClO$_4$ at 20 mV/s with a rotation rate of 1600 rpm at room temperature. E_{ring}=1.3 V *vs* RHE. FePhen@MOF-ArNH$_3$ ORR polarization plots initially and after 6,700 start-stop cycles (1.0 – 1.5 V *vs* RHE at 100 mV/s and rotation rate of 1600 rpm in argon saturated 0.1 M HClO$_4$).

Finally, high voltage (start/stop) cycling was conducted to further explore the effects of carbon corrosion on FePhen@MOF-ArNH$_3$. The RRDE profile of FePhen@MOF-ArNH$_3$ before and after start-stop durability cycling in 0.1 M HClO$_4$ is shown in Figure 3.10. To test the durability of the carbon in FePhen@MOF-ArNH$_3$ the potential was cycled from 1.0 to 1.5 V *vs* RHE with a scan rate of 100 mV/s in argon saturated 0.1 M HClO$_4$ with an electrode rotation rate of 1600 rpm. The performance RDE profiles were measured in O$_2$ saturated 0.1 M HClO$_4$ using a scan rate of 20 mV/s and an electrode rotation rate of 1600 rpm, before and after 6,700 durability cycles. Following the start-stop durability cycling of FePhen@MOF-ArNH$_3$ the overpotential for ORR increased by 150 mV and the E½ shifted cathodically by 270 mV (0.48 V *vs* 0.75 V) indicating significant degradation of the active sites. The reduction of available active sites is further supported by the lack of a well-defined diffusion limiting current as well as a slight reduction in magnitude following the start-stop durability cycling. The onset of the peroxide oxidation peak detected at the ring electrode coincides with the onset of ORR at the disk electrode for both the fresh and cycled catalyst. However, the ring current of the cycled catalyst continually increases as the overpotential is increase indicating that start-stop cycling makes FePhen@MOF-ArNH$_3$ less efficient for the 4e$^-$ reduction of oxygen. The CV of the start-stop cycled catalyst (Figure 3.9, inset) shows dramatic changes from the cycling protocol. There is a decrease in the double layer charging above 1 V after the durability cycling, indicating that the surface area has been reduced. The peak from the hydroquinone/quinone redox has increased significantly indicating introduction of considerable amounts of surface oxides to the carbon surface. Based on these results it appears the start-stop cycling causes electrochemical oxidation of the carbon surface introducing surface oxides and some removal of carbon from the conversion of surface oxides to CO$_2$ according the following mechanism in acidic media:

$$C_s \rightarrow C_s^+ + e^- \tag{3.2}$$

$$C_s^+ + ½H_2O \rightarrow C_sO + H^+ \tag{3.3}$$

$$2C_sO + H_2O \rightarrow C_sO + CO_2\ (g) + 2H^+ + 2e^- \tag{3.4}$$

One of the major concerns of using Fe-based non-PGMs as cathode catalysts in electrochemical energy conversion devices is the stability of the iron during operation. The presence Fe-ions and their potential to catalyze any Fenton type process resulting in peroxide free radical formation would contribute to degradation of multiple device components that are essential for long-term durability. As discussed in Chapter 3, the presence of iron in the synthesis of FePhen@MOF-ArNH$_3$ is imperative to form the most active ORR electrocatalyst, even though the iron is not directly involved in the ORR mechanism. FePhen@MOF-ArNH$_3$ is unusual in that there are no detectable Fe-N$_x$ moieties present in the preliminary catalyst, but it is important to investigate what the effect the durability cycling will have on the Fe that is encased in the graphitic carbon network. X-ray absorption spectroscopy (XAS) is an element specific technique that allows us to probe changes in the structural and electronic properties of Fe under simulated operating conditions of a fuel cell using a specially designed spectro-electrochemical cell[10]. The three distinct durability protocols that were performed using RRDE (Figure 3.10 a) were also carried out on XAS electrodes. Spectra were collected of fresh and cycled electrodes as a function of potential in 0.1 M $HClO_4$ electrolyte saturated with either oxygen or nitrogen. An *in situ* X-ray absorption near-edge spectrum (XANES) is an extremely powerful tool for capturing the key feature of ORR on a Fe-N_x active site. As the potential applied to the XAS electrode is increased from 0.1 up to 0.9 V, the Fe K−edge shifts toward a higher energy due to the Fe^{2+}/Fe^{3+} redox transition of the Fe-N_x species. The XANES edge shift arises exclusively from the Fe-N_x species, since the valence state of the metallic iron encapsulated in the carbon matrix does not change with applied potential. The XANES of the durability cycled electrodes are shown in Figure 3.10 b, and it can be seen that FePhen@MOF-ArNH$_3$ remains free of Fe-N_x moieties after the ORR and H_2O_2 cycling. However, the XANES of the start-stop cycled electrode has the signature edge shift indicating some the metallic Fe has been dissolved and is now present as Fe-ions that experience the Fe^{2+}/Fe^{3+} redox transition. Based on these results, we conclude that some of the Fe/Fe$_x$C nanoparticles that are covered by fewer graphitic sheets are exposed to the acidic environment during the carbon corrosion treatment and hence are dissolved. One of the original active site theories proposed by Yeager,[16,87,88] the formation of M-N_x sites resulted from the dissolution of exposed metal/metal oxides in acidic electrolyte and their eventual adsorption on nitrogen sites coordinated to the

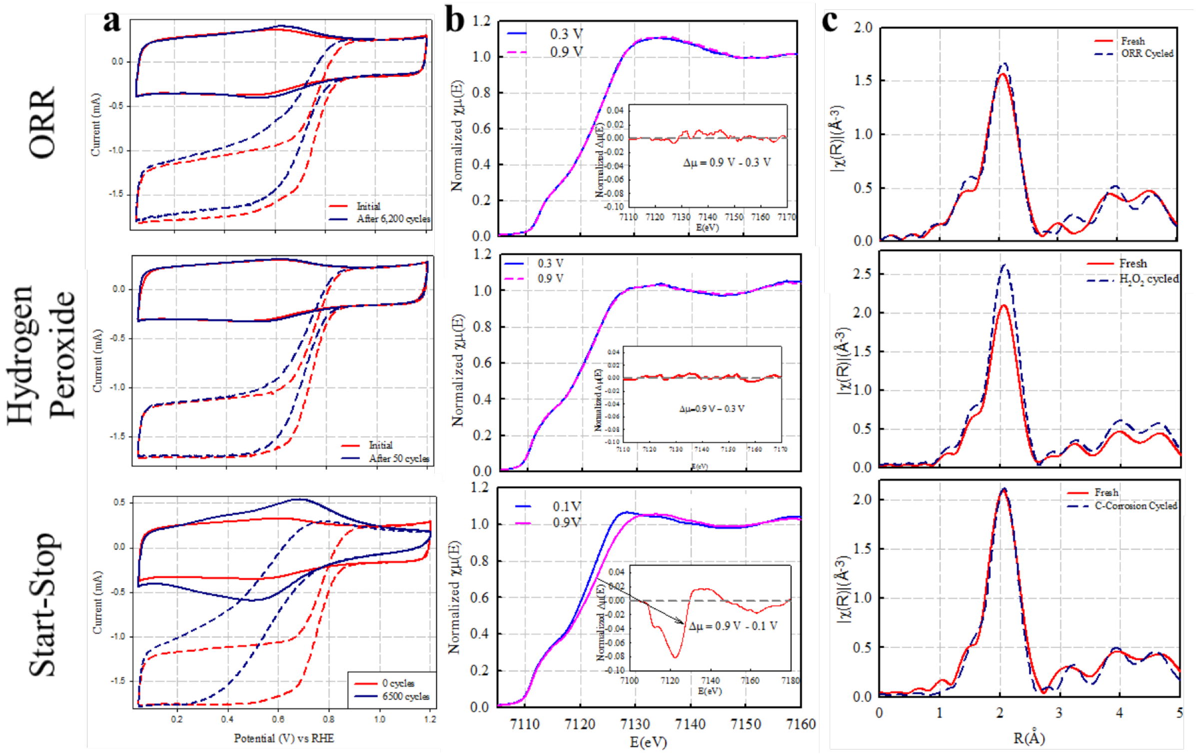

Figure 3.10: (a) CV and ORR polarization RDE profiles measured on FePhen@MOF-ArNH$_3$ before and after corresponding durability cycling protocol. CVs measured in argon saturated 0.1 M $HClO_4$ electrolyte at 20 mV/s with no rotation at RT. ORR polarizations measured in oxygen saturated 0.1 M $HClO_4$ electrolyte at 20 mV/s with rotation rate of 1600 rpm at RT. (b) Potential dependent normalized Fe K-edge XANES of FePhen@MOF-ArNH$_3$ after corresponding durability cycling protocol collected in N_2 saturated 0.1M $HClO_4$, inset $\Delta\mu = \mu$ (0.9 V) - μ (0.3 V). (c) Fourier transform EXAFS of FePhen@MOF-ArNH$_3$ before and after corresponding durability cycling procedure collected at Fe K-edge (7112 eV) in N_2 saturated 0.1M $HClO_4$ held at 0.3 V *vs* RHE.

carbon. The start-stop cycling could allow some of the dissolved Fe-ions to either adsorb on nitrogen sites that are doped into the carbon matrix to form the Fe-N_x active site, similar to the active site formation previously proposed by Yeager.[16,87,88] In another theory proposed by Goellner *et al*,[89] the carbon embedded Fe particles that are exposed from high voltage cycling produce Fe^{3+} ions that precipitate to form Fe^{III} hydroxides ($Fe(OH)_3$).

Fourier Transform (FT) extended X-ray absorption fine structure spectra (EXAFS) of the fresh and durability cycled electrodes collected at 0.3 V in nitrogen saturated electrolyte are shown in Figure 3.10 c. Electrodes held at 0.3 V *vs* RHE are considered to be free of adsorbates, and therefore represent a catalyst structure with a clean surface[17]. The Fe K-edge of fresh FePhen@MOF-ArNH_3 is characterized by a peak at ~2.2 Å, which was previously fit with a Fe-Fe scattering path with a bond length that corresponds well with bulk iron and/or iron carbide (2.51 Å vs. 2.49/2.48 Å, respectively). The small shoulder off the main peak was fit with a Fe-C/N scattering path with a bond length of ~1.96 Å. As mentioned previously, XAS is effective tool for probing the structural and electronic properties of Fe, but has an inherent limitation in that it is unable to distinguish between low Z elements (C, N and O). Therefore, we are unable to conclusively say whether the shoulder contribution comes from C, N or O. The FT EXAFS of the fresh and durability cycled electrodes shown in Figure 3.10c show very little changes and reveal that the majority of the iron present in FePhen@MOF-ArNH_3 remains metallic through the durability cycling.

	Fresh		H_2O_2 Cycled	
	Fe-N/C	Fe-Fe	Fe-N/C	Fe-Fe
CN	-	7.0 ±0.05	0.8 ±0.4	8.7 ±0.4
R (Å)	-	2.50 ±0.01	1.90 ±0.07	2.51 ±0.01
$\sigma^2 \times 10^{-3}$	-	8 ±1	2 ±3	8 ±3

Table 3.1: In situ EXAFS Fit Results Hydrogen Peroxide Cycling. EXAFS fit results for FePhen@MOF-ArNH_3 before and after hydrogen peroxide cycling. Experiments performed at the Fe K-edge (7112 eV) as a function of potential in N_2 saturated 0.1M $HClO_4$ electrolyte. Coordination number (CN) and phase-corrected bond length (R) in angstrom are shown.

After H_2O_2 cycling, there is a slight increase in the main peak (2.2 Å), and this increase is more intense after H_2O_2 cycling. The fitting results (Table 3.1) of the H_2O_2 cycled FT EXAFS shows that the Fe-Fe scattering path coordination number (CN) increased from 7 to 8.7. These results indicate that the smaller Fe/Fe_xC NPs are selectively removed when high concentrations of peroxide are present during operation. The start-stop durability cycling produces very few differences in the FT EXAFS, but we know from the XANES that some of the metallic Fe has been dissolved into Fe-ions. However, the FT EXAFS of the start-stop cycled electrode indicate that most of the Fe is still present in the metallic form. Based on these results it appears that the iron present in FePhen@MOF-ArNH_3 is stable under normal driving conditions, but becomes vulnerable to dissolution during the high voltage transients experienced during start up and shut-down.

Most interestingly, the start-stop cycled catalyst is so heavily oxidized that after cycling the onset of the ORR curve shifts so far cathodically that is now coincides with the hydroquinone/quinone redox couple (Fig 5.7 a). This could indicate the surface has become so heavily oxidized that the original carbon active site has been destroyed and ORR is now proceeding on the oxidized carbon surface.

In conclusion, we investigated the durability and degradation of FePhen@MOF-ArNH_3 in a PEM fuel cell environment using single-cell cycling, RRDE cycling and *in situ* XAS investigations. The device components of a PEM fuel cell are exposed to strongly acidic and oxidizing conditions at elevated temperatures, which necessitate the use of a first class electrocatalyst. Extensive research into the use of transition metal based electrocatalysts in place of the state-of-the-art platinum based electrocatalysts has produced highly active materials, but little is known about their degradation mechanisms. FePhen@MOF-ArNH_3 was very stable during the nitrogen fuel cell durability cycling, but suffered significant performance decline during the oxygen fuel cell cycling. Three RRDE durability cycling protocols revealed that increased surface oxides due to electrochemical oxidation of the carbon resulted in a decrease of the ORR activity. *In situ* XAS revealed that the Fe is stable during normal fuel cell operating conditions, but aggressive carbon corrosion can expose the Fe/Fe_xC particles leading to dissolution. Based on all of these results it appears the main degradation mechanism is the electrochemical oxidation of the carbon, which produces surface oxides that change the conductivity and hydrophobicity of FePhen@MOF-$ArNH_3$.

Task 4/8. Mechanistic Studies (*Ex-Situ* and *In-Situ* Spectroscopy and Modeling)

Active site debate. Despite these progresses in developing M–N_x-C catalysts, the exact nature of the active sites induced by high temperature pyrolysis, as well as the reaction mechanisms, still remains unclear. The roles of the M, N, and C toward the ORR active site have been under extensive debate, although all these elements are required in the precursor material(s) to produce efficient ORR catalysts in acidic media. Regarding the transition metal M, many researchers believe that it is the essential part of the active site (commonly labelled as M-N_x-C) and participates into the ORR directly. Using aberration-corrected annular dark field scanning transmission electron microscopy (STEM-ADF) and electron energy loss spectroscopy (EELS) mapping techniques, Li *et al.*[90] directly observed the iron atoms on the edges of graphene sheets in close proximity to nitrogen species, providing experimental evidences on the Fe-N_x-C moieties. The direct involvement of Fe in some Fe-based catalysts in mediating ORR was demonstrated by our previous studies, which show that the $Fe^{2+/3+}$ redox transition is accompanied with the adsorption of oxygenated species onto the central Fe ions, and the redox potential overlaps the ORR onset potential. Further, the ORR activity of the catalyst drops drastically when it is subjected to the poisoning test with the CN^- ions that are known to strongly coordinate with Fe. Among all 3d transition metals from Cr to Cu, Fe-based catalysts exhibit the highest activity probably owing to the appropriate redox potential. The insufficient stability of Fe-N_x-C catalysts can be significantly enhanced by alloying Fe with Co.

Besides M-N_x-C moieties, metal or metal oxides/carbides/nitrides encapsulated in N-doped Carbon shells (denoted as M@N-C hereafter) simultaneously formed during the heat treatment may be partly or completely responsible for the enhanced ORR activity.[91,92] Specifically, it was proposed that co-presence of the M-N_x-C and M@N-C species in certain catalysts is essential for the high onset-potentials obtained in acidic environment, which is accounted for by the dual-sites mechanism whereby the two adjacent sites are required to efficiently promote the $4e^-$ reduction pathway. This argument is questioned by recent studies which show that the Fe-N_4-C catalysts without any M@N-C species exhibit high ORR activities in acidic media. While these studies clearly demonstrate the Fe-N_4-C moieties with certain local configurations as efficient ORR catalysts, they do not necessarily eliminate the probability of M@N-C being ORR active. Indeed, it was demonstrated by many groups that the metallic Fe encapsulated in carbon nanotubes[39] or graphitic layers[20,93] can serve as a new active site for the ORR even in acidic media,[94] and the encapsulated Fe indirectly facilitates the ORR via modification of the electronic properties of C. Similarly, Chung *et al.* showed that the PtFe nanoparticles encapsulated in thin N-doped Carbon shells (~1 nm) are highly active and durable for ORR as the thin carbon shells are highly permeable for the reactant molecules, whereas the ones with thick carbon shells (~3.5 nm) is inactive due to the loss of the permeability. This study suggests that the ORR activity of M@N-C catalysts is very sensitive to the thickness of the N-doped carbon shell, and therefore may vary drastically within non-PGM catalysts prepared via different routines. These new findings further obscure the nature of the active sites given that M-N_x-C and M@N-C sites usually co-exist in high-temperature treated non-PGM catalysts albeit recent success in completely remove of the later species aforementioned.

On the other hand, some researchers argue that the M only serves to catalyze the formation of the nitrogen-doped carbon (N-C) active sites during the pyrolysis procedures rather than being a part of the active site, and the ORR activity is attributed to the metal-free N-C sites. However, many previously claimed metal-free N-C catalysts with decent ORR activity were synthesized with Fe-containing precursors. It is highly debatable that this class of catalysts is "metal-free" since the Fe impurities from Fe-containing precursors cannot be completely removed by the acidic treatment, especially if the Fe is encapsulated in the carbon. The residual Fe impurities, even of trace amounts that are undetectable by regular elemental analysis techniques such as x-ray photoelectron spectroscopy (XPS) and energy-dispersive x-ray spectroscopy (EDX), greatly promote the ORR. It is hereby suggested by Schuhmann *et al*[95] that any samples synthesized using Fe-containing precursors shall not be classified as "metal free" N-C catalysts. In addition, Fe impurities can also come from other sources such as the KOH electrolyte that has been commonly used for RDE testing on N-C catalysts, which was demonstrated to significantly promote the oxygen evolution reaction (OER). Therefore, even for N-C catalysts synthesized without using Fe-containing precursors, proper poisoning tests with appropriate poisoning agents such as CN^- ions (note CO is not a valid agent as it does not poison both non-pyrolyzed and pyrolyzed Fe-based catalysts[96]) are necessary to justify the complete devoid of M. In general, the ORR activity of unadulterated metal-free N-C catalysts in acidic media is far inferior to that of the corresponding M-N_x-C catalysts.[94]

As for both N-C and M-N_x-C active sites, the incorporated nitrogen has been demonstrated as the indispensable part for ORR, but the types of the nitrogen in the sites is a controversial subject. The active site Fe-N_4-C_x (commonly labelled as D1) has been identified across research groups around the world in both Fe-macrocycle-pyrolyzed catalysts[97-99] and Fe-N_x-C synthesized from individual Fe, N, and C precursors[21,24,25] using Mössbauer spectroscopy. It has been commonly believed that this site is formed upon the integration of the Fe-N_4 moiety with pyridinic N in the micropores bridging graphene sheets and/or in the edges of graphene sheets during pyrolysis. This is in consistent with the findings that that the pyridinic nitrogen is selectively formed on the edge of the carbon layers, and a higher relative content of $N_{pyridinic}$ correlate with better ORR activity.[100] However, Jaouen *et al.*[21] recently argued that this site is formed via an unusual integration of the Fe-N_4 moiety with pyrrolic N in the bridging edges of graphitic pores or zigzag graphene edges based on the advanced x-ray absorption near edge structure (XANES) analysis. Besides these Fe-N_4-C_x moieties with four coordinated nitrogen atoms, Fe-N_3[101] and X-Fe-N_4 (X represents the fifth axial ligand)[25,102,103] moieties integrated in graphene sheets were recently shown to be possible active sites with high ORR activity in pyrolyzed Fe-based catalysts.

The porous structure of carbon is another critical factor for the ORR activity of M-N_x-C materials. Ramaswamy *et al.* reported that highly disordered carbon supports yield higher ORR turnover numbers, which was explained as the electron-withdrawing character of carbon optimizes the bond strength between the metal center and the ORR intermediates. More recently, Jaouen *et al.* stated that the superior intrinsic ORR activity of the NH_3-pyrolyzed Fe-based materials to that of the Ar-pyrolyzed Fe-based materials shall be attributed to the basicity of the N-doped carbon optimized by the NH_3 treatment, rather than the local geometry of the active sites.[21]

Due primarily to the different opinions of the nature of the active sites, various ORR pathways such as direct 4e- reduction,[5,18,104] 2e- reduction,[105,106] or 2×2e- peroxide pathway (dual-site mechanism)[91,107] have accordingly been proposed. The ideal ORR kinetics with the highest efficiency in power generation is the reduction of O_2 to H_2O via a direct four-electron ($4e^-$) pathway mediated by one single site. A consensus that the Fe-N_x-C centers can efficiently promote the 4e- reduction of O_2 appears to be reached lately as some Fe-N_x-C catalysts without any M@N-C species exhibit exceptional ORR activity. In addition, a direct correlation between the content of the Fe-N_x-C centers and the kinetic current density of ORR has been observed based on both XPS and ^{57}Fe Mössbauer spectroscopy results. More recently, the M@N-C sites have also been shown to efficiently deliver the 4e- reduction in acidic media, and the devoid of Fe-N_x-C centers were justified either by CN^- poisoning test, or by *in situ* XAS method. Therefore, it is not surprising that a dual site mechanism has been proposed for catalysts containing both Fe-N_x-C and M@N-C species whereby oxygen is first reduced to H_2O_2 by Fe-N_x-C centers, followed by further reduction to H_2O by M@N-C sites.[91,107]

Most investigations on the active sites of pyrolyzed M-N_x-C catalysts are based on *ex situ* physicochemical characterization such as Mössbauer spectroscopy[25,108,109], x-ray photoelectron spectroscopy (XPS)[25,99,110], x-ray diffraction (XRD),[39,111] time of flight secondary ion mass spectroscopy (ToF-SIMS),[112,113] or transmission electron microscopy (TEM).[5,114,115] However, such information may be disconnected from the electrocatalysis as we recently showed that the local structure of the Fe-N_x-C moieties under *in situ* working conditions is different from that under *ex situ* conditions, and changes drastically during ORR as induced by the $Fe^{2+/3+}$ redox transitions by employing advanced *in situ* XAS studies. In this work, a broad variety of pyrolyzed

Fe-N_x-C catalysts are systemically investigated by combining *in situ* XAS and *ex situ* Mössbauer spectroscopy to elucidate the structure/activity correlations within Fe-N_x-C catalysts. As shown below, our work will present new experimental results obtained from *ex situ* and *in sit*u Mossbauer and XAS results and discuss the implications of these in the current understanding of the ORR mechanisms.

*Catalyst preparation***.** Iron(III) meso-tetraphenylporphyrin chloride (FeTPPCl) (Alfa Aesar) was mixed with Black Pearl carbon (BP) in the mass ratio 1:4 and ball milled for 2 hours at 400 rpm, followed by pyrolysis at 300-800°C under argon atmosphere. There is some carbon and nitrogen loss in the precursor mix during pyrolysis. The loading of iron in the pyrolyzed catalysts, including both complexed iron and/or metallic iron forms, was typically ~3% by weight as determined by energy dispersive analysis of X-rays and inductively coupled plasma mass spectrometry (ICP-MS).[17] Detailed informaion on the preparation and pyrolysis process of polyaniline Fe (PANI-Fe-C) was given in other recent work.[5,39] In brief, a short-chain aniline oligomer was mixed with high-surface area carbon material (pristine Ketjenblack EC-300J) and transition metal precursors (iron(III) chloride), followed by the addition of ammonium persulfate to fully polymerize the aniline. After vacuum-drying, the remaining solid material underwent a heat treatment at 900°C in N_2 atmosphere, and then leached in 0.5 M H_2SO_4 at 80°C for 8 hours. The preleached catalyst was subjected to another heat treatment under N_2 atmosphere. The initial Fe content in the precursor was chosen to be 3.3 wt% here, and the changes of the Fe content during the synthesis and heat treatments is provided in a previous study.[39]

Electrochemical measurements. All electrochemical measurements were made at room temperature using a rotating disk electrode (RDE) setup. Catalyst inks were prepared by ultrasonically dispersing the catalyst powder in a 1:1 (by volume) ratio of water/isopropanol solution. Typical catalyst loadings employed were 100 μg/cm^2 of catalyst on a 5.61 mm glassy carbon disk. Reversible hydrogen electrode (RHE) generated using the same electrolyte as the bulk was used as the reference electrode. The gold ring electrode was held at 1.1 V vs RHE in alkaline electrolyte and at 1.3 V vs RHE in acidic electrolyte to detect stable peroxide intermediate. Square-wave voltammetry experiments were performed using a step potential of 5 mV, potential amplitude of 20 mV, and a scan frequency of 10 Hz. Britton−Robinson buffer solutions were used for electrochemical experiments performed at electrolyte pH ranging from 2 to 12. For these pH conditions from 2 to 12, a Ag/AgCl reference electrode prepared in saturated sodium chloride was utilized for the experiments.

*X-ray absorption spectroscopic (XAS) measurements***.** The *in situ* XAS studies were performed at the X3B beamline of the National Synchrotron Light Source (NSLS, Brookhaven National Laboratory, NY). A detailed description of the *in-situ* spectro-electrochemical cell design is given elsewhere.[116] Spectra at Fe K-edge were collected in fluorescence mode using a 32-elements GE solid state dectector. Measurements were performed at different electrode potentials from 0.1 V to 1.0 V (or higher) *vs.* RHE (all the potentials mentioned in this paper are *versus* RHE unless otherwise specified). Details of electrochemical procedure associated with the *in situ* XAS measurements, and the XAS data analysis are provided in the previous section.

FEFF calculations. The FEFF9 program, an *ab initio* real space multiple-scattering (RSMS) code that employs full multiple scattering self-consistent field (SCF) calculations,[117] has been demonstrated to be suitable for mimicking the hybridization between the 4s and 4p states of iron and the symmetry-adopted atomic orbitals of the surrounding atoms in Fe-based complexes.[118,119] The Fe-N_4-C_8 with two atomic shells centered on the Fe atom (Figure 4.1b, inset), which can be considered as the common part of the three cluster models (Fe-N_4-C_{12}, Fe-N_4-C_{10}, and Fe-N_4-C_8) used in our previous work[17] for Δμ analysis, was chosen for XANES calculations. The shells further away were not included for FEFF calculations as the XANES spectral lines of Fe-based composites are dominated by shells located at distances of less than 4 Å.[118] The cluster structure was tuned by displacing the central Fe atoms out of the N_4-plane with a variety of Fe-N bond lengths to evaluate the central Fe displacement effects on the XAENS spectra.

***DFT calculations*.** The DFT calculations were performed using the Vienna Ab initio Simulation Package (VASP)[120] code programs, following the recent work by Kattel et al.[121] The core electrons were described by the projector augmented wave (PAW)[122] and a plane wave basis with cutoff energy 400 eV was used to describe the valence electrons. For electronic exchange and correlation effects we used generalized gradient approximation (GGA) within the Perdew–Burke–Ernzerhof (PBE) parametrization.[123] Three clusters $Fe-N_4-C_x$ (x=8, 10, 12) were modeled using a 4×6 graphene cluster. In particular, a cell containing 26 carbon atoms was produced using a hexagonal graphene unit cell of 2 atoms. All the outer carbon atoms in the model clusters were passivated with hydrogen atoms. The $Fe-N_4$ cluster is embedded removing the central C-C bonds forming $Fe-N_4-C_{10}$ (Figure 4.1 middle). The $Fe-N_4-C_8$ cluster simulates the $Fe-N_4$ centers within porous defects of the C-C scaffold and its configuration is in agreement with a larger defect simulated by Kattel *et al.* (Figure 4.1 right).[121] Finally, the $Fe-N_4-C_{12}$ cluster is similar to the fragment of a heme compound. The $N_{axi}-Fe-N_4-C_x$ cluster was further produced by adding a fifth NH_2 ligand at the vertical below of $Fe-N_4$ plane. The NH_2 moiety, which has been commonly used for DFT calculations on similar models, is chosen here as an example of the fifth ligand, which by no means constitutes a definitive adjudication on the nature of the fifth ligand in the D3 site. For all these structures, the DFT calculations were performed with full relaxation of ionic positions until two consecutive relaxations reached an energy difference of 0.1 meV. A k-space mesh of 2×2×1 Monkhorst-Pack grids was used for the geometry optimization. The bond distances of the cluster models with optimized structures are summarized in Table 4.1. Spin polarization was included in electronic density of states (DOS) and binding energy calculations. The DOS (Figure 4.3) was calculated from the self−consistent solution of the Schrödinger equation using a denser k−point mesh of 8×8×1 and Gaussian smearing of the Fermi level of σ=0.1.

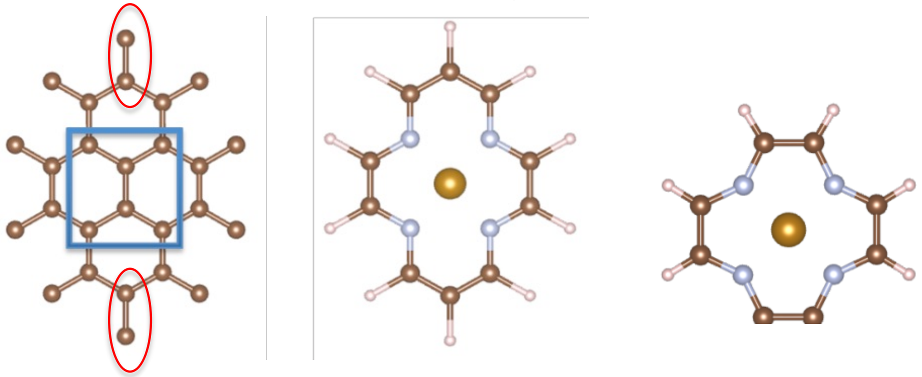

Figure 4.1. Top views of the super cell produced using a hexagonal graphene unit cell of 2 atoms (left). The $Fe-N_4$ cluster was embedded removing the central C−C bonds in the frame forming $Fe-N_4-C_{10}$ (middle). The $Fe-N_4-C_8$ cluster model (right) was created by further removing the C−C bonds on the top and bottom (in the red circles) and then self consistently relaxing the super cell.

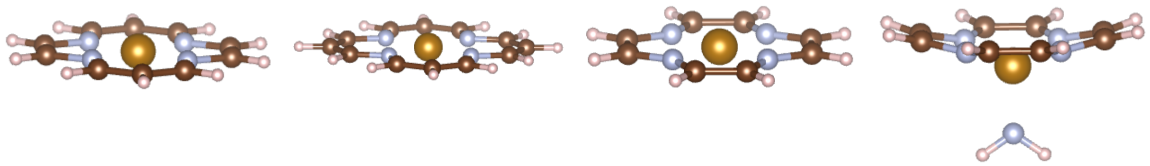

Fe-N_4-C_{10} (D1) Fe-N_4-C_{12} (D2) Fe-N_4-C_8 Fe-N_4-C_8 (D3)
NH_2

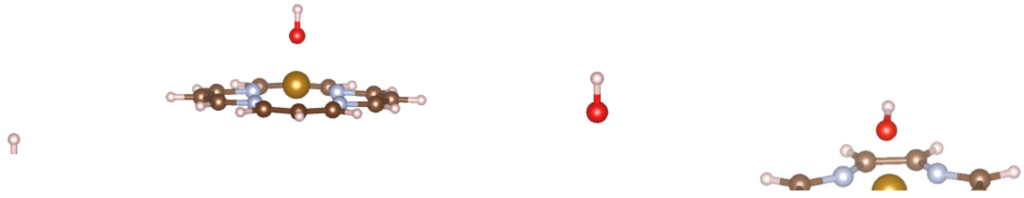

OH-Fe-N_4-C_{10} OH-Fe-N_4-C_{12} Fe-N_4-C_8 OH-Fe-N_4-C_8
NH_2

Figure 4.2. Side views of the geometries of the Fe-N_4-C_x models with or without the axial OH. Note the models exhibit distinct Fe−N switching behaviour upon the adsorption of *OH.

Table 4.1: DFT calculation results the bond lengths (Å) in the studied cluster models with optimized structures.

		Fe-N_1	Fe-N_2	Fe-N_3	Fe-N_4	Fe-N_{axi}	Fe-OH
Fe−N_4−C_{12}	clean	2.03	2.03	2.03	2.03	-	-
	-OH	2.21	2.22	2.21	2.22	-	1.79
Fe−N_4−C_{10}	clean	1.89	1.89	1.89	1.89	-	-
	-OH	1.90	1.90	1.90	1.90	-	1.81
Fe−N_4−C_8	clean	1.83	1.85	1.83	1.85	-	-
	-OH	1.87	1.87	1.87	1.87	-	1.77
NH_2-Fe−N_4−C_8	clean	1.89	1.89	1.89	1.89	1.86	-
	-OH	1.87	1.87	1.87	1.87	1.88	1.86

Table 4.2: DFT calculation results of the binding energy (BE) for ORR intermediate adsorbates O_2 (end on), OOH, O, and OH for Fe-N_4-C_8 and NH_2-Fe-N_4-C_8 clusters, together with the number of d_z^2 (e_g)-electrons. The optimized structures are summarized in Table 4.1, and the calculated electronic density of states (DOS) for the d-orbitals of the central iron is shown in Figure 4.2.

	BE (eV)				dz^2 (e_g)-electrons
	O_2	OOH	O	OH	
Fe-N_4-C_8	-2.44	-2.34	-5.27	-3.51	1.67
NH_2-Fe-N_4-C_8	-0.72	-1.10	-3.28	-2.61	1.11

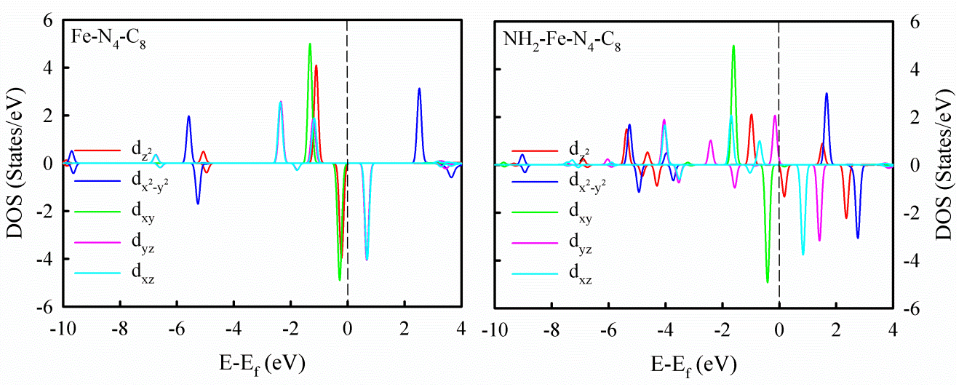

Figure 4.3. Calculated electronic density of states (DOS) for the d-orbitals of the central iron in the indicated cluster models

Fe-N switching behavior during ORR. It is known that the original porphyrin macrocycle possesses a square-planar Fe^{2+}-N_4 structure (D_{4h} symmetry), and the Fe^{2+}-center shifts out of the plane toward the $O(H)_{ads}$ (adsorbed O* and/or OH*) species when (H)O-Fe^{3+}-N_4 is formed.[17,109,124] This Fe-N switching behavior is illustrated by the XAS spectra of FeTPP-300-C (FeTPP pyrolyzed at 300 °C) collected at a potential ranging from 0.1 to 0.9 V in N_2-saturated 0.1 M KOH electrolyte (Figures 4.4a and 1b). The Fe K-edge XANES at 0.1 V closely resembles that of the pre-existing porphyrin macrocycle. In particular, the shoulder at 7117 eV is the fingerprint of the square-planar Fe-N_4 structure.[125] As the potential increases from 0.1 to 0.9 V the Fe K-edge shifting toward higher energy is indicative of the Fe^{2+}/Fe^{3+} redox transition.[17,125] Concurrently, the Fourier transform (FT) peak at ~1.6 Å arising from the Fe-N/O scattering increases in intensity and shifts to a larger radial distance. The corresponding increases in Fe-centered coordination number (Figure 4.4c) and bond distance (Figure 4.4d) caused by $O(H)_{ads}$ are confirmed by EXAFS fitting (Figure 4.4). The XAS spectra of FeTPP-300-C collected in N_2-saturated 0.1 M $HClO_4$ exhibit essentially the same trends, except that some of the Fe-N_4 moieties are already oxidized at 0 V due to the lower Fe^{2+}/Fe^{3+} redox potential at low pH, and therefore the Fe^{2+}/Fe^{3+} redox transition is not fully captured as in 0.1 M KOH electrolyte.

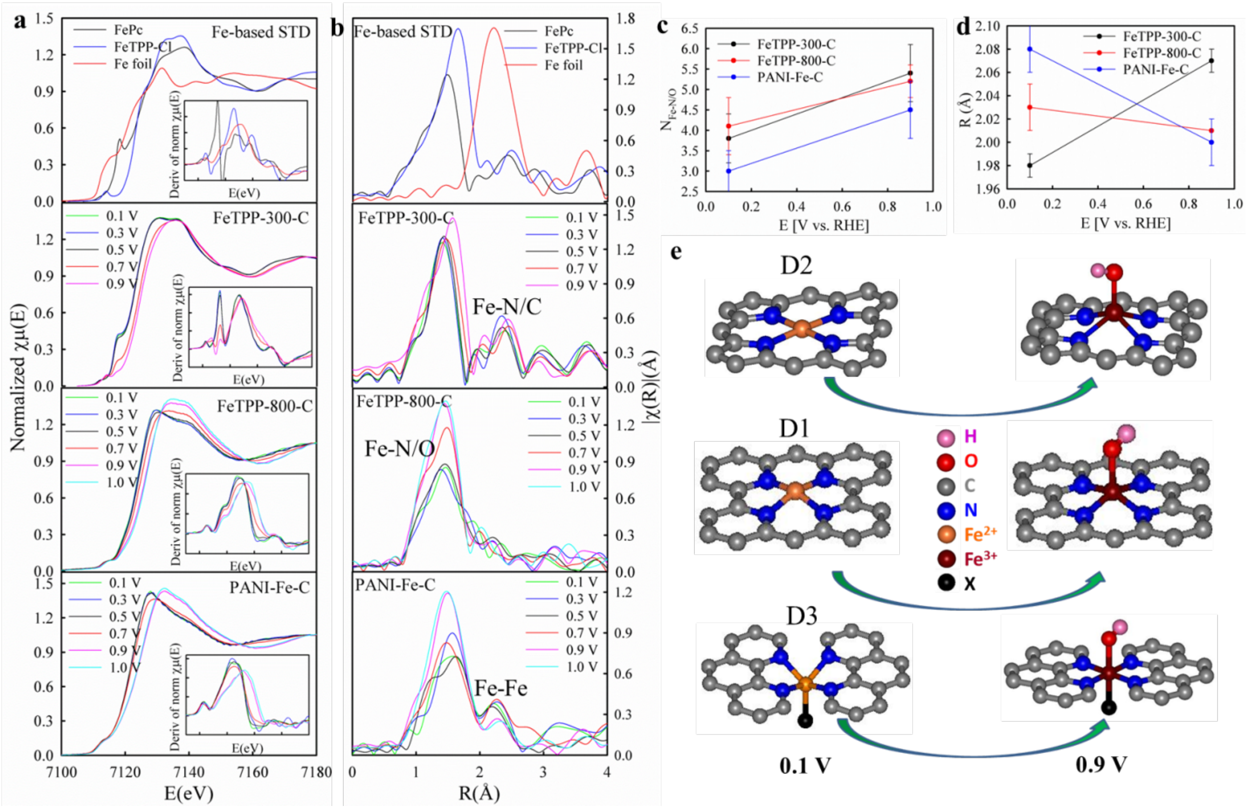

Figure 4.4. a) XANES at the Fe K-edge with concomitant first derivatives (insets). b) the corresponding FT-EXAFS of FeTPP-300-C, FeTPP-800-C, and PANI-Fe-C as a function of applied potentials *versus* reversible hydrogen electrode. The XANES and FT-EXAFS spectra of Iron (II) phthalocyanine (FePc), iron (III) meso-tetraphenyl porphyrin chloride (FeTPPCl), and bulk iron (top) were included as Fe-based standards for comparison. The spectra of FeTPP-800-C and PANI-Fe-C were collected in N_2-saturated 0.1 M $HClO_4$ electrolyte; while the spectra of FeTPP-300-C collected in N_2-saturated 0.1 M KOH electrolyte is displayed here to fully capture the Fe^{2+}/Fe^{3+} redox transition. The Fe-N/O (N and O cannot be distinguished by XAS as surrounding atoms) coordination numbers (c) and bond distances (d) of FeTPP-300-C, FeTPP-800-C, and PANI-Fe-C at 0.1 and 0.9 V vs. reversible hydrogen electrode (RHE) were obtained by EXAFS fits, and the derived Fe-N switching behavior is illustrated by three structural models ($Fe-N_4-C_x$) labelled as D2, D1, and D3, respectively, with/without axially bound $O(H)_{ads}$ (e). The atom labelled X represents the fifth ligand with its identity unknown. The vertical error bars in c and d are produced by the fitting software.

The same analysis was also conducted with FeTPP-800-C and PANI-Fe-C catalysts, for which the structure of the active site is unclear. Interestingly, the XAS spectra of the two catalysts collected in N_2-saturated 0.1 M $HClO_4$ exhibit the similar trends as observed on FeTPP-300-C: the Fe K-edge shifts toward higher energy with increasing potential, accompanied with the increase in Fe-N/O scattering peak intensity (Figure 4.4a and 1b). This indicates that the active sites in these catalysts also undergo a Fe^{2+}/Fe^{3+} redox transition that triggers the adsorption of *OH from water activation, but at much higher potentials (~0.7 V). It is noted that the spectra of all catalysts obtained in N_2- and O_2-saturated electrolyte at the same potential are within experimental uncertainties. This directly implicates that the Fe^{2+}-sites are poisoned by the *OH from water activation above the redox potential, which is consistent with our previous observation that the Fe^{2+}/Fe^{3+} redox potential overlaps with the ORR onset potential.[40] The higher Fe^{2+}/Fe^{3+} redox potential of pyrolyzed Fe-based catalysts compared to that of original $Fe-N_4$ macrocycles to a large extent accounts for the enhanced ORR activity *via* stabilization of active Fe^{2+}-sites at higher potentials. It is thus of particular importance to elucidate the structural origin and changes accompanying the redox potential increase, with apparent concomitant decrease in Fe-O binding energy.

A key difference in the active site structure within these catalysts lies in the average Fe-N bond distance ($R_{Fe\text{-}N}$). The $R_{Fe\text{-}N}$ in PANI-Fe-C is much longer than that in FeTPP-300-C at 0.1 V, but shorter at 0.9 V (Figure 4.4c). The shortening of $R_{Fe\text{-}N}$ in PANI-Fe-C with increasing potential suggests that the central Fe^{2+} in PANI-Fe-C is initially out of the plane and moves back towards plane upon the formation of axially bound $O(H)_{ads}$ (Figure 4.4e bottom), contrary to the Fe-N switching behavior observed on FeTPP-300-C (Figure 4.4e top). The value of $R_{Fe\text{-}N}$ in FeTPP-800-C does not change much with potential, remaining mildly larger than that in FeTPP-300-C at 0.1 V. This suggests the minimal structural change during ORR with a mild displacement (Figure 4.4e middle).

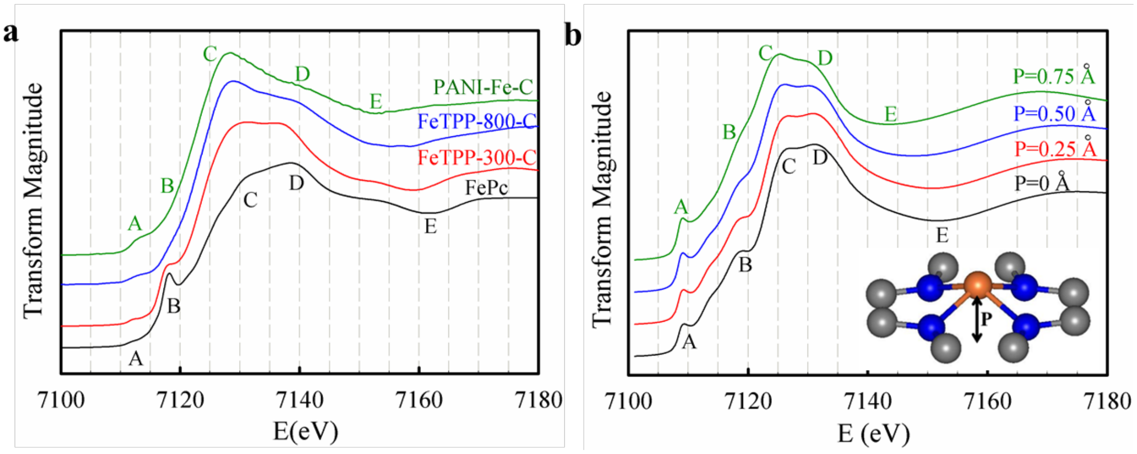

Figure 4.5. a) Catalyst XANES spectra collected at 0.1 V in N_2-saturated 0.1 M $HClO_4$; the XANES of bulk FePc as a square-planar Fe^{2+}-N_4 standard is included. b) XANES spectra calculated by FEFF9 based on the Fe-N_4-C_8 model (inset) with various central Fe displacements (denoted as P). Note the change of the relative intensity of features C and D.

The non-planar Fe-N_x-C structure in pyrolyzed Fe-based catalysts is further substantiated by comparing the experimental XANES data to the theoretical results calculated using the *ab initio* FEFF9. The XANES spectra of all the catalysts at 0.1 V possess the characteristic features (labelled as A-E) of analogue Fe-centered macrocycles (Figure 45),[118,126-128] which are well captured by the multiple scattering FEFF9 calculations based on Fe-N_4-C_x models (Figure 45). All these features exhibit monotonic trends in amplitude and/or position as the catalysts are ordered in the ascending Fe-N bond distance: the intensities of features A and C increase and of features B and D decrease, and feature E shifts toward lower energy. Most interestingly, all these trends can be well reproduced in theoretical XANES by gradually moving the central Fe away from the N_4-plane (Figure 45), and fully accounted for by the distortion of the D_{4h} symmetry and the increase in $R_{Fe\text{-}N}$ as a consequence of the Fe displacement. Specifically, The pre-edge peak A is assigned to an electronic dipole forbidden 1s → 3d transition. This transition is but allowed by the extensive molecular orbital mixing of the iron 3d with the 4p orbitals. Since the mixing is more extensive with less symmetric geometry of iron, the intensity of the peak A increases with decrease in the local symmetry of the central iron.[17,129,130] The features B and C arise from transitions to the lowest unoccupied states that are caused by mixing between the Fe (4s, 4p) and the N (2p) states. Specifically, the shoulder B, which arises from the 1s → $4p_z$ transition with simultaneous ligand to metal charge transfer, has been demonstrated as the fingerprint of the square-planar Fe–N_4 moieties. Any distortion of the symmetry greatly affects the transition. Peak C is due to 1s → $4p_{xy}$ transitions. The shoulder D has been attributed to multiple scattering processes in similar Fe^{2+} complexes, such as the pathway Fe → N → Fe → N', where N and N' are centrosymmetrically located ligands,[118] and shown to be diagnostic of the local structure difference between the Fe^{2+} complexes with different Fe-N bond distances or spin states.[126,128] Finally, the broad feature E arises from scattering processes inside the first coordination shell. Its position is governed by Natoli's rule,[131] $\Delta E \times d^2$ = constant, where ΔE is the energy of the feature E relative to a given zero energy and d is the mean metal–ligand bond length. These features overall are ultrasensitive probes of the electronic configuration and coordination environment of the Fe-based complexes.

All these features exhibit monotonic trends in amplitude and/or position as the catalysts are ordered in the ascending Fe−N bond distance: (i) the amplitude of the pre-edge feature A increases, (ii) the intensity of feature B decreases, (iii) feature C shifts towards lower energies and its amplitude increases, (iv) the amplitude of feature D decreases, and (v) feature E shifts towards lower energies. All these trends can be well reproduced in the theoretical XANES spectra by gradually moving the central Fe away from the N_4−plane (Figure 45), and fully accounted for by the distortion of the D_{4h} symmetry and the increase in R_{Fe-N} as a consequence of the Fe displacement. Specifically, the trends (i) and (ii) are caused by the distortion of the D_{4h} symmetry as a result of the Fe displacement. Trend (iii) can be ascribed to the increase in Fe-N bond length. Specifically, the increase in Fe-N bond length reduces the overlap between the Fe and ligand orbitals. As a result, the Fe orbitals have less ligand character, which leads to an increase in the intensity of the 1s → $4p_{xy}$ transition (feature C). In addition, the increase in Fe-N bond length lowers the energy of the unoccupied Fe(4s,4p)-N(2p) state(s) since the transition involves an antibonding orbital, accounting for the negative shift of feature C. Furthermore, as the Fe-N bong length increases with the Fe displacement, the multiple scattering amplitude reduces, which accounts for the trend (iv). Similar results have been widely reported on similar Fe-based complexes previously.[118,127,128] Trend (v) is directly related to the increase in the Fe-N bond length according to Natoli's rule. That is, the position of feature E relative to the threshold energy (ΔE) is coupled to the mean first shell metal-ligand bond length (R), as governed by Natoli's rule:[131] $\Delta E \times R^2$ = constant. Thus, feature E shifting toward lower energy directly reflects the increase in R_{Fe-N}. Likewise, the comparison of the feature E position in the spectra collected at 0.9 V clearly shows that the $R_{Fe-N/O}$ in FeTPP-800-C and PANI-Fe-C is shorter than in FeTPP-300-C . The excellent agreement between the experimental and theoretical results unambiguously demonstrates the distinct Fe displacement and Fe-N switching behavior presented by the three representative catalysts, and the Fe-N-C active sites formed upon high temperature pyrolysis exhibited distorted Fe-N_x local structures featured with Fe displacements and elongated Fe-N bond distance.

The nature of active sites. By employing the surface sensitive Δμ technique, we showed previously that the active site in FeTPP-300-C in alkaline solution is well represented by a Fe-N_4-C_{12} cluster model inscribed in the original iron-porphyrin macrocycle cavity (denoted hereafter as D2, based on the symbol commonly used in Mössbauer studies[24,25]), while the majority of the active sites in FeTPP-800-C are well represented by an Fe-N_4-C_{10} site with Fe positioned in a C-divacancy in the basal plane and/or an Fe-N_4-C_8 cluster model in the armchair edges of graphitic surfaces (denoted as D1 hereafter).[17] The Δμ signals obtained from FeTPP-300-C and FeTPP-800-C in acid are essentially the same as those obtained in alkaline,[17] indicating similar active sites in different pH environments. The commonality of the role of the active site at the two extreme ends of the pH scale has been extensively discussed in the context of one of the catalysts studied in this work, *i.e.*, FeTPP[17,132] that in both pH environments the reactions meditated by Fe-sites occur through inner-sphere charge transfer process. The Fe-N_4 coordination in FeTPP-300-C and FeTPP-800-C is also supported by EXAFS fits.

Unlike the FeTPP−pyrolyzed catalysts, the PANI−Fe−C exhibits two FT peaks (Figure S1 bottom right) even under *in situ* acidic conditions. The second FT peak at ~ 2.1 Å can be well fitted as a Fe-Fe scattering with a bond length of ~2.54 Å, which is close to the Fe-Fe bond length in bulk iron (2.49 Å) or iron carbide (2.48 Å). Attempts to fit this peak as C, N, O, or S interaction with Fe, gave poorer fits and refinements and led to physically unreasonable coordination, and/or Debye−Waller factors. This indicates that PANI−Fe−C contains some metallic iron that is stable under the acidic environment; this is ascribed to the protection by the surrounding onion-like graphitic carbon nanoshells as directly observed by high-resolution transmission electron microscopy (HRTEM)[5]. Recently it was proposed that the metallic iron encapsulated in carbon nanotubes[39] or graphitic layers[20,93] may be a new active site for ORR, but it is beyond the scope of this work. The Fe−N coordination number (N_{Fe-N} = 3.0) for PANI−Fe−C is a weighted average of the N_{Fe-N} in the Fe−N_x moieties (N_{Fe-N} = x) and in the metallic iron (N_{Fe-N} = 0) owing to the bulk nature of EXAFS, and is thus smaller than x. As the metallic iron content is relatively low as suggested by the small N_{Fe-Fe}, the x is not expected to exceed 3.0 by much, pointing to the Fe−N_4 and/or Fe−N_5 moieties in PANI−Fe−C.

To reveal how D1 is formed in FeTPP catalysts during pyrolysis, the FeTPPCl pyrolyzed at various temperatures has been investigated by combining XAS and rotating disk electrode (RDE) methods. The XANES evolution trend of the FeTPP-pyrolyzed catalysts displayed in Figure 4.6 confirms the Fe displacement increase with increasing pyrolysis temperature, which is expected for increasing D1(non-planar) concentration *vs*. that of the pre-existing D2 (planar) as pyrolysis temperatures are increased. Consistent with the XAS results, square-wave voltammetry profiles of these catalysts (Figure 4.6) show the reduction in the redox peak intensity of D2 at ~0.15 V and the concurrent increase in the redox peak intensity of D1 at ~0.75 V with increasing pyrolysis temperature. The increasing ORR activity trend (Figure 4.6, inset) with increasing D1 content clearly shows that D1 is responsible for the higher activities of these catalysts, despite the co-existence of D1 and D2 sites in the pyrolyzed FeTPP samples. The diminishing of the FT peaks (~2.5 Å) that arise from the carbon atoms in the second shell of the pre-existing macrocycle for FeTPP-800-C (Figure 4.6 3c) suggests that the Fe-N_4 moiety is detached from D2 upon high-temperature treatment, and recaptured at divacant defective centers and/or edge-plane sites on the amorphous carbon support forming D1. The shoulder at 7117 eV (feature B) becomes indiscernible in the XANES of FeTPP-800-C, but is visible in the first derivative of the XANES (Figure 4.6a, inset). This indicates some residual D2 sites in FeTPP-800-C, consistent with the weak redox peak of D2 at ~0.15 V (Figure 4.6c). Further increase of the pyrolysis temperature leads to the decrease of the ORR activity, with the product dominated by inactive metallic iron and/or iron oxides..[17]

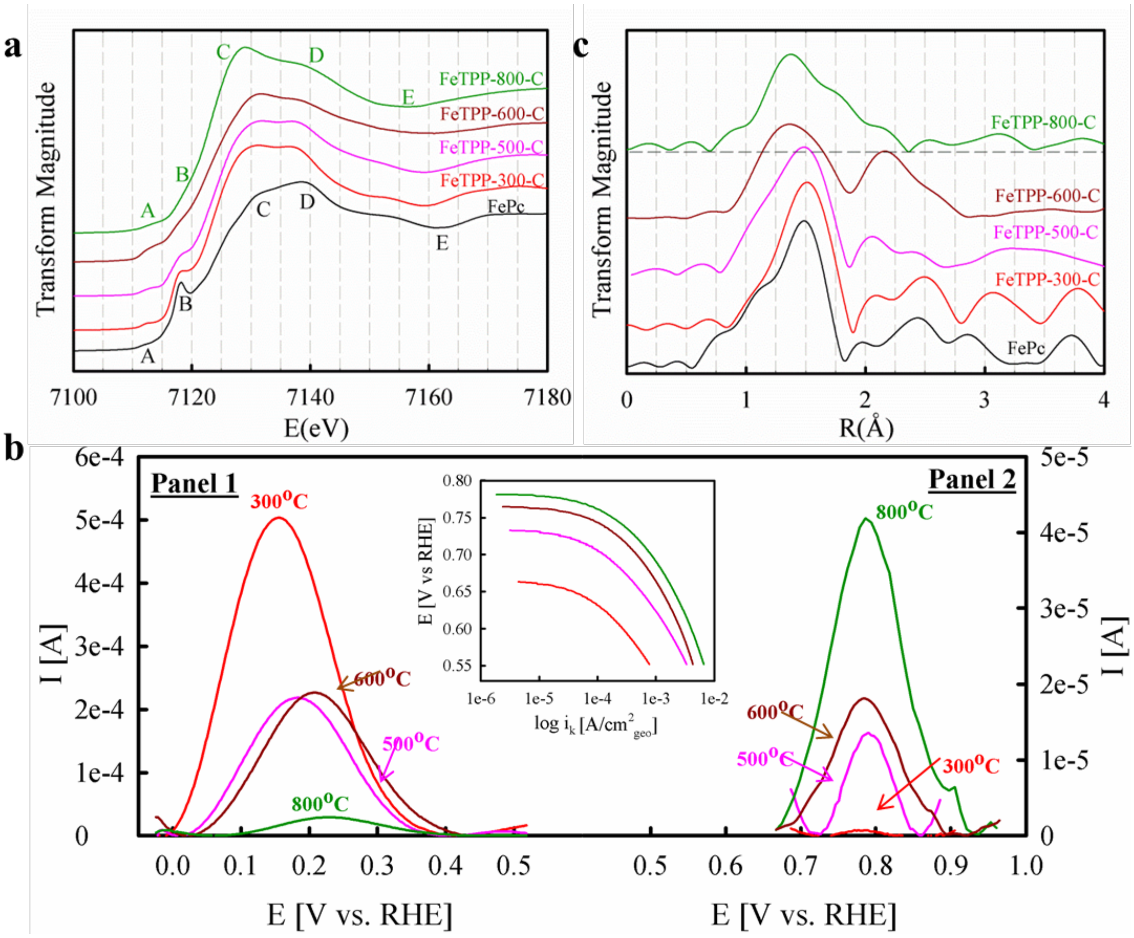

Figure 4.6. The XANES (a) and FT-EXAFS (b) of FeTPP-pyrolyzed dry powders (except for FeTPP-800-C) together with the bulk FePc; the spectra of FeTPP-800-C were collected at 0.1 V in N_2-saturated 0.1 M $HClO_4$ electrolyte. **c,** Square wave voltammetry (SWV) profiles of FeTPP-pyrolyzed catalysts as a function of pyrolysis temperature. All SWV experiments were performed in N_2-saturated 0.1 M $HClO_4$ electrolyte with a step potential

of 5 mV, amplitude of 20 mV, and scan frequency of 10 Hz. Note that the scaling for the left and right current axes is different. The ORR activity trend of the FeTPP-pyrolyzed catalysts is illustrated by the Tafel plots (inset) obtained from RDE experiments in O_2-saturated 0.1 M $HClO_4$ electrolyte at 900 rpm and 20 $mV{\cdot}s^{-1}$ scan rate.

The XAS results are generally consistent with Mössbauer characterization of Fe-macrocycle-pyrolyzed catalysts, which allow for the identification of two types of Fe-N_4 moieties and metallic iron (oxides) in various proportions, depending on the pyrolysis temperature. They are assigned to the square-planar Fe-N_4 in medium-spin state (MS) and low-spin state (LS) in the original macrocycle (D2) and Fe-N_4 embedded in carbon support (D1), respectively.[98,99,108,133] The discrepancy regarding the central Fe position in D1 between the *ex situ* Mössbauer and *in situ* XAS results is likely caused by the structure modifications of the sites upon contact with an electrolyte solution. A recent DFT study[103] suggests that the binding of *OH occurs spontaneously in aqueous environments on an Fe_2N_5 C-edge site, leading to a new active site with higher catalytic activity. Similarly, Yeager *et al.* believed[88] that the active sites are not formed during the heat-treatment of M-N_4 chelates, but upon contact with solutions afterwards.

D1 was also found in PANI-Fe-C[102] and many other Fe-N_x-C catalysts synthesized using individual Fe, N and C precursors,[24,25] but the Fe-N_4 moieties in PANI-Fe-C may also be located in the micropores derived from the highly microporous carbon material, in addition to the edges/defects of graphene sheets. As the average Fe-N bond distance ($R_{Fe\text{-}N}$) in PANI-Fe-C (2.08±0.02 Å) is longer than that in the D1 dominated FeTPP-800-C (2.03±0.02 Å), PANI-Fe-C must contain some Fe-N_x species with the $R_{Fe\text{-}N}$ longer than 2.08 Å. This long Fe-N bond distance is often coupled to a high-spin (HS) Fe^{2+} ion located out of the graphene plane[134] with a fifth axial ligand required for stabilization. Previous Mössbauer studies also suggested a Fe^{2+}(HS)-N_4 site in PANI-Fe-C with the central Fe bonding to axial ligand(s).[102] This structure resembles those of the non-coplanar N_{axi}-Fe^{2+}(HS)-N_4 site in myoglobin[134] or other bio-mimetic catalysts.[135] Interestingly, myoglobin exhibits the same Fe-N switching behavior observed on PANI-Fe-C: the Fe^{2+}-center shifts back toward the plane upon the formation of axially bound species.[134] These results together strongly indicate the existence of the fifth axial ligand at this site despite the lack of direct observation. A similar non-planar NH_2-Fe^{2+}(HS)-N_4 site (denoted as D3) was proposed by Dodelet *et al.* in pyrolyzed Fe-N_x-C catalysts.[25] However, this work provides the first experimental evidence for the substantial Fe^{2+}-center displacement with elongated Fe-N bonds, and strongly suggests the presence of the fifth ligand as the cause of the significant Fe displacement. In addition, we demonstrate that the Fe-N switching behavior of the D3 site during ORR is opposite to that of the pre-existing macrocycle (D2) as represented by FeTPP-300. This accounts primarily for the exceptional inherent activity in terms of turnover frequency (TOF) that far exceeds the TOFs of D1 and D2 sites.[25] Given that FeTPP-800 contains D1 and D2 sites while PANI-Fe-C contains D1 and D3 sites, the superior inherent activity of PANI-Fe-C to that of FeTPP-800 is likely attributed to D3 sites.

Structural origin of enhanced ORR activity. As revealed by the combined *in situ* EXAFS, XANES, and Δμ analysis, all three types of active sites considered undergo the Fe^{2+}/Fe^{3+} redox transition with the denouement of the Fe^{3+} associated with the adsorption of *OH through water activation:

$$N_x\text{-}Fe^{2+} + H_2O \rightarrow N_x\text{-}Fe^{3+}\text{-}OH_{ads} + H^+ + e^- \qquad (4.1)$$

Such transition was previously predicted by Anderson *et al.*[136] as the potential determining step (pds) for Fe-N_4-based sites with a reversible potential (V_{pds}) of 0.64 V based on theoretical computations. The model however was simplistic with Fe-N_4 without any carbon embodiments. The difference between V_{pds} and the ORR reversible potential (1.23 V) represents a thermodynamic overpotential as potentials higher than V_{pds} have a thermodynamic barrier between intermediate reaction states.[137] We show below that the ORR activity of Fe-based catalysts is closely related to the $O(H)_{ads}$ coverage, suggesting that the desorption of oxygenated adsorbates is controlling the overall activity.

The change in $O(H)_{ads}$ coverage on Pt electrodes with applied potential can be best followed by plotting the $\Delta\mu$ magnitude ($|\Delta\mu|$) as a function of potential.[138,139] In the Fe-N_x-C case, the negative dip centered at 7126 eV in the $\Delta\mu$ spectra reflects the charge transfer from the metal center to adsorbed oxygen species.[140] The increase in $|\Delta\mu|$ with increasing potential up to 1.0 V indicates that the Fe^{2+}-sites are progressively occupied by $O(H)_{ads}$ until reaching occupancy saturation at 1.0 V. The relative $O(H)_{ads}$ coverage (Θ_{OH}) at a potential E is thus represented by the ratio of $|\Delta\mu_E|/|\Delta\mu_{1.0V}|$. Potential dependence of Θ_{OH} shown in Figure 4.7a clearly shows that $O(H)_{ads}$ starts to occupy the active sites at potentials far below the ORR onset potential for all considered catalysts (Figure 4.7b), and tracks measured current densities. These results point to a surface redox mediated electrocatalytic process with potential-dependent population of active sites, for which the population of active sites and the reaction rate can be expressed as:[93]

$$N_{active} = N_{total}\frac{1}{1+e^{\frac{F}{RT}(E-E_{redox})}} \tag{4.2}$$

$$\Theta_{O^*} = \frac{N_{total}-N_{active}}{N_{total}} = \frac{1}{1+e^{-\frac{F}{RT}(E-E_{redox})}} \tag{4.3}$$

$$J \propto N_{total}(1-\Theta_{O^*})\exp\left(-\frac{\Delta H^*}{RT}\right)\exp\left(-\frac{E-E^0}{b}\right) \tag{4.4}$$

Where N_{active} and N_{total} are the available and total number of surface active sites, respectively; F is the Faraday constant, R is the universal gas constant; T is the temperature; E is the cathode potential, E_{redox} is the redox potential under the relevant operation conditions, Θ_{O^*} is the coverage by adsorbed oxygen species at potential E; ΔH^* is the activation energy for the electrocatalytic process; E^0 is the standard potential for the faradaic process, and b is the value of the Tafel slope. The general trend between Θ_{OH} and measured current density manifested in Figure 4 .7 illustrates the site blocking effect that lies in the pre-exponential factor ($1-\Theta_{O^*}$) of the rate expression (equation 4). The rising curves of the experimental Θ_{OH}(s) overall follow the theoretical Θ_{OH}(s) derived from equation 3, which suggests that the surface coverage of oxygen species is governed by the cathode potential relative to the redox potential. The gradual slopes observed in experimental $\Theta_{OH}(s)$ implicate multiples types of active sites and/or poor kinetics of the catalysts. Some important conclusions can be derived from the qualitative analysis: (i) the catalytically active sites are Fe^{2+}- N_x rather than Fe^{3+}- N_x sites; (ii) the ORR rate mediated by Fe^{2+}- N_x sites is limited by the removal of oxygen species; (iii) the cathode potential needs to be sufficiently negative to generate enough Fe^{2+}- N_x sites to proceed ORR, accounting for the previously observed strong correlation between the $Fe^{2+/3+}$ redox potential and ORR onset potential[7]; and (iv) positive shift of $Fe^{2+/3+}$ redox potential resulting in stabilization of active Fe^{2+}- N_x sites at elevated potentials, thereby promoting ORR. A quantitative analysis of Θ_{OH} as a function of applied and redox potential on the basis of multiple sites is currently under preparation. This, in addition to the *in situ* real-time XAS measurements of Θ_{OH} at short and long time scales, is expected to give a comprehensive understanding of the nature of various active sites and the structural origins of their activity and durability toward ORR.

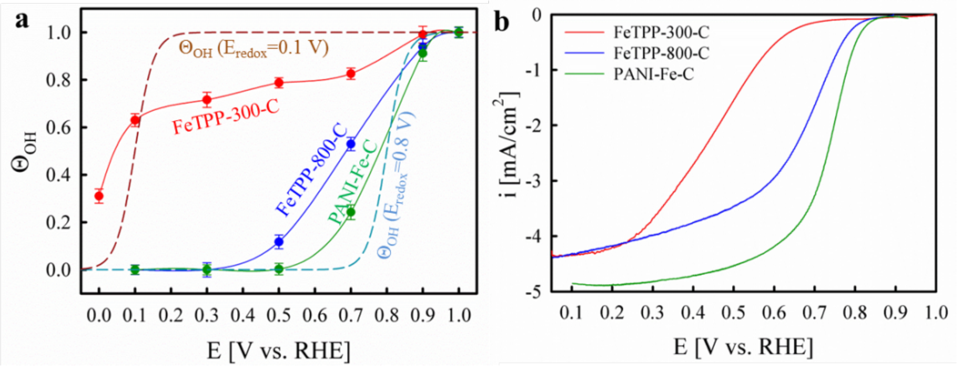

Figure 4.7. a) Experimental Θ_{OH}(s) as a function of potential extracted from the $\Delta\mu$ data, in comparison to the two calculated Θ_{OH}(s) based on equation 3 using the redox potential of 0.05 V or 0.85 V, respectively, and the temperature of 298 K. b) ORR polarization curves obtained in O_2-saturated 0.1 M $HClO_4$ electrolyte at 900 rpm rotation rate and 20 mV·s^{-1} scan rate. Note the ORR polarization curve of PANI-Fe-C presented previously[5] was

obtained using a different testing protocol, and is not identical to that shown here. Vertical error bars in (a) refer to errors involved in determining Θ_{OH} from multiple experimental scans collected at each potential.

Following observation that greater Fe displacement (or longer Fe-N bond) leads to lower $O(H)_{ads}$ coverage and higher ORR activity of studied catalysts, DFT calculations were performed to investigate the effects of the Fe displacement on the electronic property of $Fe\text{-}N_4\text{-}C$ sites and its binding energies with ORR intermediates. The DFT conducted here disregards the solvation and entropic effects but is sufficient for comparing relative activities and predicting limiting steps in the ORR reaction pathway as shown by different research groups.[21,101,103] The different Fe-N switching behaviors exhibited by FeTPP-300-C, FeTPP-800-C, and PANI-Fe-C are nicely reproduced by $Fe\text{-}N_4\text{-}C_{12}$ (D2), $Fe\text{-}N_4\text{-}C_{10}$ (D1), and $N_{axi}\text{-}Fe\text{-}N_4\text{-}C_8$ (D3) models, respectively (Figure 4.2 and Table 4.1). The over-binding of $O(H)_{ads}$ on the three sites as suggested by the experimental results is manifested by their free energy diagrams. Most importantly, the addition of an axial NH_2 ligand to the $Fe\text{-}N_4\text{-}C_8$ model (forming $N_{axi}\text{-}Fe\text{-}N_4\text{-}C_8$) results in the reverse of the Fe-N switching behavior, and the decrease of the binding energies of ORR intermediates (Table 4.2), thereby drastically increasing the ORR activity as manifested by the calculated reaction pathways (Figure 4.8a). Correspondingly, the V_{pds} is significantly increased from -0.18 to 0.73 V, close to the highest calculated value (0.80 V) of V_{pds} for any non-PGM catalyst structure to date.[103] Once the applied potential exceeds the V_{pds}, water activation (equation 1) becomes downhill in energy or exothermic (Figure 4.8b), and the produced oxygen species poison the surface $Fe^{2+}\text{-}N_x$ active sites. This agrees with the experimental observation of the adsorption of *OH from water activation triggered by Fe^{2+}/Fe^{3+} redox transition. In accordance with our results, the record high V_{pds} obtained on the $FeCoN_5$(*OH) site is essentially triggered by the binding of an *OH as a fifth ligand onto $FeCoN_5$, which decreases subsequent binding energies of ORR intermediates.[103] Our DFT calculations also agree with the experimental results reported by Cao *et al.*,[135] which show that the FePc anchored on pyridine-functionalized carbon nanotubes (FePc–Py–CNTs) featured with the $NH_2\text{-}Fe\text{-}N_4$ structure exhibits much higher ORR activity as compared with the FePc directly anchored on CNTs (FePc-CNTs) featured with in-plane $Fe\text{-}N_4$ structure. In addition to optimizing the binding energies of ORR intermediates, the Fe displacement induced by the fifth axial ligand may facilitate O_2 adsorption *via* reducing the number of d_{z^2}-electrons of the central Fe (Figure 4.3), given that the completely filled d_{z^2} orbital of D2 prevents the end-on adsorption of molecular oxygen.[25]

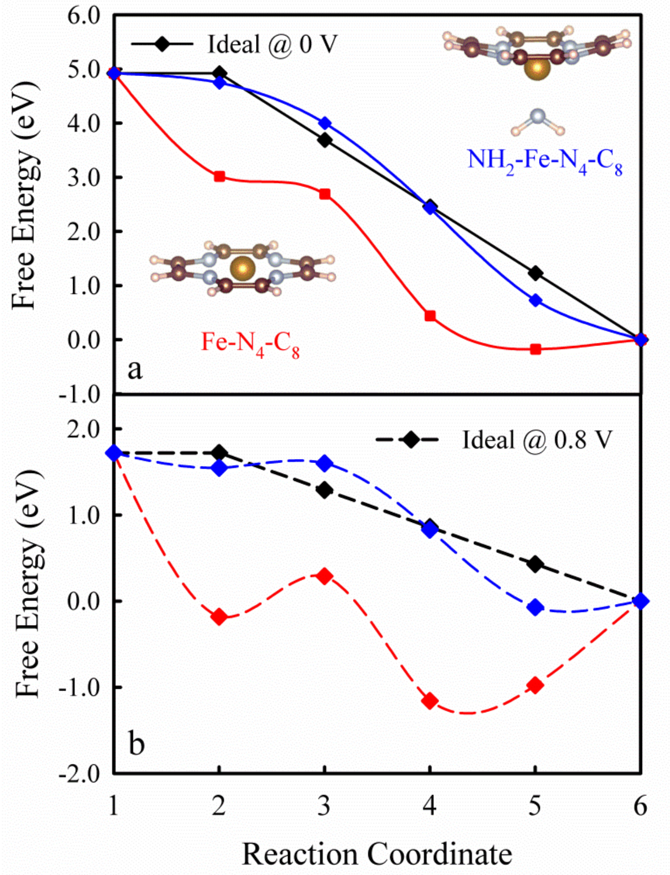

Figure 4.8. Reaction coordinates correspond to the given systems: (1) $* + O_2 + 4H^+ + 4e^-$, (2) $*OO + 4H^+ + 4e^-$, (3) $*OOH + 3H^+ + 3e^-$, (4) $*O + 2H^+ + 2e^- + H_2O$, (5) $*OH + H^+ + e^- + H_2O$, (6) $* + 2H_2O$ at potential of 0 V (a) and 0.8 V (b) relative to the computational[41] hydrogen electrode. The ideal pathway (shown in black) gives a flat line at 1.23 V, the ORR reversible potential. The Fe, N, C, and H atoms are represented by yellow, blue, brown, and white spheres, respectively.

Therefore, one way to increase the ORR activity of iron-based catalysts is to selectively yield the D3 site. However, neither the formation mechanism of the D3 site nor the nature of the fifth axial ligand in the D3 site is clear. Given the 3-

dimentional nature of this site and the absence of this site in Fe-macrocycle-pyrolyzed catalysts, it is inferred that the D3 site resides in 3-dimentional micropores derived from the highly microporous carbon material (PANI here), and the D3 content increases with increase of the 3-D micropore population. A plausible evidence of this hypothesis is that the D3 content in the Fe-N_x-C catalyst was significantly increased by replacing the Black Pearls 2000 to zeolitic-imidazolate-framework enriched with 3D micropores, with a consequence of ORR activity increase.[3,28] In addition, prior report by Holby *et al.,*[103] using DFT calculations suggests that the *OH may serve as a fifth ligand responsible for the displacement of the central Fe thereby accounts for the higher ORR rate. The clarification of the fifth axial ligand may advance the development of non-PGM catalysts and the fundamental understanding of the ORR kinetics mediated by metal-nitrogen coordinate centers.

In conclusion, we show that the new active sites (D1 and D3) in pyrolyzed Fe-N_x-C catalysts exhibit distinctly different Fe displacements and Fe-N switching behaviors during ORR from the original Fe-N_4 macrocycle (D2), which accounts for their enhanced ORR activity. The new principles linking the dynamic structure of M-N_x-C sites during chemical reactions to catalytic activity are expected to be applicable to a broad variety of transition-metal compounds such as oxides, nitrides, chalcogenides, and metalloporphyrins, and potentially guide rational design of these non-PGM materials for broad applications.

Sumamry

The objective of this multi-institutional effort was to comprehensively pursue the goal of eliminating noble metal (Pt group metals, PGM) from the cathodic oxygen reduction reaction (ORR) electrode thereby providing a quantum leap in lowering the overall PGM loading in a polymer electrolyte fuel cell (PEMFC). The overall project scope encompassed (a) comprehensive materials discovery effort, (b) a concomitant effort to scale up these materials with very high (± 5%) reproducibility, both intra and inter, (c) understanding mass transport in porous medium both in gas diffusion and micro-porous layers for enhanced areal activity, (d) understanding mechanistic aspects of active site structure and ORR electrocatalytic pathway.

Overall project milestones and metrics were (a) first phase effort based on performance in oxygen where the project's Go/No-Go decision point milestone of 100 mA/cm^2 at 0.8 V (internal resistance-free, iR-free) at 80^{o}C, pure H_2/O_2, with 1.5 bar total pressure was met. Subsequently, the principle objectives were to (a) transition the project from H_2/O_2 to H_2/Air with slated target of exceeding 30 mA/cm^2 @ 0.8 V, 2.5 bar total pressure and an end of the project target of 1 A/cm^2 @ 0.4 V (same total pressure), both under 100% relative humidity. The target for catalyst material scale up was to achieve 100 g batch size at the end of the program. This scale up target had a quality control milestone of less than 5% variation of activity measured with H_2/Air (2.5 bar total pressure) at 0.8 V. In addition, the project also aimed at arriving at a unified understanding of the nature of active sites in these catalysts as well as some preliminary understanding of the mechanistic pathway. Also addressed is the development of an integrated method for determination of mass transport parameters using a combination of Helox experiments and modeling of the gas diffusion media, especially the micro-porous layer on the gas diffusion electrode (GDE). Detailed aspects of technical metrics and milestones are provided in Table 1 of the final report.

Besides the success in meeting the DOE milestones in areal activities for oxygen and air described above one of the key successes of this effort was in understanding the nature of the active site(s) and aspects of the ORR pathway. In this it should be noted that the materials discovery effort provided for use of unconventional approaches, some of which led to very active catalysts. This aspect is described in detail in the final report. From a mechanistic perspective, a combination spectroscopic techniques confirmed that the high activity observed for most pyrolyzed Fe-based catalysts, irrespective of the precursors materials (macrocycles or individual Fe, N, and C precursors), the synthesis method (wet chemical impregnation or SSM), and final Fe-species (with or without inorganic iron species), can mainly be attributed to a single active site: non-planar Fe-N_4 moiety embedded in distorted carbon matrix characterized by a high potential for the $Fe^{2+/3+}$ redox transition in acidic electrolyte/environment, which is likely formed via the covalent incorporation of distorted Fe-N_4 moieties in the defective centers on the carbon basal plane or in armchair edges of two adjacent graphene layers. This Fe^{2+}-N_4

active site at 0.3 V undergoes redox transition to a pentacoordinate HO−Fe^{3+}−N_4 at 0.90 V, and the adsorption of the *OH trigged by the Fe^{2+}/Fe^{3+} redox transition poisons the active sites, thereby providing experimental evidence of the redox mechanism. Moreover, a highly active MOF-based catalyst devoid of any Fe-N moieties was also developed, and the active sites were identified as nitrogen-doped carbon fibers with embedded iron particles that are not directly involved in the oxygen reduction pathway. The high ORR activity and durability of catalysts involving this site in fuel cells are attributed to the high density of active sites and the elimination or reduction of Fenton-type processes. The latter are initiated by hydrogen peroxide but are known to be accelerated by iron ions exposed to the surface, resulting in the formation of damaging free-radicals. We expect that the comprehensive understanding of the synthesis-products correlations, nature of active sites, and the reaction mechanisms acquired here by systematically studying a broad variety of M-N-C materials under *in situ* conditions will provide guidelines to rational design of this type of non-PGM catalysts.

Conclusions

This multi-institutional effort combined the expertise of Northeastern University (NEU) (Lead institution) [electrocatalysis, In situ spectroscopy and fuel cell Polarization tests], University of New Mexico (UNM) [electrocatayst materials, scale up, ex situ characterizations], Michigan State University (MSU) [Modeling of mass transport processes], Pajarito Powders (PPC) [electrocatalyst scale up and fuel cell performance validation] and Nissan Technical Center North America (NTCNA) [validation of fuel cell performance under automotive conditions]. The overall goal of this project was to provide a comprehensive effort to develop scalable cathode catalysts for oxygen reduction reaction (ORR) possessing no noble metals (non Pt group metals, non PGM). Approach involved comprehensive materials discovery effort leading to scale up, development of porous medium for efficient mass transport supported by fuel cell polarization studies and mass transport modeling and detailed insight on the nature of the active site for ORR and elucidation of ORR electrocatalytic pathways.

Materials discovery effort lead to two approaches which provided for high performance meeting DOE milestones in H_2/O_2 (i.e., 100 mA/cm^2 at 0.8 V, 1.5 bar total pressure) and H_2/Air (30 mA/cm^2 at 0.8 V and 1 A/cm^2 at 0.4 V, 2.5 bar total pressure). These included (a) the sacrificial support method (SSM) developed by UNM involving Si micro-spheres which served as a template for carbon incorporating diverse approaches such as the micromechanical method using organic salt precursors (i.e., Nicarbazin) or nitrogen chelated moieties (such as amino-antipyrene). (b) An alternative approach involved metal organic framework (MOF) precursors developed by NEU provided for unprecedented ability to control the nature of active sites. Detailed mass transport measurements were conducted at NEU using an experimental protocol in association with single PEM cell polarization measurements referred to as ‘Helox’ method. Here careful control of oxygen partial pressure and use of various concomitant carrier gases were employed to determine mass transport parameters. In additional protocol developed by MSU using rotating disk electrode (RDE) measurements provided for a careful sensitivity analysis on the effect various parameters such as ionomer loading, binder concentration, porosity of the micro-porous layer etc. This analysis and feedback provided for areal activity in air to meet and exceed DOE milestone and go/no go decision point.

In addition, detailed spectroscopy using a combination of in situ synchrotron x-ray absorption, ex situ XPS and Mossbauer provided detailed insight on the nature of the ORR active site and the role of Fe-N coordination and spatial structure in determining relative onset potential of ORR and its turnover number. ORR activity was ascribed to depend on (a) Fe^{2+}/Fe^{3+} redox potential, (b) the nature of the Fe-

N coordination with the most active site being in D3 configuration (c) Fe switching behavior with potential providing the important driving force for the four electron reduction.

All active materials developed in this effort was scaled up to levels ranging from 30-300 g batch by PPC. In addition, protocols for making electrodes and MEAs were developed by PPC and NEU. Its validation and testing of performance was conducted both at NTCNA and PPC.

Publications and Patents

Leonard, N. D.; Artyushkova, K.; Halevi, B.; Serov, A.; Atanassov, P.; Barton, S. C. *Journal of The Electrochemical Society* **2015**, *162*, F1253.

Leonard, N. D. & Barton, S. C. Analysis of Adsorption Effects on a Metal-Nitrogen-Carbon Catalyst Using a Rotating Ring-Disk Study. *Journal of The Electrochemical Society* 161, H3100-H3105 (2015).

Kabir, S.; Artyushkova, K.; Kiefer, B.; Atanassov, P. Computational and experimental evidence for a new TM-N3/C moiety family in non-PGM electrocatalysts. *Phys. Chem. Chem. Phys.* **2015**, 17, 17785-17789.

Jia, Q.; Ramaswamy, N.; Hafiz, H.; Tylus, U.; Strickland, K.; Wu, G.; Barbiellini, B.; Bansil, A.; Holby, E. F.; Zelenay, P.; Mukerjee, S. Experimental Observation of Redox-Induced Fe–N Switching Behavior as a Determinant Role for Oxygen Reduction Activity. *ACS Nano* **2015**, 9, 12496-12505.

Strickland, K.; Miner, E.; Jia, Q.; Tylus, U.; Ramaswamy, N.; Liang, W.; Sougrati, M.-T.; Jaouen, F.; Mukerjee, S. Highly active oxygen reduction non-platinum group metal electrocatalyst without direct metal-nitrogen coordination. *Nat Commun* **2015**, 6.

Serov, A., Artyushkova, K., Andersen, N. I., Stariha, S. & Atanassov, P. Original Mechanochemical Synthesis of Non-Platinum Group Metals Oxygen Reduction Reaction Catalysts Assisted by Sacrificial Support Method. *Electrochimica Acta* (**2015**).

Serov, A.; Tylus, U.; Artyushkova, K.; Mukerjee, S.; Atanassov, P. Mechanistic studies of oxygen reduction on Fe-PEI derived non-PGM electrocatalysts. *Applied Catalysis B: Environmental* **2014**, 150–151, 179-186.

Tylus, U.; Jia, Q.; Strickland, K.; Ramaswamy, N.; Serov, A.; Atanassov, P.; Mukerjee, S. Elucidating Oxygen Reduction Active Sites in Pyrolyzed Metal–Nitrogen Coordinated Non-Precious-Metal Electrocatalyst Systems. *The Journal of Physical Chemistry C* **2014**, 118, 8999-9008.

Ganesan, S., Leonard, N. & Barton, S. C. Impact of transition metal on nitrogen retention and activity of iron–nitrogen–carbon oxygen reduction catalysts. *Physical Chemistry Chemical Physics* 16, 4576-4585 (**2014**).

Robson, M. H., Artyushkova, K., Patterson, W., Atanassov, P. & Hibbs, M. R. Non-platinum Carbon-Supported Oxygen Reduction Catalyst Ink Evaluation Based on Poly (sulfone) and Poly (phenylene)-Derived Ionomers in Alkaline Media. *Electrocatalysis* 5, 148-158 (**2014**).

Serov, A., Artyushkova, K. & Atanassov, P. Fe-N-C Oxygen Reduction Fuel Cell Catalyst Derived from Carbendazim: Synthesis, Structure, and Reactivity. *Advanced Energy Materials* 4 (**2014**).

Serov, A., Tylus, U., Artyushkova, K., Mukerjee, S. & Atanassov, P. Mechanistic studies of oxygen reduction on Fe-PEI derived non-PGM electrocatalysts. *Applied Catalysis B: Environmental* 150, 179-186 (**2014**).

Ramaswamy, N.; Tylus, U.; Jia, Q.; Mukerjee, S. Activity Descriptor Identification for Oxygen Reduction on Nonprecious Electrocatalysts: Linking Surface Science to Coordination Chemistry. *Journal of the American Chemical Society* **2013**, 135, 15443-15449.

Serov, A.; Robson, M. H.; Smolnik, M.; Atanassov, P. Templated bi-metallic non-PGM catalysts for oxygen reduction. *Electrochimica Acta* **2012**, 80, 213-218.

Patents:

1. Patterson, W., Artyushkova, K. D., Halevi, B., Robson, M. H., Serov, A., Walker, C., and Atanassov, P., *'Structured Cathode Catalysts for Fuel Cell Application Derived from Metal-Nitrogen-Carbon Precursors',* (US Patent 20,140,349,843, 2014).
2. A. Serov, Kateryna D. Artyushkova, Barr Halevi, Michael H. Robson, Wendy Patterson and Plamen B. Atanassov "*Cathode Catalysts for Fuel Cell Application Derived from Polymer Precursors*", Appl. Number: 2011-103, Appl. Date: May 9, 2011
3. A. Serov, Kateryna D. Artyushkova, Barr Halevi and Plamen B. Atanassov "*Non-PGM Cathode Catalysts for Fuel Cell Application Derived from Heat Treated Heteroatomic Amines Precursors*", Appl. Number: 2011-107, Appl. Date: May 16, 2011
4. Mukerjee, S., Sgtrickland K., Tylus, Q., '*Non Noble Metal Electrocatalysts for Oxygen Depolarized Cathodes and Their Uses*' PCT/US14/10502.

References

(1) Shao, Y.; Yin, G.; Wang, Z.; Gao, Y. Proton exchange membrane fuel cell from low temperature to high temperature: Material challenges. *Journal of Power Sources* **2007**, 167, 235-242.
(2) Jasinski, R. Cobalt Phthalocyanine as a Fuel Cell Cathode. *Journal of The Electrochemical Society* **1965**, 112, 526-528.
(3) Collman, J. P.; Denisevich, P.; Konai, Y.; Marrocco, M.; Koval, C.; Anson, F. C. Electrode catalysis of the four-electron reduction of oxygen to water by dicobalt face-to-face porphyrins. *Journal of the American Chemical Society* **1980**, 102, 6027-6036.
(4) Chang, C. J.; Loh, Z.-H.; Shi, C.; Anson, F. C.; Nocera, D. G. Targeted Proton Delivery in the Catalyzed Reduction of Oxygen to Water by Bimetallic Pacman Porphyrins. *Journal of the American Chemical Society* **2004**, 126, 10013-10020.
(5) Wu, G.; More, K. L.; Johnston, C. M.; Zelenay, P. High-Performance Electrocatalysts for Oxygen Reduction Derived from Polyaniline, Iron, and Cobalt. *Science* **2011**, 332, 443-447.
(6) Ghiladi, M.; J. McKenzie, C.; Meier, A.; K. Powell, A.; Ulstrup, J.; Wocadlo, S. Dinuclear iron(III)-metal(II) complexes as structural core models for purple acid phosphatases [dagger]. *Journal of the Chemical Society, Dalton Transactions* **1997**, 4011-4018.
(7) Southon, P. D.; Price, D. J.; Nielsen, P. K.; McKenzie, C. J.; Kepert, C. J. Reversible and Selective O2 Chemisorption in a Porous Metal–Organic Host Material. *Journal of the American Chemical Society* **2011**, 133, 10885-10891.
(8) Carmo, M.; Linardi, M.; Poco, J. G. R. Characterization of nitric acid functionalized carbon black and its evaluation as electrocatalyst support for direct methanol fuel cell applications. *Applied Catalysis A: General* **2009**, 355, 132-138.
(9) Paulus, U. A.; Schmidt, T. J.; Gasteiger, H. A.; Behm, R. J. Oxygen reduction on a high-surface area Pt/Vulcan carbon catalyst: a thin-film rotating ring-disk electrode study. *Journal of Electroanalytical Chemistry* **2001**, 495, 134-145.
(10) Arruda, T. M.; Shyam, B.; Lawton, J. S.; Ramaswamy, N.; Budil, D. E.; Ramaker, D. E.; Mukerjee, S. Fundamental Aspects of Spontaneous Cathodic Deposition of Ru onto Pt/C Electrocatalysts and Membranes under Direct Methanol Fuel Cell Operating Conditions: An in Situ X-ray Absorption Spectroscopy and Electron Spin Resonance Study. *The Journal of Physical Chemistry C* **2009**, 114, 1028-1040.
(11) Newville, M. IFEFFIT : Interactive XAFS Analysis and FEFF Fitting. *Journal of Synchrotron Radiation* **2001**, 8, 322-324.
(12) Ravel, B.; Newville, M. ATHENA and ARTEMIS: interactive graphical data analysis using IFEFFIT. *Physica Scripta* **2005**, 2005, 1007.
(13) Zabinsky, S. I.; Rehr, J. J.; Ankudinov, A.; Albers, R. C.; Eller, M. J. Multiple-scattering calculations of x-ray-absorption spectra. *Physical Review B* **1995**, 52, 2995-3009.
(14) Jiang, R.; Anson, F. C. The origin of inclined plateau currents in steady-state voltammograms for electrode processes involving electrocatalysis. *Journal of Electroanalytical Chemistry and Interfacial Electrochemistry* **1991**, 305, 171-184.
(15) Bonnecaze, R. T.; Mano, N.; Nam, B.; Heller, A. On the Behavior of the Porous Rotating Disk Electrode. *Journal of The Electrochemical Society* **2007**, 154, F44-F47.
(16) Yeager, E. Electrocatalysts for O2 reduction. *Electrochimica Acta* **1984**, 29, 1527-1537.
(17) Ramaswamy, N.; Tylus, U.; Jia, Q.; Mukerjee, S. Activity Descriptor Identification for Oxygen Reduction on Nonprecious Electrocatalysts: Linking Surface Science to Coordination Chemistry. *Journal of the American Chemical Society* **2013**, 135, 15443-15449.
(18) Lefèvre, M.; Proietti, E.; Jaouen, F.; Dodelet, J.-P. Iron-based catalysts with improved oxygen reduction activity in polymer electrolyte fuel cells. *Science* **2009**, 324, 71-74.
(19) Proietti, E.; Jaouen, F.; Lefèvre, M.; Larouche, N.; Tian, J.; Herranz, J.; Dodelet, J.-P. Iron-based cathode catalyst with enhanced power density in polymer electrolyte membrane fuel cells. *Nature Communication* **2011**, 2, 416.

(20) Strickland, K.; Miner, E.; Jia, Q.; Tylus, U.; Ramaswamy, N.; Liang, W.; Sougrati, M.-T.; Jaouen, F.; Mukerjee, S. Highly active oxygen reduction non-platinum group metal electrocatalyst without direct metal-nitrogen coordination. *Nat Commun* **2015**, 6.
(21) Zitolo, A.; Goellner, V.; Armel, V.; Sougrati, M.-T.; Mineva, T.; Stievano, L.; Fonda, E.; Jaouen, F. Identification of catalytic sites for oxygen reduction in iron- and nitrogen-doped graphene materials. *Nat Mater* **2015**, 14, 937-942.
(22) Falase, A.; Main, M.; Garcia, K.; Serov, A.; Lau, C.; Atanassov, P. Electrooxidation of ethylene glycol and glycerol by platinum-based binary and ternary nano-structured catalysts. *Electrochimica Acta* **2012**, 66, 295-301.
(23) Zalineeva, A.; Serov, A.; Padilla, M.; Martinez, U.; Artyushkova, K.; Baranton, S.; Coutanceau, C.; Atanassov, P. B. Self-Supported PdxBi Catalysts for the Electrooxidation of Glycerol in Alkaline Media. *Journal of the American Chemical Society* **2014**, 136, 3937-3945.
(24) Kramm, U. I.; Lefèvre, M.; Larouche, N.; Schmeisser, D.; Dodelet, J.-P. Correlations between mass activity and physicochemical properties of Fe/N/C catalysts for the ORR in PEM fuel cell via 57Fe mössbauer spectroscopy and other techniques. *J. Am. Chem. Soc.* **2013**, 136, 978-985.
(25) Kramm, U. I.; Herranz, J.; Larouche, N.; Arruda, T. M.; Lefevre, M.; Jaouen, F.; Bogdanoff, P.; Fiechter, S.; Abs-Wurmbach, I.; Mukerjee, S.; Dodelet, J.-P. Structure of the catalytic sites in Fe/N/C-catalysts for O2-reduction in PEM fuel cells. *Phys. Chem. Chem. Phys.* **2012**, 14, 11673-11688.
(26) Serov, A.; Tylus, U.; Artyushkova, K.; Mukerjee, S.; Atanassov, P. Mechanistic studies of oxygen reduction on Fe-PEI derived non-PGM electrocatalysts. *Applied Catalysis B: Environmental* **2014**, 150–151, 179-186.
(27) Serov, A.; Robson, M. H.; Smolnik, M.; Atanassov, P. Templated bi-metallic non-PGM catalysts for oxygen reduction. *Electrochimica Acta* **2012**, 80, 213-218.
(28) Jaouen, F.; Herranz, J.; Lefèvre, M.; Dodelet, J.-P.; Kramm, U. I.; Herrmann, I.; Bogdanoff, P.; Maruyama, J.; Nagaoka, T.; Garsuch, A.; Dahn, J. R.; Olson, T.; Pylypenko, S.; Atanassov, P.; Ustinov, E. A. Cross-Laboratory Experimental Study of Non-Noble-Metal Electrocatalysts for the Oxygen Reduction Reaction. *ACS Applied Materials & Interfaces* **2009**, 1, 1623-1639.
(29) Gong, K.; Du, F.; Xia, Z.; Durstock, M.; Dai, L. Nitrogen-Doped Carbon Nanotube Arrays with High Electrocatalytic Activity for Oxygen Reduction. *Science* **2009**, 323, 760-764.
(30) Zhang, L.; Mukerjee, S. Investigation of Durability Issues of Selected Nonfluorinated Proton Exchange Membranes for Fuel Cell Application. *Journal of The Electrochemical Society* **2006**, 153, A1062-A1072.
(31) Kramm, U. I.; Lefèvre, M.; Larouche, N.; Schmeisser, D.; Dodelet, J.-P. Correlations between Mass Activity and Physicochemical Properties of Fe/N/C Catalysts for the ORR in PEM Fuel Cell via 57Fe Mössbauer Spectroscopy and Other Techniques. *Journal of the American Chemical Society* **2014**, 136, 978-985.
(32) Ruskov, T.; Asenov, S.; Spirov, I.; Garcia, C.; Mönch, I.; Graff, A.; Kozhuharova, R.; Leonhardt, A.; Mühl, T.; Ritschel, M. Mössbauer transmission and back scattered conversion electron study of Fe nanowires encapsulated in multiwalled carbon nanotubes. *Journal of applied physics* **2004**, 96, 7514-7518.
(33) Miyatani, R.; Yamada, Y.; Kobayashi, Y. Mössbauer study of iron carbide nanoparticles produced by sonochemical synthesis. *Journal of Radioanalytical and Nuclear Chemistry* **2014**, 303, 1503-1506.
(34) Borsa, D. M.; Boerma, D. O. Phase identification of iron nitrides and iron oxy-nitrides with Mössbauer spectroscopy. *Hyperfine Interactions*, 151, 31-48.
(35) Wang, L.; Yin, J.; Zhao, L.; Tian, C.; Yu, P.; Wang, J.; Fu, H. Ion-exchanged route synthesis of Fe2N-N-doped graphitic nanocarbons composite as advanced oxygen reduction electrocatalyst. *Chemical Communications* **2013**, 49, 3022-3024.
(36) Koslowski, U. I.; Abs-Wurmbach, I.; Fiechter, S.; Bogdanoff, P. Nature of the Catalytic Centers of Porphyrin-Based Electrocatalysts for the ORR: A Correlation of Kinetic Current Density with the Site Density of Fe−N4 Centers. *The Journal of Physical Chemistry C* **2008**, 112, 15356-15366.
(37) Jaouen, F. In *Non-Noble Metal Fuel Cell Catalysts*; Wiley-VCH Verlag GmbH & Co. KGaA: **2014**, p. 29-118.
(38) Banks, C. E.; Davies, T. J.; Wildgoose, G. G.; Compton, R. G. Electrocatalysis at graphite and carbon nanotube modified electrodes: edge-plane sites and tube ends are the reactive sites. *Chemical Communications* **2005**, 829-841.

(39) Deng, D.; Yu, L.; Chen, X.; Wang, G.; Jin, L.; Pan, X.; Deng, J.; Sun, G.; Bao, X. Iron Encapsulated within Pod-like Carbon Nanotubes for Oxygen Reduction Reaction. *Angewandte Chemie International Edition* **2013**, 52, 371-375.
(40) Tylus, U.; Jia, Q.; Strickland, K.; Ramaswamy, N.; Serov, A.; Atanassov, P.; Mukerjee, S. Elucidating Oxygen Reduction Active Sites in Pyrolyzed Metal–Nitrogen Coordinated Non-Precious-Metal Electrocatalyst Systems. *The Journal of Physical Chemistry C* **2014**, 118, 8999-9008.
(41) Gasteiger, H. A.; Kocha, S. S.; Sompalli, B.; Wagner, F. T. Activity benchmarks and requirements for Pt, Pt-alloy, and non-Pt oxygen reduction catalysts for PEMFCs. *Applied Catalysis B: Environmental* **2005**, 56, 9-35.
(42) Weber, A. Z.; Darling, R. M.; Newman, J. Modeling Two-Phase Behavior in PEFCs. *Journal of The Electrochemical Society* **2004**, 151, A1715-A1727.
(43) Gostick, J. T.; Ioannidis, M. A.; Fowler, M. W.; Pritzker, M. D. Pore network modeling of fibrous gas diffusion layers for polymer electrolyte membrane fuel cells. *Journal of Power Sources* **2007**, 173, 277-290.
(44) Eikerling, M.; Kornyshev, A. A. Modelling the performance of the cathode catalyst layer of polymer electrolyte fuel cells. *Journal of Electroanalytical Chemistry* **1998**, 453, 89-106.
(45) El Hannach, M.; Pauchet, J.; Prat, M. Pore network modeling: Application to multiphase transport inside the cathode catalyst layer of proton exchange membrane fuel cell. *Electrochimica Acta* **2011**, 56, 10796-10808.
(46) Liu, J.; Eikerling, M. Model of cathode catalyst layers for polymer electrolyte fuel cells: The role of porous structure and water accumulation. *Electrochimica Acta* **2008**, 53, 4435-4446.
(47) Eikerling, M. Water Management in Cathode Catalyst Layers of PEM Fuel Cells: A Structure-Based Model. *Journal of The Electrochemical Society* **2006**, 153, E58-E70.
(48) Adamson, A. W.; Gast, A. P. *Physical chemistry of surfaces*; Wiley: New York [u.a.], 1997.
(49) Weber, A. Z.; Newman, J. Transport in Polymer-Electrolyte Membranes: III. Model Validation in a Simple Fuel-Cell Model. *J. Electrochem. Soc.* **2004**, 151, A326-A339.
(50) Janssen, G. J. M. A Phenomenological Model of Water Transport in a Proton Exchange Membrane Fuel Cell. *J. Electrochem. Soc.* **2001**, 148, A1313-A1323.
(51) Weber, A. Z.; Newman, J. Transport in polymer-electrolyte membranes II. mathematical model. *J. Electrochem. Soc.* **2004**, 151, A311-A325.
(52) Weber, A. Z.; Newman, J. Modeling Transport in Polymer-Electrolyte Fuel Cells. *Chem. Rev.* **2004**, 104, 4679-4726.
(53) Das, P. K.; Li, X.; Liu, Z.-S. Effective transport coefficients in PEM fuel cell catalyst and gas diffusion layers: Beyond Bruggeman approximation. *Applied Energy* **2010**, 87, 2785-2796.
(54) Weber, A. Z.; Borup, R. L.; Darling, R. M.; Das, P. K.; Dursch, T. J.; Gu, W.; Harvey, D.; Kusoglu, A.; Litster, S.; Mench, M. M.; Mukundan, R.; Owejan, J. P.; Pharoah, J. G.; Secanell, M.; Zenyuk, I. V. A Critical Review of Modeling Transport Phenomena in Polymer-Electrolyte Fuel Cells. *J. Electrochem. Soc.* **2014**, 161, F1254-F1299.
(55) Uchida, M.; Fukuoka, Y.; Sugawara, Y.; Eda, N.; Ohta, A. Effects of Microstructure of Carbon Support in the Catalyst Layer on the Performance of Polymer-Electrolyte Fuel Cells. *J. Electrochem. Soc.* **1996**, 143, 2245-2252.
(56) Eastman, S. A.; Kim, S.; Page, K. A.; Rowe, B. W.; Kang, S.; Soles, C. L.; Yager, K. G. Effect of Confinement on Structure, Water Solubility, and Water Transport in Nafion Thin Films. *Macromolecules* **2012**, 45, 7920-7930.
(57) Dishari, S. K.; Hickner, M. A. Confinement and Proton Transfer in NAFION Thin Films. *Macromolecules* **2013**, 46, 413-421.
(58) Kusoglu, A.; Kushner, D.; Paul, D. K.; Karan, K.; Hickner, M. A.; Weber, A. Z. Impact of Substrate and Processing on Confinement of Nafion Thin Films. *Adv. Funct. Mater.* **2014**, 24, 4763-4774.
(59) Yoon, W.; Weber, A. Z. Modeling Low-Platinum-Loading Effects in Fuel-Cell Catalyst Layers. *J. Electrochem. Soc.* **2011**, 158, B1007-B1018.
(60) Pollard, W. G.; Present, R. D. On Gaseous Self-Diffusion in Long Capillary Tubes. *Physical Review* **1948**, 73, 762-774.
(61) Becker, J.; Wieser, C.; Fell, S.; Steiner, K. A multi-scale approach to material modeling of fuel cell diffusion media. *Int. J. Heat Mass Transfer* **2011**, 54, 1360-1368.

(62) Hutzenlaub, T.; Becker, J.; Zengerle, R.; Thiele, S. Modelling the water distribution within a hydrophilic and hydrophobic 3D reconstructed cathode catalyst layer of a proton exchange membrane fuel cell. *J. Power Sources* **2013**, 227, 260-266.
(63) Litster, S.; Epting, W. K.; Wargo, E. A.; Kalidindi, S. R.; Kumbur, E. C. Morphological Analyses of Polymer Electrolyte Fuel Cell Electrodes with Nano-Scale Computed Tomography Imaging. *Fuel Cells* **2013**, 13, 935-945.
(64) Gostick, J. T.; Fowler, M. W.; Ioannidis, M. A.; Pritzker, M. D.; Volfkovich, Y. M.; Sakars, A. Capillary pressure and hydrophilic porosity in gas diffusion layers for polymer electrolyte fuel cells. *J. Power Sources* **2006**, 156, 375-387.
(65) Schweiss, R.; Steeb, M.; Wilde, P. M. Mitigation of Water Management in PEM Fuel Cell Cathodes by Hydrophilic Wicking Microporous Layers. *Fuel Cells* **2010**, 10, 1176-1180.
(66) Schweiss, R.; Steeb, M.; Wilde, P. M.; Schubert, T. Enhancement of proton exchange membrane fuel cell performance by doping microporous layers of gas diffusion layers with multiwall carbon nanotubes. *Journal of Power Sources* **2012**, 220, 79-83.
(67) Makharia, R.; Mathias, M. F.; Baker, D. R. Measurement of catalyst layer electrolyte resistance in PEFCs using electrochemical impedance spectroscopy. *J. Electrochem. Soc.* **2005**, 152, A970-A977.
(68) Eikerling, M.; Kornyshev, A. A. Electrochemical impedance of the cathode catalyst layer in polymer electrolyte fuel cells. *J. Electroanal. Chem.* **1999**, 475, 107-123.
(69) Yi, J. S.; Song, T.-w. Performance Characterization of PEM Fuel Cells Using AC Impedance Spectroscopy: I. Model-Based Analysis. *J. Electrochem. Soc.* **2013**, 160, F141-F152.
(70) Nielsen, J.; Hjalmarsson, P.; Hansen, M. H.; Blennow, P. Effect of low temperature in-situ sintering on the impedance and the performance of intermediate temperature solid oxide fuel cell cathodes. *J. Power Sources* **2014**, 245, 418-428.
(71) González-Cuenca, M.; Zipprich, W.; Boukamp, B. A.; Pudmich, G.; Tietz, F. Impedance Studies on Chromite-Titanate Porous Electrodes under Reducing Conditions. *Fuel Cells* **2001**, 1, 256-264.
(72) Bard, A. J.; Faulkner, L. R. *Electrochemical methods : fundamentals and applications*; 2nd ed.; John Wiley: New York, 2001.
(73) Nam, J. H.; Kaviany, M. Effective diffusivity and water-saturation distribution in single- and two-layer PEMFC diffusion medium. *International Journal of Heat and Mass Transfer* **2003**, 46, 4595-4611.
(74) Salby, M. L. *International Geophysics, Volume 61 : Fundamentals of Atmospheric Physics*; Academic Press: Burlington, MA, USA, 1996.
(75) Salomov, U. R.; Chiavazzo, E.; Asinari, P. Pore-scale modeling of fluid flow through gas diffusion and catalyst layers for high temperature proton exchange membrane (HT-PEM) fuel cells. *Computers & Mathematics with Applications* **2014**, 67, 393-411.
(76) Page, K. A.; Kusoglu, A.; Stafford, C. M.; Kim, S.; Kline, R. J.; Weber, A. Z. Confinement-Driven Increase in Ionomer Thin-Film Modulus. *Nano Lett.* **2014**, 14, 2299-2304.
(77) Kim, S.; Dura, J. A.; Page, K. A.; Rowe, B. W.; Yager, K. G.; Lee, H.-J.; Soles, C. L. Surface-Induced Nanostructure and Water Transport of Thin Proton-Conducting Polymer Films. *Macromolecules* **2013**, 46, 5630-5637.
(78) Page, K. A.; Cable, K. M.; Moore, R. B. Molecular Origins of the Thermal Transitions and Dynamic Mechanical Relaxations in Perfluorosulfonate Ionomers. *Macromolecules* **2005**, 38, 6472-6484.
(79) Xie, Z.; Navessin, T.; Shi, K.; Chow, R.; Wang, Q.; Song, D.; Andreaus, B.; Eikerling, M.; Liu, Z.; Holdcroft, S. Functionally Graded Cathode Catalyst Layers for Polymer Electrolyte Fuel Cells: II. Experimental Study of the Effect of Nafion Distribution. *J. Electrochem. Soc.* **2005**, 152, A1171-A1179.
(80) Song, D. T.; Wang, Q. P.; Liu, Z. S.; Eikerling, M.; Xie, Z.; Navessin, T.; Holdcroft, S. A method for optimizing distributions of Nafion and Pt in cathode catalyst layers of PEM fuel cells. *Electrochim. Acta* **2005**, 50, 3347-3358.
(81) Jaouen, F.; Proietti, E.; Lefevre, M.; Chenitz, R.; Dodelet, J. P.; Wu, G.; Chung, H. T.; Johnston, C. M.; Zelenay, P. Recent advances in non-precious metal catalysis for oxygen-reduction reaction in polymer electrolyte fuel cells. *Energ Environ Sci* **2011**, 4, 114-130.
(82) Tüber, K.; Pócza, D.; Hebling, C. Visualization of water buildup in the cathode of a transparent PEM fuel cell. *Journal of Power Sources* **2003**, 124, 403-414.

(83) Maass, S.; Finsterwalder, F.; Frank, G.; Hartmann, R.; Merten, C. Carbon support oxidation in PEM fuel cell cathodes. *Journal of Power Sources* **2008**, 176, 444-451.
(84) Oh, H.-S.; Kim, K.; Ko, Y.-J.; Kim, H. Effect of chemical oxidation of CNFs on the electrochemical carbon corrosion in polymer electrolyte membrane fuel cells. *International Journal of Hydrogen Energy* **2010**, 35, 701-708.
(85) StrmcnikD; KodamaK; van der Vliet, D.; GreeleyJ; Stamenkovic, V. R.; Marković, N. M. The role of non-covalent interactions in electrocatalytic fuel-cell reactions on platinum. *Nat Chem* **2009**, 1, 466-472.
(86) Kinoshita, K.; Bett, J. A. S. Potentiodynamic analysis of surface oxides on carbon blacks. *Carbon* **1973**, 11, 403-411.
(87) Scherson, D. A.; Gupta, S. L.; Fierro, C.; Yeager, E. B.; Kordesch, M. E.; Eldridge, J.; Hoffman, R. W.; Blue, J. Cobalt tetramethoxyphenyl porphyrin—emission Mossbauer spectroscopy and O2 reduction electrochemical studies. *Electrochimica Acta* **1983**, 28, 1205-1209.
(88) Scherson, D.; Tanaka, A. A.; Gupta, S. L.; Tryk, D.; Fierro, C.; Holze, R.; Yeager, E. B.; Lattimer, R. P. Transition metal macrocycles supported on high area carbon: Pyrolysis—mass spectrometry studies. *Electrochimica Acta* **1986**, 31, 1247-1258.
(89) Goellner, V.; Baldizzone, C.; Schuppert, A.; Sougrati, M. T.; Mayrhofer, K.; Jaouen, F. Degradation of Fe/N/C catalysts upon high polarization in acid medium. *Physical Chemistry Chemical Physics* **2014**, 16, 18454-18462.
(90) Li, Y.; Zhou, W.; Wang, H.; Xie, L.; Liang, Y.; Wei, F.; Idrobo, J.-C.; Pennycook, S. J.; Dai, H. An oxygen reduction electrocatalyst based on carbon nanotube-graphene complexes. *Nat Nano* **2012**, 7, 394-400.
(91) Olson, T. S.; Pylypenko, S.; Fulghum, J. E.; Atanassov, P. Bifunctional Oxygen Reduction Reaction Mechanism on Non-Platinum Catalysts Derived from Pyrolyzed Porphyrins. *J. Electrochem. Soc.* **2010**, 157, B54-B63.
(92) Martins Alves, M. C.; Tourillon, G. Influence of Complexation Processes on the Catalytic Properties of Some Polymer-Based Cobalt Compounds for Oxygen Electroreduction. *J. Phys. Chem.* **1996**, 100, 7566-7572.
(93) Hu, Y.; Jensen, J. O.; Zhang, W.; Cleemann, L. N.; Xing, W.; Bjerrum, N. J.; Li, Q. Hollow Spheres of Iron Carbide Nanoparticles Encased in Graphitic Layers as Oxygen Reduction Catalysts. *Angew. Chem. Int. Ed.* **2014**, 53, 3675-3679.
(94) Dodelet, J.-P.; Chenitz, R.; Yang, L.; Lefèvre, M. A New Catalytic Site for the Electroreduction of Oxygen? *ChemCatChem* **2014**, 6, 1866-1867.
(95) Masa, J.; Xia, W.; Muhler, M.; Schuhmann, W. On the Role of Metals in Nitrogen-Doped Carbon Electrocatalysts for Oxygen Reduction. *Angew. Chem. Int. Ed.* **2015**, 54, 10102-10120.
(96) Birry, L.; Zagal, J. H.; Dodelet, J.-P. Does CO poison Fe-based catalysts for ORR? *Electrochem. Commun.* **2010**, 12, 628-631.
(97) Schulenburg, H.; Stankov, S.; Schünemann, V.; Radnik, J.; Dorbandt, I.; Fiechter, S.; Bogdanoff, P.; Tributsch, H. Catalysts for the oxygen reduction from heat-treated iron(III) tetramethoxyphenylporphyrin chloride: structure and stability of active sites. *J. Phys. Chem. B* **2003**, 107, 9034-9041.
(98) Koslowski, U. I.; Abs-Wurmbach, I.; Fiechter, S.; Bogdanoff, P. Nature of the catalytic centers of porphyrin-based electrocatalysts for the ORR: a correlation of kinetic current density with the site density of Fe−N4 centers. *J. Phys. Chem. C* **2008**, 112, 15356-15366.
(99) Kramm, U. I.; Abs-Wurmbach, I.; Herrmann-Geppert, I.; Radnik, J.; Fiechter, S.; Bogdanoff, P. Influence of the electron-density of FeN4-centers towards the catalytic activity of pyrolyzed FeTMPPCl-based ORR-electrocatalysts. *J. Electrochem. Soc.* **2011**, 158, B69-B78.
(100) Wu, G.; Nelson, M. A.; Mack, N. H.; Ma, S.; Sekhar, P.; Garzon, F. H.; Zelenay, P. Titanium dioxide-supported non-precious metal oxygen reduction electrocatalyst. *Chem. Commun.* **2010**, 46, 7489-7491.
(101) Kabir, S.; Artyushkova, K.; Kiefer, B.; Atanassov, P. Computational and experimental evidence for a new TM-N3/C moiety family in non-PGM electrocatalysts. *Phys. Chem. Chem. Phys.* **2015**, 17, 17785-17789.
(102) Ferrandon, M.; Kropf, A. J.; Myers, D. J.; Artyushkova, K.; Kramm, U.; Bogdanoff, P.; Wu, G.; Johnston, C. M.; Zelenay, P. Multitechnique characterization of a polyaniline–iron–carbon oxygen reduction catalyst. *J. Phys. Chem. C* **2012**, 116, 16001-16013.

(103) Holby, E. F.; Taylor, C. D. Activity of N-coordinated multi-metal-atom active site structures for Pt-free oxygen reduction reaction catalysis: Role of *OH ligands. *Sci. Rep.* **2015**, 5.

(104) Proietti, E.; Jaouen, F.; Lefèvre, M.; Larouche, N.; Tian, J.; Herranz, J.; Dodelet, J.-P. Iron-based cathode catalyst with enhanced power density in polymer electrolyte membrane fuel cells. *Nat Commun* **2011**, 2, 416.

(105) Bouwkamp-Wijnoltz, A. L.; Visscher, W.; van Veen, J. A. R. The selectivity of oxygen reduction by pyrolysed iron porphyrin supported on carbon. *Electrochim. Acta* **1998**, 43, 3141-3152.

(106) Okada, T.; Gokita, M.; Yuasa, M.; Sekine, I. Oxygen Reduction Characteristics of Heat-Treated Catalysts Based on Cobalt-Porphyrin Ion Complexes. *J. Electrochem. Soc.* **1998**, 145, 815-822.

(107) Wiggins-Camacho, J. D.; Stevenson, K. J. Mechanistic Discussion of the Oxygen Reduction Reaction at Nitrogen-Doped Carbon Nanotubes. *The Journal of Physical Chemistry C* **2011**, 115, 20002-20010.

(108) Bouwkamp-Wijnoltz, A. L.; Visscher, W.; van Veen, J. A. R.; Boellaard, E.; van der Kraan, A. M.; Tang, S. C. On active-site heterogeneity in pyrolyzed carbon-supported iron porphyrin catalysts for the electrochemical reduction of oxygen: an in situ Mössbauer study. *J. Phys. Chem. B* **2002**, 106, 12993-13001.

(109) Kim, S.; Tryk, D.; Bae, I. T.; Sandifer, M.; Carr, R.; Antonio, M. R.; Scherson, D. A. In situ extended x-ray absorption fine structure of an iron porphyrin irreversibly adsorbed on an electrode surface. *J. Phys. Chem.* **1995**, 99, 10359-10364.

(110) Kuroki, S.; Nabae, Y.; Kakimoto, M.-a.; Miyata, S. Oxygen Reduction Activity of Pyrolyzed Polyanilines Studied by 15N Solid-State NMR and XPS with Principal Component Analysis. *ECS Transactions* **2011**, 41, 2269-2276.

(111) Wu, G.; Chen, Z.; Artyushkova, K.; Garzon, F. H.; Zelenay, P. Polyaniline-derived non-precious catalyst for the polymer electrolyte fuel cell cathode. *ECS Trans.* **2008**, 16, 159-170.

(112) Lefèvre, M.; Dodelet, J. P.; Bertrand, P. Molecular Oxygen Reduction in PEM Fuel Cell Conditions: ToF-SIMS Analysis of Co-Based Electrocatalysts. *J. Phys. Chem. B* **2005**, 109, 16718-16724.

(113) Lefèvre, M.; Dodelet, J. P.; Bertrand, P. Molecular Oxygen Reduction in PEM Fuel Cells: Evidence for the Simultaneous Presence of Two Active Sites in Fe-Based Catalysts. *J. Phys. Chem. B* **2002**, 106, 8705-8713.

(114) Gojković, S. L.; Gupta, S.; Savinell, R. F. Heat-Treated Iron(III) Tetramethoxyphenyl Porphyrin Supported on High-Area Carbon as an Electrocatalyst for Oxygen Reduction. *J. Electrochem. Soc.* **1998**, 145, 3493-3499.

(115) Bron, M.; Radnik, J.; Fieber-Erdmann, M.; Bogdanoff, P.; Fiechter, S. EXAFS, XPS and electrochemical studies on oxygen reduction catalysts obtained by heat treatment of iron phenanthroline complexes supported on high surface area carbon black. *J. Electroanal. Chem.* **2002**, 535, 113-119.

(116) Arruda, T. M.; Shyam, B.; Lawton, J. S.; Ramaswamy, N.; Budil, D. E.; Ramaker, D. E.; Mukerjee, S. Fundamental aspects of spontaneous cathodic deposition of Ru onto Pt/C electrocatalysts and membranes under direct methanol fuel cell operating conditions: an in situ x-ray absorption spectroscopy and electron spin resonance study. *J. Phys. Chem. C* **2010**, 114, 1028-1040.

(117) Ankudinov, A. L.; Ravel, B.; Rehr, J. J.; Conradson, S. D. Real-space multiple-scattering calculation and interpretation of x-ray-absorption near-edge structure. *Phys. Rev. B* **1998**, 58, 7565-7576.

(118) Briois, V.; Sainctavit, P.; Long, G. J.; Grandjean, F. Importance of photoelectron multiple scattering in the iron K-edge x-ray absorption spectra of spin-crossover complexes: full multiple scattering calculations for several iron(II) trispyrazolylborate and trispyrazolylmethane complexes. *Inorg. Chem.* **2001**, 40, 912-918.

(119) Briois, V.; dit Moulin, C. C.; Sainctavit, P.; Brouder, C.; Flank, A. M. Full multiple scattering and crystal field multiplet calculations performed on the spin transition FeII(phen)2(NCS)2 complex at the iron K and L2,3 x-ray absorption edges. *J. Am. Chem. Soc.* **1995**, 117, 1019-1026.

(120) Kresse, G.; Furthmüller, J. Efficient iterative schemes for ab initio total-energy calculations using a plane-wave basis set. *Phys. Rev. B* **1996**, 54, 11169-11186.

(121) Kattel, S.; Wang, G. A density functional theory study of oxygen reduction reaction on Me-N4 (Me = Fe, Co, or Ni) clusters between graphitic pores. *Journal of Materials Chemistry A* **2013**, 1, 10790-10797.

(122) Blöchl, P. Projector augmented-wave method. *Phys. Rev. B* **1994**, 50, 17953-17979.

(123) Perdew, J.; Burke, K.; Ernzerhof, M. Generalized gradient approximation made simple. *Phys. Rev. Lett.* **1996**, 77, 3865-3868.

(124) Stefan, I. C.; Mo, Y.; Ha, S. Y.; Kim, S.; Scherson, D. A. In situ Fe K-edge x-ray absorption fine structure of a nitrosyl adduct of iron phthalocyanine irreversibly adsorbed on a high area carbon electrode in an acidic electrolyte. *Inorg. Chem.* **2003**, 42, 4316-4321.
(125) Bae, I. T.; Tryk, D. A.; Scherson, D. A. Effect of heat treatment on the redox properties of iron porphyrins adsorbed on high area carbon in acid electrolytes: an in situ Fe K-edge x-ray absorption near-edge structure study. *J. Phys. Chem. B* **1998**, 102, 4114-4117.
(126) Boillot, M.-L.; Zarembowitch, J.; Itie, J.-P.; Polian, A.; Bourdet, E.; Haasnoot, J. G. Pressure-induced spin-state crossovers at room temperature in iron(II) complexes: comparative analysis; a XANES investigation of some new transitions. *New J. Chem.* **2002**, 26, 313-322.
(127) Hannay, C.; Hubin-Franskin, M.-J.; Grandjean, F.; Briois, V.; Polian, A.; Trofimenko, S.; Long, G. J. X-ray absorption spectroscopic study of the temperature and pressure dependence of the electronic spin states in several iron(II) and cobalt(II) tris(pyrazolyl)borate complexes. *Inorg. Chem.* **1997**, 36, 5580-5588.
(128) Khalil, M.; Marcus, M. A.; Smeigh, A. L.; McCusker, J. K.; Chong, H. H. W.; Schoenlein, R. W. Picosecond x-ray absorption spectroscopy of a photoinduced iron(II) spin crossover reaction in solution. *J. Phys. Chem. A* **2005**, 110, 38-44.
(129) Cartier, C.; Momenteau, M.; Dartyge, E.; Fontaine, A.; Tourillon, G.; Michalowicz, A.; Verdaguer, M. X-Ray absorption spectroscopy of iron-(II) and -(III) basket-handle porphyrins. *J. Chem. Soc., Dalton Trans.* **1992**, 609-618.
(130) Roe, A. L.; Schneider, D. J.; Mayer, R. J.; Pyrz, J. W.; Widom, J.; Que, L. X-ray absorption spectroscopy of iron-tyrosinate proteins. *J. Am. Chem. Soc.* **1984**, 106, 1676-1681.
(131) Natoli, C. R. In *EXAFS and near edge structure III*; Hodgson, K., Hedman, B., Penner-Hahn, J., Eds.; Springer Berlin Heidelberg: **1984**; Vol. 2, p. 38-42.
(132) Jia, Q.; Ramaswamy, N.; Hafiz, H.; Tylus, U.; Strickland, K.; Wu, G.; Barbiellini, B.; Bansil, A.; Holby, E. F.; Zelenay, P.; Mukerjee, S. Experimental Observation of Redox-Induced Fe–N Switching Behavior as a Determinant Role for Oxygen Reduction Activity. *ACS Nano* **2015**, 9, 12496-12505.
(133) Scherson, D. A.; Yao, S. B.; Yeager, E. B.; Eldridge, J.; Kordesch, M. E.; Hoffman, R. W. In situ and ex situ Moessbauer spectroscopy studies of iron phthalocyanine adsorbed on high surface area carbon. *J. Phys. Chem.* **1983**, 87, 932-943.
(134) Scheidt, W. R.; Reed, C. A. Spin-state/stereochemical relationships in iron porphyrins: implications for the hemoproteins. *Chem. Rev.* **1981**, 81, 543-555.
(135) Cao, R.; Thapa, R.; Kim, H.; Xu, X.; Gyu Kim, M.; Li, Q.; Park, N.; Liu, M.; Cho, J. Promotion of oxygen reduction by a bio-inspired tethered iron phthalocyanine carbon nanotube-based catalyst. *Nat. Commun.* **2013**, 4.
(136) Anderson, A. B.; Sidik, R. A. Oxygen electroreduction on FeII and FeIII coordinated to N4 chelates. reversible potentials for the intermediate steps from quantum theory. *J. Phys. Chem. B* **2004**, 108, 5031-5035.
(137) Nørskov, J. K.; Rossmeisl, J.; Logadottir, A.; Lindqvist, L.; Kitchin, J. R.; Bligaard, T.; Jónsson, H. Origin of the overpotential for oxygen reduction at a fuel-cell cathode. *J. Phys. Chem. B* **2004**, 108, 17886-17892.
(138) Jia, Q.; Caldwell, K.; Ziegelbauer, J. M.; Kongkanand, A.; Wagner, F. T.; Mukerjee, S.; Ramaker, D. E. The role of OOH binding site and Pt surface structure on ORR activities. *J. Electrochem. Soc.* **2014**, 161, F1323-F1329.
(139) Roth, C.; Benker, N.; Buhrmester, T.; Mazurek, M.; Loster, M.; Fuess, H.; Koningsberger, D. C.; Ramaker, D. E. Determination of O[H] and CO coverage and adsorption sites on PtRu electrodes in an operating PEM fuel cell. *J. Am. Chem. Soc.* **2005**, 127, 14607-14615.
(140) Lewis, E. A.; Segre, C. U.; Smotkin, E. S. Embedded cluster Δ-XANES modeling of adsorption processes on Pt. *Electrochim. Acta* **2009**, 54, 7181-7185.